

CMS Draft Analysis Note

The content of this note is intended for CMS internal use and distribution only

2016/07/22

Head Id: 358734

Archive Id: 358853

Archive Date: 2016/07/22

Archive Tag: trunk

Search for ttH in multilepton final states at 13 TeV

Anne-Catherine Le Bihan⁶, Benjamin Stieger⁴, Binghuan Li⁵, Charlie Mueller³, Cristina Botta¹, Daniel Bloch⁶, Francesco Romeo⁵, Geoffrey Smith³, Giovanni Petrucciani¹, Huaqiao Zhang⁵, Jan Steggemann¹, Jeremy Andrea⁶, Kevin Lannon³, Kirill Skovpen⁶, Marco Peruzzi¹, Milos Dordevic¹, Nicolas Chanon⁶, Predrag Cirkovic², Rami Kamalieddin⁴, Rebeca Gonzalez Suarez⁴, Xavier Coubez⁶, Thomas Strebler⁷, and Jing Li⁸

¹ CERN

² University of Belgrade

³ University of Notre Dame

⁴ University of Nebraska

⁵ IHEP

⁶ IPHC

⁷ LLR

⁸ PKU

Abstract

A search for the standard model Higgs boson produced in association with a top quark pair is presented, using 12.9 fb^{-1} of 13 TeV pp collision data collected by the CMS experiment at the LHC. Final states with a Higgs boson that decays to either ZZ^* , WW^* , or $\tau\tau$ are required to have a top quark pair that decays to either lepton plus jets ($t\bar{t} \rightarrow \ell\nu jj b\bar{b}$) or dileptons ($t\bar{t} \rightarrow \ell\nu \ell\nu bb\bar{b}$), where ℓ represents an electron or a muon. The following signatures are selected: two isolated same-sign leptons (electrons or muons) plus b-tagged jets, three isolated leptons plus b-tagged jets, or four isolated leptons plus b-tagged jets. The presence of an hadronic τ reconstructed in the event is also considered in the event categorization. The expected 95% confidence level upper limit on the Higgs boson production cross section for a Higgs boson mass of 125 GeV/c² is 1.2 times the standard model expectation, compared to an observed limit of 3.7. The signal strength μ , relative to the expectation for the standard model Higgs boson, is measured to be $2.1^{+0.9}_{-0.8}$.

This box is only visible in draft mode. Please make sure the values below make sense.

PDFAuthor: The ttH multilepton group
PDFTitle: Search for ttH in multilepton final states at 13 TeV
PDFSubject: CMS
PDFKeywords: CMS, physics, higgs, top

Please also verify that the abstract does not use any user defined symbols

DRAFT

1 Contents

2	1	Introduction	2
3	2	Data and MC Samples	4
4	2.1	Data Samples	4
5	2.2	Signal Samples	4
6	2.3	Background Samples	4
7	2.4	Triggers	6
8	2.5	Trigger efficiency in data and simulation	6
9	3	Event reconstruction and object identification	13
10	3.1	Jets and B-tagging	13
11	3.2	Missing Energy	13
12	3.3	Lepton Identification	14
13	3.4	Validation of lepton identification variables	17
14	3.5	Taus	23
15	4	Event selection	25
16	4.1	Two lepton same-sign category	26
17	4.2	Three lepton category	26
18	5	Signal extraction	33
19	5.1	Event subcategories	40
20	6	Signal modeling	41
21	6.1	Correction factors and experimental uncertainties	41
22	6.2	Theoretical uncertainties	41
23	7	Background predictions	44
24	7.1	Irreducible backgrounds	44
25	7.2	Di-bosons backgrounds	46
26	7.3	Charge misassignment background	49
27	7.4	Fake lepton background	52
28	8	Results	63
29	A	Control region plots	64
30	A.1	Lepton MVA sideband region	64
31	A.2	Jet multiplicity sideband region	67
32	A.3	$t\bar{t} \rightarrow e^\pm \mu^\mp b\bar{b} \nu\bar{\nu}$	70
33	A.4	$WZ \rightarrow 3\ell$	75
34	A.5	$t\bar{t}Z \rightarrow 3\ell$	76
35	B	Matrix Element Method	78
36	B.1	The algorithm	78
37	B.2	Treatment of jets and permutations	79
38	B.3	MEM discriminant	82
39	B.4	MEM distributions after event selection	83
40	C	Event Reconstruction	91
41	C.1	Training	91
42	C.2	Evaluation	91

43 1 Introduction

44 The LHC Run I data have been exploited to measure all the accessible properties of the newly-
 45 discovered Higgs boson [1, 2]. ATLAS and CMS have combined their effort in order to reach
 46 an already very precise measurement of the boson mass, 125.09 ± 0.21 (stat.) ± 0.11 (syst.)
 47 GeV [3]. This precise mass result has created an opportunity to test the predictions of the stan-
 48 dard model by measuring the other properties of the Higgs boson. Measurements of the Higgs
 49 boson production and decay rates and constraints on its couplings have been performed by
 50 both experiments [4, 5], and in general, agreement with the SM predictions given the current
 51 uncertainties (10-30 %) have been found. It is of great interest to use the 13 TeV LHC data to
 52 further constrain these measurements as any deviation from expectation could be a sign of new
 53 physics.

54

55 Among these measurements, it is of particular interest to measure the coupling of the Higgs
 56 boson to the top quark ($t\bar{t}H$) because the top quark could play a special role in the context
 57 of electroweak symmetry breaking due to its large mass. The Higgs boson does not decay to
 58 top quarks. The $t\bar{t}H$ interaction vertex, however, is present in a rare production mechanism
 59 where the Higgs boson is produced in association with a top quark-antiquark pair as shown
 60 in Fig. 1. At LHC energies the largest contribution to standard model Higgs boson production
 61 is a gluon-gluon induced loop dominated by virtual top exchange. The comparison of a direct
 62 measurement of the $t\bar{t}H$ coupling with the one inferred from the cross section measurement
 63 can put limits on the contribution of new physics to the gluon-gluon loop.

64

65 The $t\bar{t}H$ process has been used by both experiments to directly measure the top-Higgs coupling
 66 at tree level with the 20 fb^{-1} of 8 TeV collisions of LHC Run I. Via this process, both experiments
 67 reached a 30% accuracy on the top Yukawa coupling, a great achievement given that the pro-
 68 duction cross section (130 fb at 8 TeV at next-to-leading order (NLO) [6]) was two orders of
 69 magnitude lower with respect to the dominant Higgs production mode (gluon-gluon fusion).
 70 In order to achieve this result several decay channels of the Higgs boson have been considered
 71 by both experiments, and three main searches have been designed by both experiments. The
 72 first channel searches for $t\bar{t}H$ in events where the Higgs boson decays to $b\bar{b}$; the best fit value
 73 for the combined signal strength obtained by the CMS experiment is $0.7^{+1.9}_{-1.9}$ (95% CL)) [7].
 74 The second channel searches for $t\bar{t}H$ in events where the Higgs boson decays to $\gamma\gamma$; the best fit
 75 value for the combined signal strength obtained by the CMS experiment is $2.7^{+2.6}_{-1.8}$ (95% CL)) [7].

76

77 We designed the third search to probe $t\bar{t}H$ events where the Higgs boson decays into ZZ^* ,
 78 WW^* , or $\tau\tau$, with at least one Z, W or τ decaying leptonically. Despite the small branching
 79 ratio, the presence of one or two additional leptons from the top quark pair decays leads to the
 80 following clean experimental signatures:

- 81 • two same-sign leptons (electrons or muons) plus b-tagged jets;
- 82 • three leptons plus b-tagged jets;
- 83 • four leptons plus b-tagged jets.

84 Examples of Feynman diagrams for $t\bar{t}H$, followed by the decays of the top quark and the Higgs
 85 boson that lead to the signatures described above are shown in Fig. 1. With this search we ob-
 86 tained the most precise measurement of the $t\bar{t}H$ signal strength: $3.7^{+1.9}_{-1.9}$ (95%CL)) [8].

87

88 The combined best-fit signal strength obtained assuming a Higgs boson mass of 125 GeV was
 89 $\mu = 2.9^{+1.1}_{-0.9}$. This result corresponds to a 3.5 standard deviation excess over the background-
 90 only ($\mu = 0$) hypothesis, and represents a 2.1 standard deviation upward fluctuation on the SM
 91 $t\bar{t}H$ ($\mu = 1$) expectation. Although the combined observed signal strength is consistent with
 92 SM expectations, with a roughly 2 standard deviation upward fluctuation, it is interesting to
 93 point out that the excess was mainly driven by the multilepton analysis, and in particular by
 94 the same-sign di-muon subsample [8].

95

96 The first multilepton search at 13 TeV analyzed 2.3 fb^{-1} of the 2015 Run II dataset. With respect
 97 to 8 TeV, the 13 TeV $t\bar{t}H$ cross section increased by a factor of 4 with the higher center of mass
 98 energy. The cross sections of the main backgrounds $t\bar{t}W$, $t\bar{t}Z$, $t\bar{t}+\text{jets}$ increased by roughly a
 99 factor of 3. This first 13 TeV multilepton search measured the expected 95% confidence level
 100 upper limit on the Higgs boson production cross section for a Higgs boson mass of $125 \text{ GeV}/c^2$
 101 to be 2.6 times the standard model expectation, compared to the observed limit of 3.3. The sig-
 102 nal strength μ , relative to the expectation for the standard model Higgs boson, was measured
 103 to be $0.6^{+1.4}_{-1.1}$ [9].

104

105 In this note we repeat the 2015 multilepton search with the first 4.0 fb^{-1} of 2016 13 TeV data
 106 collected by the CMS experiment. Thus, in this analysis we expect increased precision on the
 107 signal strength measurement compared to the 2015 result. The general strategy remains simi-
 108 lar to the 2015 search. Multivariate analysis techniques are used to identify objects with high
 109 purity and to distinguish background from signal events. The amount of signal is fit to the
 110 multivariate discriminant output distribution in all the final states simultaneously.

111

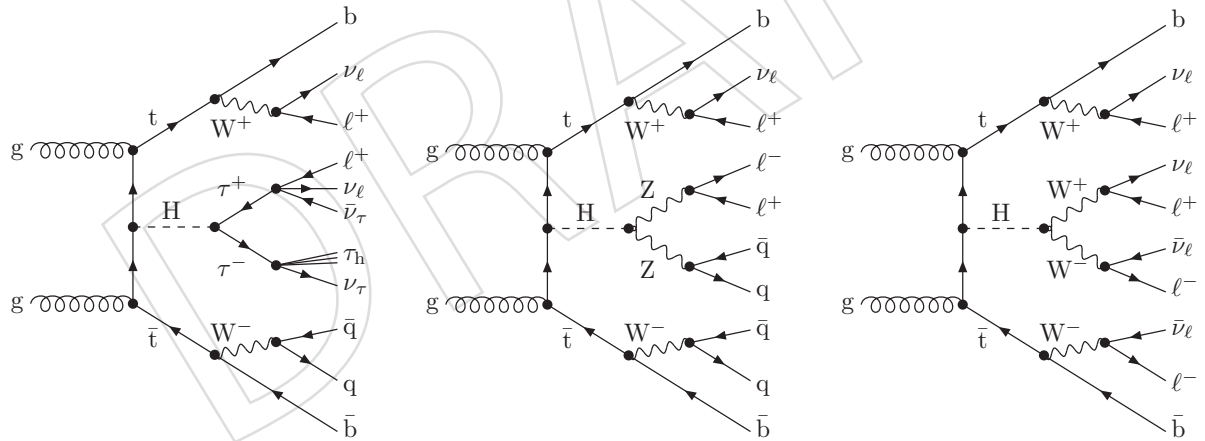


Figure 1: Example leading order Feynman diagrams for $t\bar{t}H$ production at pp colliders, with the Higgs boson decaying to $\tau\tau$, ZZ^* and WW^* (from left to right). The first, second, and third diagrams are examples of the two same-sign lepton signature, the three lepton signature, and the four lepton signature, respectively.

112 2 Data and MC Samples

113 In the following we list as reference the set of samples of the RunIISpring16MiniAODv2 (CMSSW
 114 80X) campaign used for the studies and results presented in this analysis.

115 **2.1 Data Samples**

116 The data used in this analysis was collected with the CMS detector in 2016. We use data col-
 117 lected only during periods when the CMS magnet was on, corresponding to a total integrated
 118 luminosity of 12.9 fb^{-1} [10]. We use the PromptReco-v2 version of the datasets.

119 **2.2 Signal Samples**

120 We use simulated Monte-Carlo events to model both the ttH signal and the various standard
 121 model backgrounds. The ttH events are simulated at next-to-leading-order (NLO) accuracy
 122 using aMC@NLO [11], and matched to PYTHIA [12] for the parton shower. An additional
 123 POWHEG [13] ttH sample provides more statistics when training boosted descision trees dur-
 124 ing the signal extraction phase, but is not used in computing the final result of the analysis.
 125 More details on the samples and the NLO cross section are reported in Table 1.

Sample	Xsec (pb)
/ttHJettToNonbb_M125_13TeV_amcatnloFXFX_madspin_pythia8_mWCutfix/RunIISpring16MiniAODv2-PUSpring16RAWAODSIM_80X_mcRun2_asymptotic_2016_miniAODv2_v0_ext1-v2/MINIAODSIM	0.2586
/ttHToNonbb_M125_13TeV_powheg_pythia8/RunIISpring16MiniAODv2-PUSpring16RAWAODSIM_80X_mcRun2_asymptotic_2016_miniAODv2_v0-v1/MINIAODSIM	0.2586

Table 1: Signal samples used in this analysis (CMSSW 80X).

126 **2.3 Background Samples**

127 In this section, we list the Monte-Carlo samples used to model our backgrounds. A variety of
 128 methods are used to produce these samples: for our dominant backgrounds (ttbar, ttW, ttZ), we
 129 use the same aMC@NLO→PYTHIA chain used for the ttH signal and the NLO cross sections.
 130 Other minor backgrounds may use other generators, such as PYTHIA or POWHEG matched
 131 to PYTHIA. See table 2 for more details.

132

133 The nominal $t\bar{t}Z$ MC sample is generated with the requirement $m_{\ell^+\ell^-} > 10 \text{ GeV}$, because of
 134 this, we also use LO Madgraph to generate the remaining part of the phase space ($1 < m_{\ell^+\ell^-} <$
 135 10 GeV). This private sample was produced both in the context of the RunIISpring16MiniAODv2
 136 and RunIISpring16MiniAODv1 (CMSSW 80X) campaigns. Another sample not yet available in
 137 both campaigns is the $t\bar{t}WW$. Nevertheless in the RunI analysis we proved that in all the ana-
 138 lyzed final states, the contribution of the process is found to be at least an order of magnitude
 139 smaller than $t\bar{t}W$ and $t\bar{t}Z$.

Sample	Xsec (pb)
/TTWjetsToLNu.TuneCUETP8M1_13TeV-amcatnloFXFX-madspin-pythia8/RunIISpring16MiniAODv2-PUSpring16.80X_mcRun2_asymptotic_2016_miniAODv2_v0-v1/MINIAODSIM	0.2043
/TTZToLNuNu.M-10.TuneCUETP8M1_13TeV-amcatnlo-pythia8/RunIISpring16MiniAODv2-PUSpring16.80X_mcRun2_asymptotic_2016_miniAODv2_v0-v1/MINIAODSIM	0.2529
/store/cms3/group/susy/sptreucci/13TeV/RunIISpring16MiniAODv2/TTL_L_m1to10_L0_NoMS_for76X/	0.0283
/WGToLNuG.TuneCUETP8M1_13TeV-madgraphMLM-pythia8/RunIISpring16MiniAODv2-PUSpring16.80X_mcRun2_asymptotic_2016_miniAODv2_v0-v1/MINIAODSIM	585.8
/ZGto2L_G.TuneCUETP8M1_13TeV-amcatnloFXFX-pythia8/RunIISpring16MiniAODv2-PUSpring16.80X_mcRun2_asymptotic_2016_miniAODv2_v0-v1/MINIAODSIM	131.3
/TGjets.TuneCUETP8M1_13TeV_amcatnlo_madspin_pythia8/RunIISpring16MiniAODv2-PUSpring16.80X_mcRun2_asymptotic_2016_miniAODv2_v0-v1/MINIAODSIM	2.967
/TTGjets.TuneCUETP8M1_13TeV-amcatnloFXFX-madspin-pythia8/RunIISpring16MiniAODv2-PUSpring16.80X_mcRun2_asymptotic_2016_miniAODv2_v0-v1/MINIAODSIM	3.697
/WpWpjj_EWK-QCD.TuneCUETP8M1_13TeV-madgraph-pythia8/RunIISpring16MiniAODv2-PUSpring16.80X_mcRun2_asymptotic_2016_miniAODv2_v0-v1/MINIAODSIM	0.03711
Rares_ZZZ (not yet available)	
Rares_WWZ (not yet available)	
Rares /WWZ.TuneCUETP8M1_13TeV-amcatnlo-pythia8/RunIISpring16MiniAODv2-PUSpring16.80X_mcRun2_asymptotic_2016_miniAODv2_v0-v1/MINIAODSIM	0.05565
Rares /WW_DoubleScattering_13TeV-pythia8/RunIISpring16MiniAODv2-PUSpring16.80X_mcRun2_asymptotic_2016_miniAODv2_v0-v1/MINIAODSIM	1.64
Rares /Zq_ll_4f_13TeV-amcatnlo-pythia8.TuneCUETP8M1/RunIISpring16MiniAODv2-PUSpring16.80X_mcRun2_asymptotic_2016_miniAODv2_v0-v1/MINIAODSIM	0.0758
Rares /TTT1.TuneCUETP8M1_13TeV-amcatnlo-pythia8/RunIISpring16MiniAODv2-PUSpring16.80X_mcRun2_asymptotic_2016_miniAODv2_v0_ext1-v1/MINIAODSIM	0.009103
/TTJets_SingleLeptFromTbar.TuneCUETP8M1_13TeV-madgraphMLM-pythia8/RunIISpring16MiniAODv2-PUSpring16.80X_mcRun2_asymptotic_2016_miniAODv2_v0-v1/MINIAODSIM	182
/TTJets_SingleLeptFromT.TuneCUETP8M1_13TeV-madgraphMLM-pythia8/RunIISpring16MiniAODv2-PUSpring16.80X_mcRun2_asymptotic_2016_miniAODv2_v0-v1/MINIAODSIM	182
/T1Jets_DiLept.TuneCUETP8M1_13TeV-madgraphMLM-pythia8/RunIISpring16MiniAODv2-PUSpring16.80X_mcRun2_asymptotic_2016_miniAODv2_v0-v4/MINIAODSIM	87.3
/DYjetsToLL_M-10to50.TuneCUETP8M1_13TeV-amcatnloFXFX-pythia8/RunIISpring16MiniAODv2-PUSpring16.80X_mcRun2_asymptotic_2016_miniAODv2_v0-v1/MINIAODSIM	18610
/DYjetsToLL_M-50.TuneCUETP8M1_13TeV-madgraphMLM-pythia8/RunIISpring16MiniAODv2-PUSpring16.80X_mcRun2_asymptotic_2016_miniAODv2_v0_ext1-v1/MINIAODSIM	6025.2
/WjetsToLNu.TuneCUETP8M1_13TeV-amcatnloFXFX-pythia8/RunIISpring16MiniAODv2-PUSpring16.80X_mcRun2_asymptotic_2016_miniAODv2_v0-v1/MINIAODSIM	61526.7
/ST_tW_top_5f_inclusiveDecays_13TeV-powheg-pythia8.TuneCUETP8M1/RunIISpring16MiniAODv2-PUSpring16.80X_mcRun2_asymptotic_2016_miniAODv2_v0-v2/MINIAODSIM	35.6
/ST_tW_antitop_5f_inclusiveDecays_13TeV-powheg-pythia8.TuneCUETP8M1/RunIISpring16MiniAODv2-PUSpring16.80X_mcRun2_asymptotic_2016_miniAODv2_v0-v1/MINIAODSIM	35.6
/ST_t-channel_4f (not yet available)	
/ST_t-channel_antitop (not yet available)	
/ST_s-channel_4f_leptonDecays_13TeV-amcatnlo-pythia8.TuneCUETP8M1/RunIISpring16MiniAODv2-PUSpring16.80X_mcRun2_asymptotic_2016_miniAODv2_v0-v1/MINIAODSIM	3.75
/WZTo3LNu.TuneCUETP8M1_13TeV-powheg-pythia8/RunIISpring16MiniAODv2-PUSpring16.80X_mcRun2_asymptotic_2016_miniAODv2_v0-v1/MINIAODSIM	4.102
/WWTo2l2Nu_13TeV-powheg/RunIISpring16MiniAODv2-PUSpring16.80X_mcRun2_asymptotic_2016_miniAODv2_v0-v1/MINIAODSIM	10.481
/ZZTo4L_13TeV_powheg_pythia8/RunIISpring16MiniAODv2-PUSpring16.80X_mcRun2_asymptotic_2016_miniAODv2_v0-v1/MINIAODSIM	1.256

Table 2: List of background samples used in this analysis (CMSSW 80X). In the first section of the table are listed the samples of the processes for which we use the simulation to extract the final yields and shapes, in the second section the samples of the processes we will estimate from data. The MC simulation is used to design the data driven methods and derive the associated systematics.

140 **2.4 Triggers**

141 In this analysis, we consider online-reconstructed events triggered on one, two or three leptons.
 142 The inclusion of single-lepton triggers boosts acceptance by including events where the p_T of
 143 the subleading lepton falls below the threshold of the double-lepton triggers. In addition, by
 144 including double-lepton triggers in the ≥ 3 lepton category, as well as single-lepton triggers in
 145 all categories, we increase efficiency by considering the logical “or” of the trigger decisions of
 146 all the individual triggers in a given category. Table 3 shows the lowest-threshold unprescaled
 147 triggers present in the High-Level Trigger (HLT) menus for both Monte-Carlo and data in 2016
 148 (will be updated if subsequent data have different unprescaled triggers).

Same-sign dilepton (==2 muons)
HLT_Mu17_TrkIsoVVL_Mu8_TrkIsoVVL_DZ_v*
HLT_Mu17_TrkIsoVVL_TkMu8_TrkIsoVVL_DZ_v*
HLT_IsoMu22_v*
HLT_IsoTkMu22_v*
Same-sign dilepton (==2 electrons)
HLT_Ele23_Ele12_CaloIdL_TrackIdL_IsoVL_DZ_v*
HLT_Ele27_eta2p1_WPLoose_Gsf_v*
Same-sign dilepton (==1 muon, ==1 electron)
HLT_Mu23_TrkIsoVVL_Ele8_CaloIdL_TrackIdL_IsoVL_v*
HLT_Mu8_TrkIsoVVL_Ele23_CaloIdL_TrackIdL_IsoVL_v*
HLT_IsoMu22_v*
HLT_IsoTkMu22_v*
HLT_Ele27_eta2p1_WPLoose_Gsf_v*
Three lepton and Four lepton
HLT_DiMu9_Ele9_CaloIdL_TrackIdL_v*
HLT_Mu8_DiEle12_CaloIdL_TrackIdL_v*
HLT_TripleMu_12_10_5_v*
HLT_Ele16_Ele12_Ele8_CaloIdL_TrackIdL_v*
HLT_Mu23_TrkIsoVVL_Ele8_CaloIdL_TrackIdL_IsoVL_v*
HLT_Mu8_TrkIsoVVL_Ele23_CaloIdL_TrackIdL_IsoVL_v*
HLT_Ele23_Ele12_CaloIdL_TrackIdL_IsoVL_DZ_v*
HLT_Mu17_TrkIsoVVL_Mu8_TrkIsoVVL_DZ_v*
HLT_Mu17_TrkIsoVVL_TkMu8_TrkIsoVVL_DZ_v*
HLT_IsoMu22_v*
HLT_IsoTkMu22_v*
HLT_Ele27_eta2p1_WPLoose_Gsf_v*

Table 3: Table of high-level triggers that we consider in the analysis.

149 **2.5 Trigger efficiency in data and simulation**

150 Figures 2, 3, 4, and 5 show a comparison of the trigger efficiency between data and Monte-
 151 Carlo in each of the analysis categories. In general, we find that the trigger efficiencies in the
 152 data agree well with simulation. Measuring the efficiency in simulated events is straightfor-
 153 ward because there is no trigger bias with simulated events. To measure the efficiency in data
 154 we follow the procedure described here [14], which was also the same procedure used in the
 155 Run I and 2015 Run II multilepton analyses. We first select a set of events that were recorded on
 156 a trigger that is uncorrelated with the lepton triggers. We use events recorded on a MET trigger
 157 as a unbiased sample. We then look for candidate events with exactly two good leptons. We
 158 measure the efficiency for the candidate events to pass the logical “or” of triggers being con-
 159 sidered in a given event category (i.e., the triggers listed by category in table 3).
 160

161 We use scale factors to correct for small differences in the trigger efficiency between data and
 162 Monte-Carlo. Due to a lack of statistics, for events with ≥ 3 leptons we do not apply a correc-

Category	Scale Factor
2e	1.02 ± 0.02
e+mu	1.02 ± 0.01
2mu	1.01 ± 0.01
3 and 4l	$(1) \pm 0.06$

Table 4: Trigger efficiency scale factors and associated uncertainties, shown here rounded to the nearest percent.

tion factor to the simulation, but instead apply an uncertainty of 6% to all processes modeled with simulation in this channel that is large enough to accommodate any differences in performance. For two-lepton events, we do apply correction factors to the simulation that correct for small differences in performance compared to the data. These correction factors are the ratio of the efficiency in data to the efficiency in simulation, and are summarized in table 4.

Some of our Monte-Carlo samples were not produced with trigger information. For these samples, as well as applying the data/MC trigger scale factors, we also apply a per-event weight based on the trigger efficiency measured in ttH Monte-Carlo. These weights are binned in 2 dimensions as a function of the leading and subleading lepton p_T . Figure 6 summarizes these efficiencies. As a cross-check, we compare the shapes of a variety of event variables after applying the efficiencies in figure 6, versus after filtering directly from the trigger decisions. We observe good agreement between the two methods for each of these variables, including the p_T of the dilepton system (made up of the two leading leptons), shown in Figure 7.

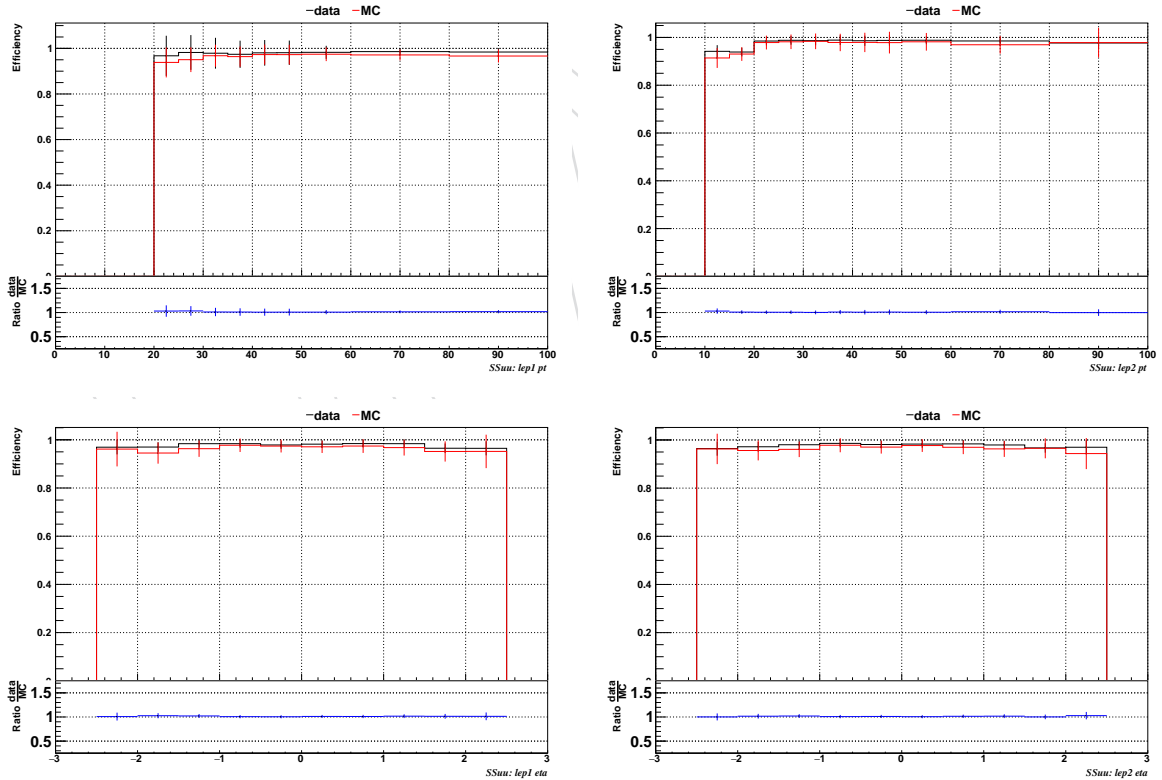


Figure 2: Comparison of the trigger efficiency in the same-sign dimuon category before corrections, shown as a function of the p_T and η of the leading lepton (left) and the sub-leading lepton (right).

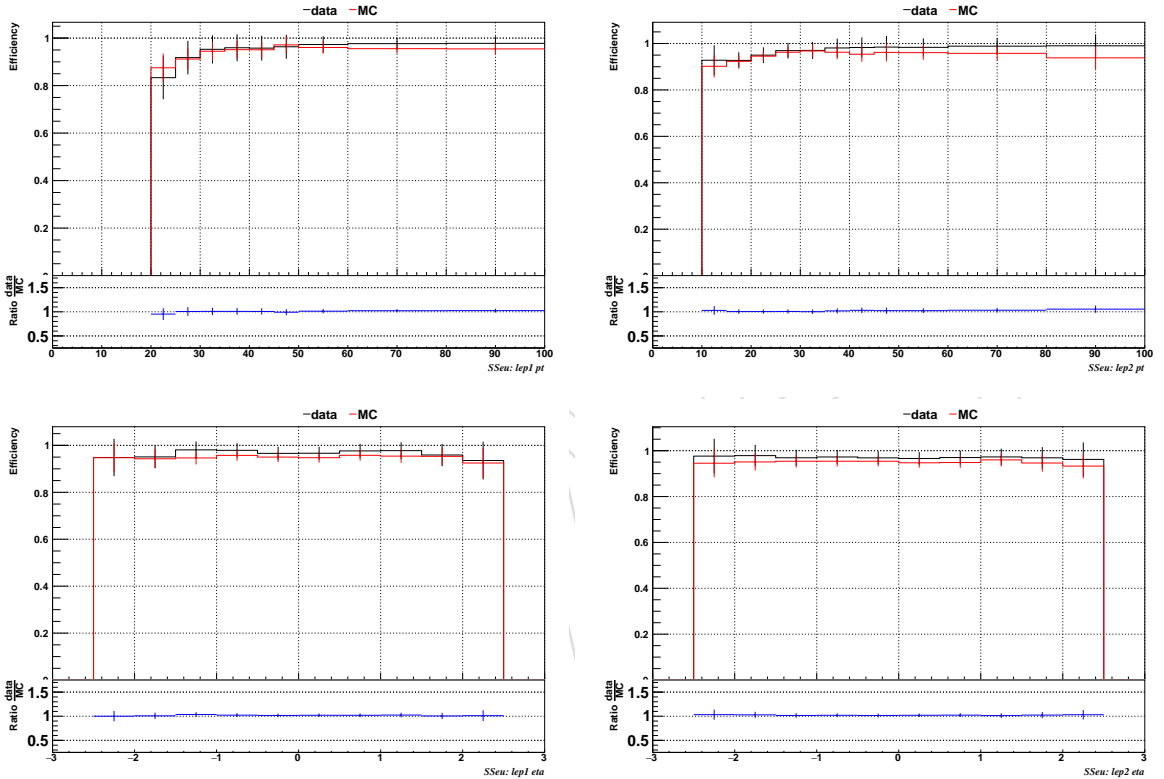


Figure 3: Comparison of the trigger efficiency in the same-sign muon+electron category before corrections, shown as a function of the p_T and η of the leading lepton (left) and the sub-leading lepton (right).

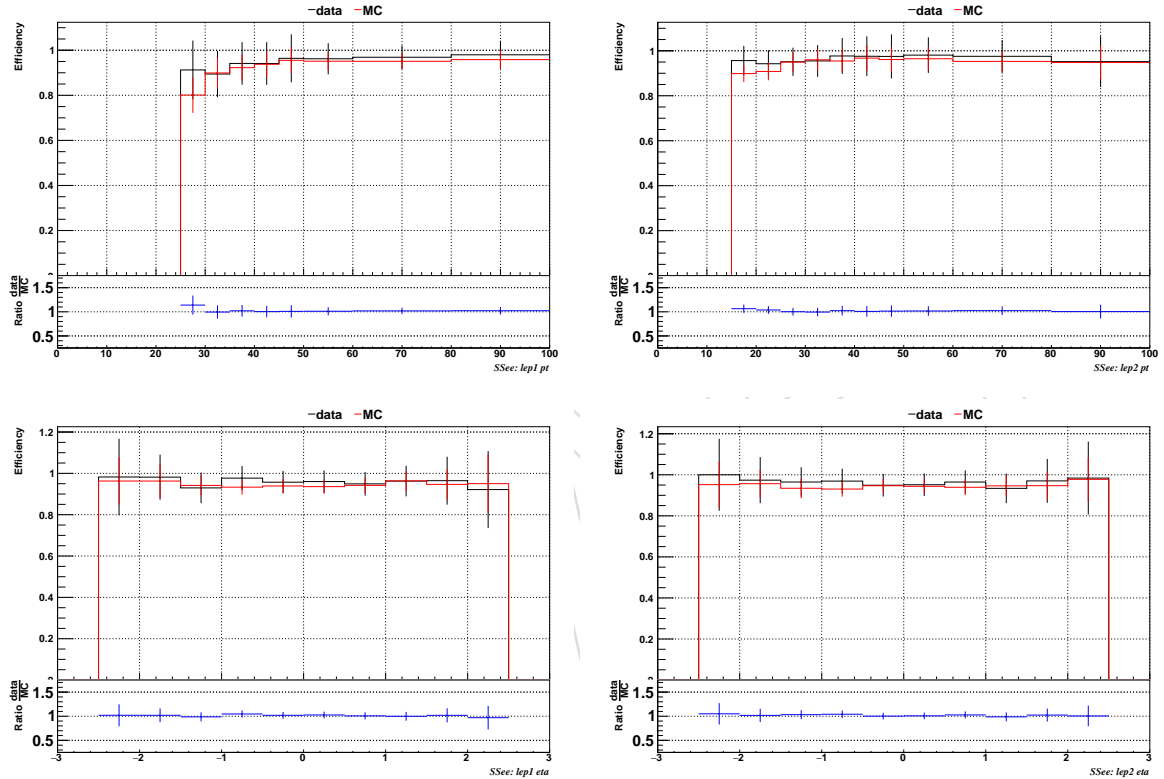


Figure 4: Comparison of the trigger efficiency in the same-sign dielectron category before corrections, shown as a function of the p_T and η of the leading lepton (left) and the sub-leading lepton (right).

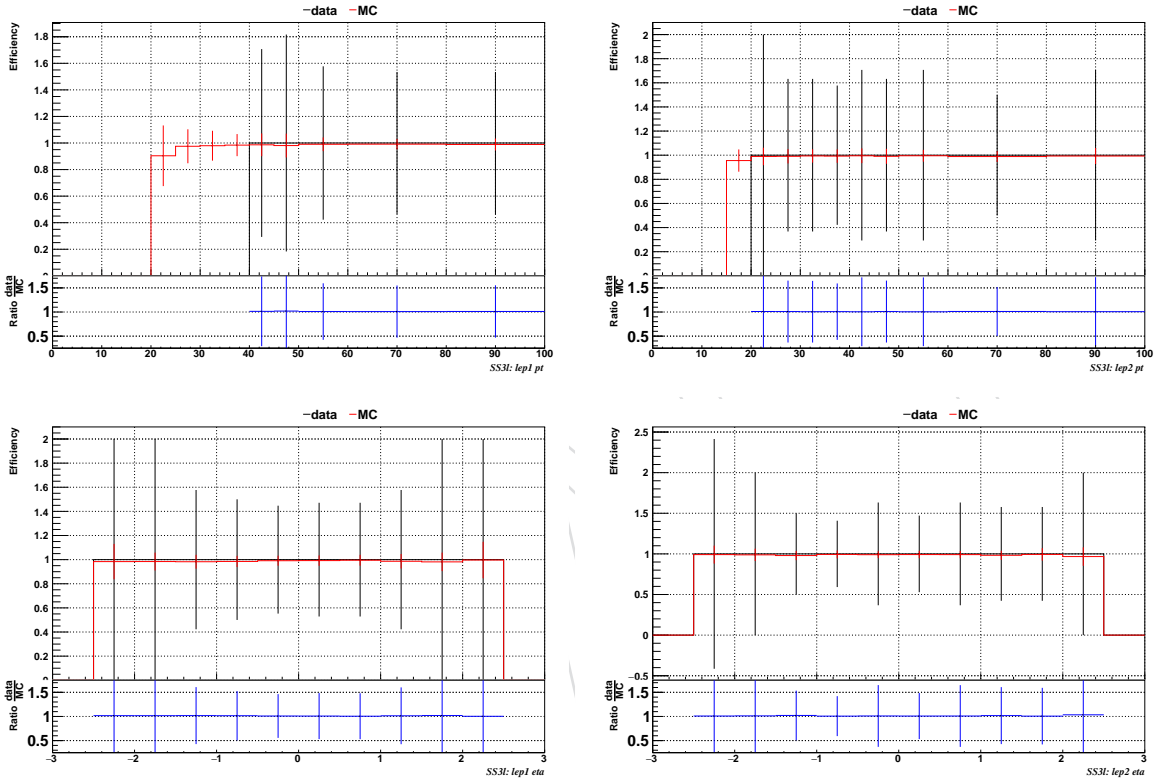


Figure 5: Comparison of the trigger efficiency in the ≥ 3 -lepton category before corrections, shown as a function of the p_T and η of the leading lepton (left) and the sub-leading lepton (right). Due to the low statistics in data, for these events we do not attempt to calculate a scale factor but instead assign an uncertainty that is large enough to cover differences in performance between data and simulation.

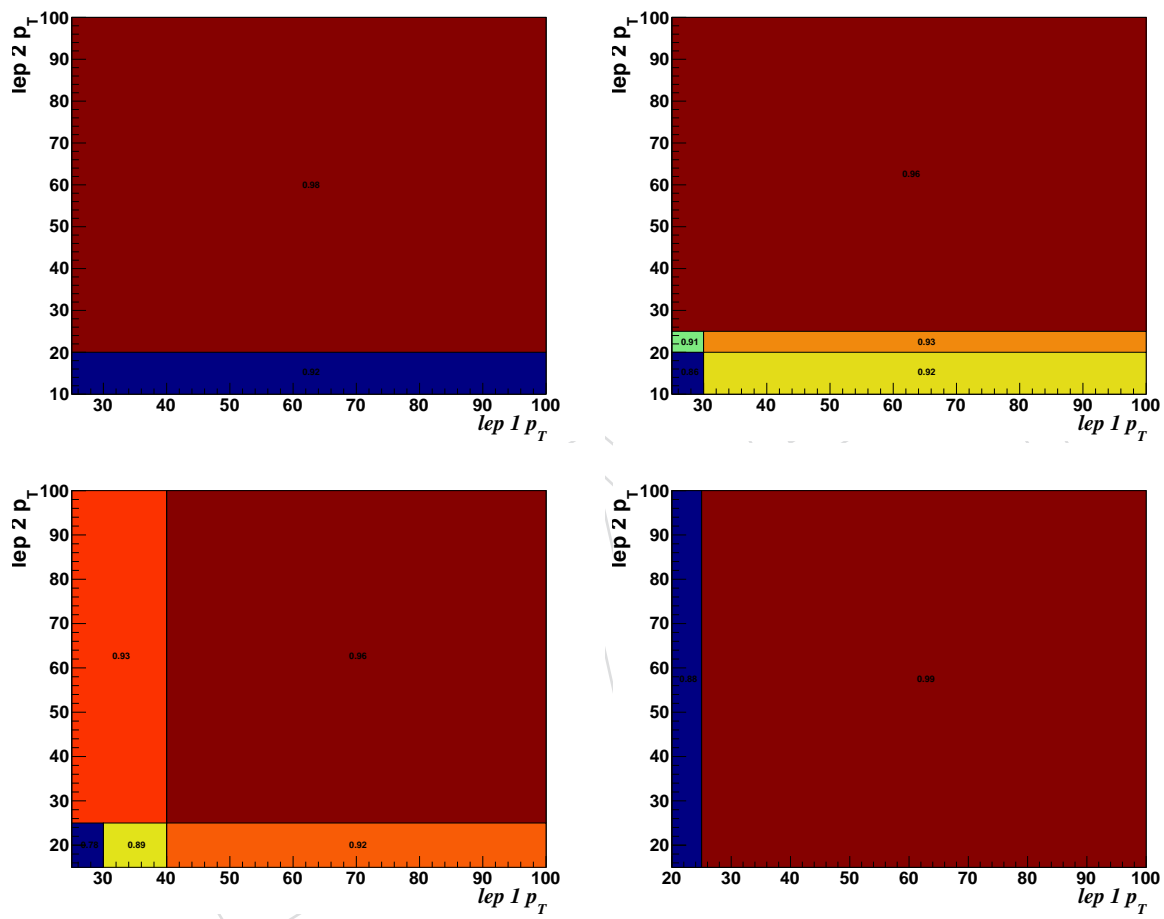


Figure 6: Clockwise from top left: trigger efficiency regions in the same-sign dimuon, same-sign muon+electron, 3 lepton and same-sign dielectron categories.

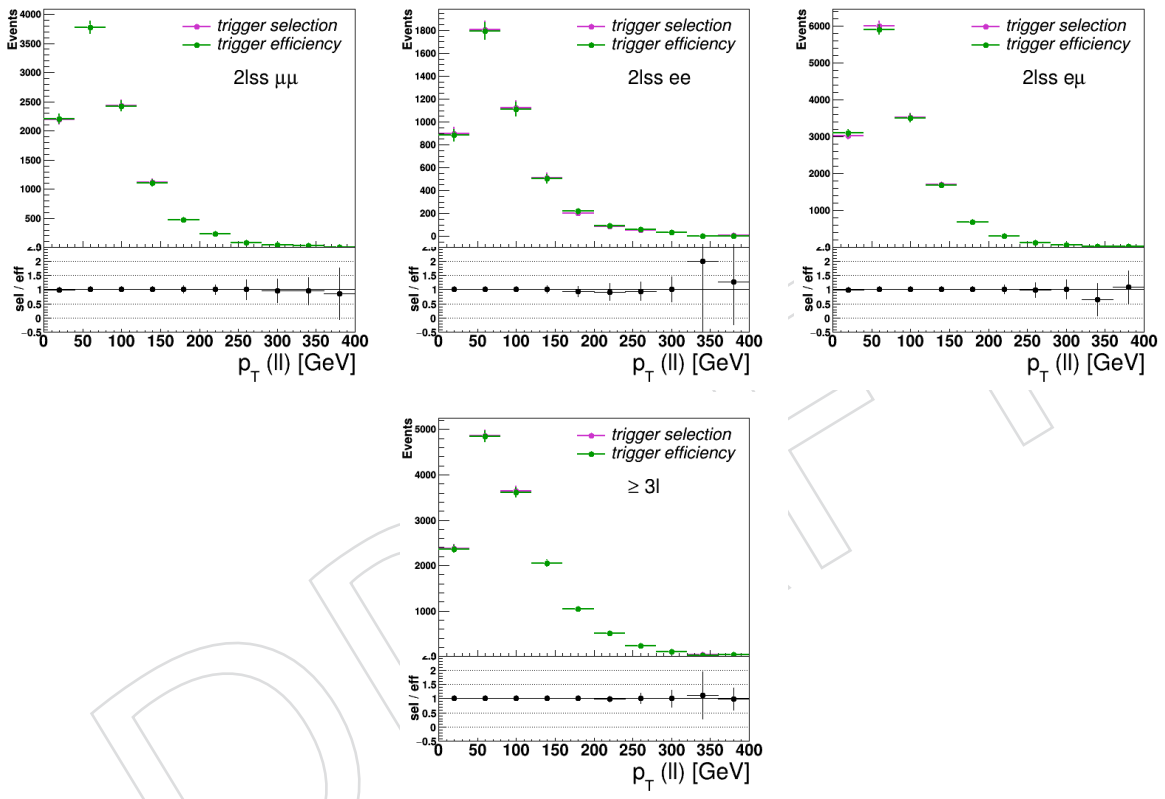


Figure 7: Closure test showing the difference between applying the trigger selection directly to ttH MC and applying the derived trigger efficiency to ttH MC. Here, the dilepton p_T distribution in the 2ℓ ($\mu\mu$, ee , $e\mu$) categories (top), and the $\geq 3\ell$ category (bottom) is shown. Uncertainties are statistical only.

176 3 Event reconstruction and object identification

177 A complete reconstruction of the individual particles from each collision event is obtained
 178 via the particle-flow (PF) algorithm. The technique uses the information from all CMS sub-
 179 detectors to identify and reconstruct individual particles in the collision event [15, 16]. The
 180 particles are classified into mutually exclusive categories: charged hadrons, neutral hadrons,
 181 photons, muons, and electrons.

182 3.1 Jets and B-tagging

183 Jets are reconstructed by clustering PF candidates using the anti- k_T algorithm with distance
 184 parameter $\Delta R = 0.4$ as implemented in the FASTJET package [17, 18]. The charged hadrons not
 185 coming from the primary vertices are subtracted from the PF candidates considered in the clus-
 186 tering. The primary vertex is chosen as the vertex with the highest sum of p_T^2 of its constituent
 187 tracks. The prescribed jet energy corrections are applied as a function of the jet E_T and η [19]. In
 188 addition, a multivariate discriminator is applied to distinguish between jets coming from the
 189 primary vertex and jets coming from pile-up vertices. The discrimination is based on the dif-
 190 ferences in the jet shapes, in the relative multiplicity of charged and neutral components, and
 191 in the different fraction of transverse momentum which is carried by the hardest components.
 192 Within the tracker acceptance the jet tracks are also required to be compatible with the primary
 193 vertex. Jets are only considered if they have a transverse energy above 25 GeV and $|\eta| < 2.4$.
 194 In addition, they have to be separated from any lepton candidates passing the Fakeable Object
 195 selection by requiring $\Delta R = \sqrt{(\eta^\ell - \eta^{jet})^2 + (\phi^\ell - \phi^{jet})^2} > 0.4$.

196 The CSV b-tagging algorithm [20] is used to identify jets that are likely to originate from the
 197 hadronization of bottom quarks. This algorithm combines both secondary vertex information
 198 and track impact parameter information together in a likelihood discriminant. The discrimi-
 199 nant output value ranges from zero to one. It distinguishes between b -jets and jets originating
 200 from light quarks, gluons and charm quarks. The efficiency to tag b -jets and the rate of misiden-
 201 tification of non- b jets depend on the operating point chosen. Both the efficiency and the fake
 202 rate are parameterised as a function of the transverse momentum and pseudorapidity of the
 203 jets. These performance measurements are obtained directly from data in samples that can be
 204 enriched in b jets, such as $t\bar{t}$ and multijet events where a muon can be found inside the one of
 205 jets. Two working points for the CSV output discriminant are used in the analysis. The *loose*
 206 one ($\text{CSV} > 0.46$) has approximately 85% efficiency to tag jets with b quarks and a 10% chance
 207 to tag jets with only light quarks or gluons. The *medium* working point ($\text{CSV} > 0.80$) has ap-
 208 proximately 70% efficiency for tagging jets with b quarks and 1.5% efficiency to tag jets with
 209 only light quarks or gluons [20].

210 We correct for data/sim differences in the b-tagging performance by applying to the simula-
 211 tion per-jet weights dependent on the jet pt, eta, b-tagging discriminator and flavour (from
 212 simulation truth). The weights are derived on $t\bar{t}$ and $Z+jets$ events. The per-event weight
 213 is taken as the product of the per-jet weight, including those of the jets associated to the leptons.

214

215 3.2 Missing Energy

The missing transverse energy vector is calculated offline as the negative of the vector sum
 of transverse momenta of all PF candidates identified in the event. The magnitude of this
 vector is referred to as E_T^{miss} . To recover from the performance degradation of the missing
 transverse energy due to pile-up interactions, we also consider the H_T^{miss} variable, computed in
 the same way as the E_T^{miss} , but using only the selected jets and leptons (the lepton selection will

be described in the following paragraphs). The H_T^{miss} variable has worse resolution than E_T^{miss} but is more robust as it does not rely on the soft part of the event. In this analysis the event selection makes use of a linear discriminator based on the two variables, $E_T^{miss}LD$, exploiting the fact that E_T^{miss} and H_T^{miss} are less correlated in events with instrumental missing energy with respect to events with real missing energy. The $E_T^{miss}LD$ is defined as

$$E_T^{miss}LD = E_T^{miss} * 0.00397 + H_T^{miss} * 0.00265 \quad (1)$$

and the working point used is $E_T^{miss}LD > 0.2$, as in HIG-15-008.

3.3 Lepton Identification

In this analysis, *background leptons* are defined as leptons coming from b-hadron decays, the misidentification of light jets, and photon conversions. We define *signal leptons* as the isolated leptons coming from W, Z, and τ decays.

The reconstruction and identification of electron and muon candidates is described first, followed by the advanced identification criteria used to retain the highest possible efficiency for signal leptons while rejecting background leptons.

3.3.1 Muons reconstruction and identification

Muon candidates are reconstructed combining the information from both the silicon tracker and the muon spectrometer in a global fit [21]. An identification selection is performed using the quality of the geometrical matching between the tracker and the muon system measurements.

Two working points are considered for the muon identification. The loose working point, "POG Loose ID" described in [22], and a tighter working point given by the list of requirements on the muon segment-compatibility variable, known as the "POG Medium Id", defined in [23]. The usage of each working point will be described in Table 6. Only muons within the muon system acceptance $|\eta| < 2.4$ and minimum p_T cuts of 5 GeV are considered.

234

3.3.2 Electron reconstruction and identification

Electrons are reconstructed using tracking and electromagnetic calorimeter information by combining ECAL superclusters and gaussian sum filter (GSF) tracks. We require electrons to have $|\eta| < 2.5$ to ensure that they are within the tracking volume and a minimum p_T of 7 GeV. The electron identification is performed using a multivariate discriminant built with shower-shape variables ($\sigma_{i\eta i\eta}$, $\sigma_{i\phi i\phi}$, the cluster circularity, widths along η and ϕ , R₉, H/E, E_{inES}/E_{raw}), track-cluster matching variables (E_{tot}/p_{in} , E_{Ele}/p_{out} , $\Delta\eta_{in}$, $\Delta\eta_{out}$, $\Delta\phi_{in}$, $1/E - 1/p$) and track quality variables (χ^2 of the KF and GSF tracks, the number of hits used by the KF/GSF filters, fbrem). A complete description of the multivariate discriminant (MVA ID) and training used can be found in [24]. A loose selection based on eta-dependent cuts on this discriminant is used to preselect our electron candidates, the full shape of the discriminant is used in the lepton multivariate selection to separate signal leptons from background leptons. Additional identification criteria are applied for electrons with p_T greater than 30 GeV to mimic the identification applied at trigger level in order to ensure consistency between the *measurement* region and *application* region of the fake-rate (as it will be described in dedicated sections).

All the selection criteria will be described in Table 7.

251 **3.3.3 Lepton vertexing**

252 With the goal of rejecting pile-up or mis-reconstructed tracks, and more importantly to reject
 253 background leptons from b-hadron decays impact parameter variables are also considered:
 254 impact parameter in the transverse plane d_0 , impact parameter along the z axis d_z , and the
 255 impact parameter significance in the detector space SIP_{3D} .

256 Loose cuts are applied on this variables to achieve the first goal, while the full shape of the same
 257 variables is used in a multivariate approach to reach the best separation between the signal and
 258 the background leptons.

259 The details of the selections are provided in Table 7, Table 6.

260 **3.3.4 Lepton isolation**

The charged leptons produced in decays of heavy particles, such as W and Z bosons, are typically spatially isolated from the hadronic activity in the event, while the leptons produced in the decays of hadrons or misidentified leptons are usually embedded in jets. This distinction become less evident moving to highly boosted systems where decay products tend to overlap. Therefore, given the higher collision energy, instead of using the standard PF Isolation where all the neutral, charged hadrons and photons are considered in a cone of $\Delta R = \sqrt{(\eta^\ell - \eta^i)^2 + (\phi^\ell - \phi^i)^2} < 0.3$ around the leptons, a new isolation variable is constructed: the mini isolation I_{mini} .

Requiring I_{mini} below a given threshold ensures that the lepton is locally isolated, even in boosted topologies. The impact of pileup is mitigated using the so-called effective area correction:

$$I_{\text{mini}} = \frac{\sum_R p_T(h^\pm) - \max(0, \sum_R p_T(h^0) + p_T(\gamma) - \rho \mathcal{A} (\frac{R}{0.3})^2)}{p_T(\ell)}. \quad (2)$$

where ρ is the pileup energy density, where $\sum_R p_T(h^\pm)$, $\sum_R p_T(h^0)$ and $\sum_R p_T(\gamma)$ refers to the sum of the transverse momentum of the charged hadrons, neutral hadrons and photons, respectively, within a cone R , dependent of the lepton p_T :

$$R = \frac{10}{\min(\max(p_T(\ell), 50), 200)} \quad (3)$$

The effective areas \mathcal{A} used are listed in Table 5. A very loose cut on this variable is applied to

$ \eta $ range	$\mathcal{A}(e)$ neutral/charged	$\mathcal{A}(\mu)$ neutral/charged
0.0 – 0.8	0.1607 / 0.0188	0.1322 / 0.0191
0.8 – 1.3	0.1579 / 0.0188	0.1137 / 0.0170
1.3 – 2.0	0.1120 / 0.0135	0.0883 / 0.0146
2.0 – 2.2	0.1228 / 0.0135	0.0865 / 0.0111
2.2 – 2.5	0.2156 / 0.0105	0.1214 / 0.0091

Table 5: Effective areas, for muons and electrons

261 pre-select the muon and electron candidates, while the full shape is used in the multivariate
 262 discriminator for the signal lepton selection. Again, details of the selections are provided in in
 263 Table 7, Table 6.

265 **3.3.5 Jet-related variables**

In this analysis the most important source of misidentified leptons comes from the decay of b-hadrons (from $t\bar{t}$ +jets, DY+jets, and W+jets events). We therefore want to use in addition

to the vertexing and isolation variables described above additional handles to target the rejection of this particular type of background leptons. These additional variables are related to the jet reconstructed in the event closest to the lepton. In particular we use the PF jets reconstructed around the leptons, requiring $\Delta R = \sqrt{(\eta^\ell - \eta^{jet})^2 + (\phi^\ell - \phi^{jet})^2} < 0.5$; charged hadrons from pile-up primary vertices are not removed prior to the jet clustering. The four considered variables are the ratio between the p_T of the lepton and the p_T of the jet, the CSV b-tagging discriminator value of the jet, the number of charged tracks of the jet, and the p_T^{rel} variable:

$$p_T^{\text{rel}} = \frac{(\vec{p}(\text{jet}) - \vec{p}(\ell)) \cdot \vec{p}(\ell)}{||\vec{p}(\text{jet}) - \vec{p}(\ell)||}. \quad (4)$$

266 In order to avoid an over-correction on prompt leptons, the application of the jet energy cor-
 267 rection is only applied on the hadronic part of the jet, using the following formula $\text{jet} =$
 268 $\ell + (\text{jet-PU-}\ell) * \text{JEC} - \text{PU}$, where ℓ is the lepton, PU the pileup energy clustered into the jet,
 269 and JEC the jet energy scale correction to be applied to any jet.

270 3.3.6 Lepton MVA discriminator

271 In order to profit from all these handles together, we first preselect our leptons candidates with
 272 the *Loose* selection that will be described in the following, and we then developed a multivar-
 273 iate discriminator based on boosted decision tree (BDT) techniques to distinguish signal leptons
 274 (from W, Z, or τ decays) from background leptons (mostly from b-hadron decays). We refer to
 275 it as the *lepton MVA discriminator* throughout this document. The multivariate discriminator is
 276 trained using simulated signal Loose leptons from the $t\bar{t}H$ MC sample and fake leptons from
 277 the $t\bar{t}+\text{jets}$ MC sample, separately for muons and electrons. The training used in this analysis
 278 is unchanged with respect to the 2015 analysis, detailed in [25]. It uses as input variables the
 279 vertexing, isolation and jet-related variables described so far, the p_T and η of the lepton and two
 280 additional variables that contribute to make it robust also in the rejection of leptons from light
 281 jets mis-identification: the electron MVA ID discriminator and the muon segment-compatibility
 282 variables.

283 In Fig. 8 the performances of the lepton MVA are described comparing the efficiency on sig-
 284 nal lepton from $t\bar{t}H$ to the one on background leptons from $t\bar{t}$ that pass the preselection. The
 285 performances are compared with what we would obtained simply using the I_{mini} , and with
 286 the identification working point choose by the same-sign dilepton SUSY analysis (SUS-15-008),
 287 which is a cut based algorithm based on I_{mini} , p_T^{ratio} , p_T^{rel} , SIP_{3D} on top of the Muon Medium ID
 288 and a tight working point for the electron MVA ID.
 289

290 3.3.7 Additional requirements

291 In the dilepton final state additional requirements on the quality of the charge assignment are
 292 applied to suppress opposite-sign events in which the charge of one of the leptons is mismea-
 293 sured. For the electrons we require consistency between the independent measurements of the
 294 charge from the ECAL supercluster and the tracker, while for the muons we require the track
 295 transverse momentum to be well measured ($\Delta p_T / p_T < 0.2$). We will refer to these cuts as *tight-*
charge
 296 Moreover in order to suppress as much as possible background electrons from photon conver-
 297 sions we reject electrons with missing hits in the innermost layer or associated with a success-
 298 fully reconstructed conversion vertex [26].

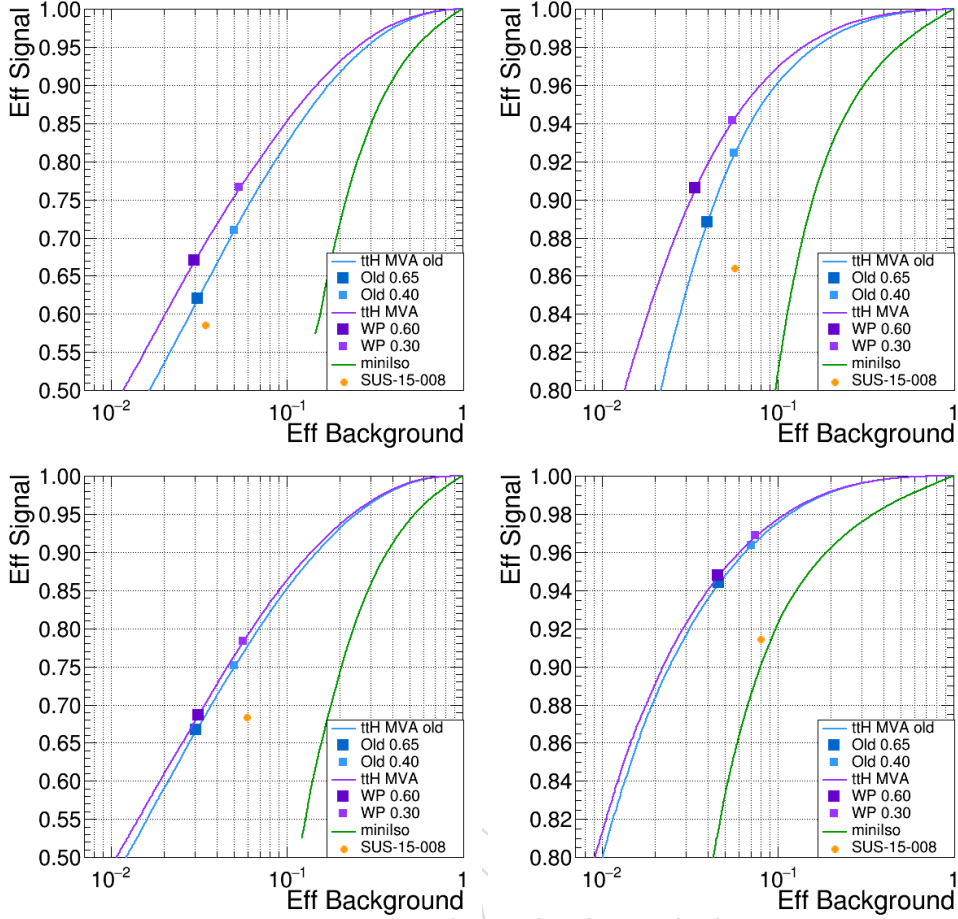


Figure 8: The lepton MVA ROCs are shown from top left to bottom right for electrons with $10 < p_T < 25$, electrons with $p_T > 25$, muons with $10 < p_T < 25$, muons with $p_T > 25$. CMSSW 76X MC is used for this plot.

3.3.8 Loose, *Fakeable Object*, Tight definitions

- Three different selections are used both for the electron and the muon objects identification: the *Loose*, the *Fakeable Object*, the *Tight* selection. In the description of the analysis strategy it will be explained for which purposes the different criteria are used.
 For reasons that will be explained in the data-driven background prediction session, for the *Fakeable Object* selections the lepton p_T is intended to $0.85 * p_T(jet)$ with the jet being the one associated to the lepton as defined for the jet-related variables computation.
 In Table 6 and Table 7 all the criteria on the variables previously described are listed.

3.4 Validation of lepton identification variables

- We validate the modelling of the lepton identification variables in simulation by looking at two control regions, one enriched in prompt leptons from dileptonic $t\bar{t}$, and one enriched in non-prompt leptons from semi-leptonic $t\bar{t}$. The first control region is obtained selecting opposite-sign dilepton events with at least two jets and at least one medium b-tagged jet or two loose ones; events with more than two leptons are vetoed. The second control region is obtained selecting same-sign dilepton events with exactly three or four jets, and exactly one medium b-tagged jet, in order to suppress the contributions from $t\bar{t}V$ and $t\bar{t}H$, and similarly events with more than two leptons are vetoed. In both control regions, the trailing lepton is required only

Table 6: Requirements on each of the three muon selections. In the cases where the cut values change between the selections, those values are listed in the table. Otherwise, whether the cut is applied is indicated. For the two p_T^{ratio} and CSV rows, the cuts marked with † are applied to leptons that fail the lepton MVA cut, while the loose cut value to those that pass the lepton MVA cut.

Cut	Loose	Fakeable Object	Tight
$ \eta < 2.4$	✓	✓	✓
p_T	> 5	> 10	> 10
$ d_{xy} < 0.05 \text{ (cm)}$	✓	✓	✓
$ d_z < 0.1 \text{ (cm)}$	✓	✓	✓
$\text{SIP}_{3D} < 8$	✓	✓	✓
$I_{\text{mini}} < 0.4$	✓	✓	✓
is Loose Muon	✓	✓	✓
p_T^{ratio}	—	$> 0.3† / -$	—
jet CSV	—	$< 0.46† / < 0.80$	< 0.80
is Medium Muon	—	—	✓
tight-charge	—	—	✓
lepMVA > 0.75	—	—	✓

Table 7: Requirements on each of the three electron selections. In the cases where the cut values change between the selections, those values are listed in the table. Otherwise, whether the cut is applied is indicated. In some cases, the cut values change for different η ranges. These ranges are $0 < |\eta| < 0.8$, $0.8 < |\eta| < 1.479$, and $1.479 < |\eta| < 2.5$ and the respective cut values are given in the form (value₁, value₂, value₃).

Cut	Loose	Fakeable Object	Tight
$ \eta < 2.5$	✓	✓	✓
p_T	> 7	> 10	$> 15(10) \text{ 2lss}(3l)$
$ d_{xy} < 0.05 \text{ (cm)}$	✓	✓	✓
$ d_z < 0.1 \text{ (cm)}$	✓	✓	✓
$\text{SIP}_{3D} < 8$	✓	✓	✓
$I_{\text{mini}} < 0.4$	✓	✓	✓
MVA ID	$> (-0.70, -0.83, -0.92)$	$> (-0.70, -0.83, -0.92)$ for corr. $p_T > 30$	$> (-0.70, -0.83, -0.92)$ for corr. $p_T > 30$
$\sigma_{ijinj} < (0.011, 0.011, 0.030)$	—	—	—
$H/E < (0.10, 0.10, 0.07)$	—	—	—
$\Delta\eta_{in} < (0.01, 0.01, 0.008)$	—	—	—
$\Delta\phi_{in} < (0.04, 0.04, 0.07)$	—	—	—
$-0.05 < 1/E - 1/p < (0.010, 0.010, 0.005)$	—	—	—
p_T^{ratio}	—	$> 0.3† / -$	—
jet CSV	—	$< 0.46† / < 0.80$	< 0.80
tight-charge	—	—	✓
conversion rejection	—	—	✓
Number of missing hits	< 2	$= 0$	$= 0$
lepMVA > 0.75	—	—	✓

317 to pass the loose selection, not the lepMVA requirement, so that its properties can be studied
 318 in an unbiased way. A data to simulation comparison is done for the lepton MVA discriminant
 319 and some of the more important inputs: the mini-isolation, SIP_{3D} , p_T^{ratio} , p_T^{rel} and the b-tagging
 320 discriminator of the associated jet (Fig. 9 and 10). In all cases, the simulation is normalized to
 321 data, scaling all contributions by the same factor. The contribution from $t\bar{t}$ is split according to
 322 the origin of the lepton in the simulation: prompt, non-prompt from B hadron decays ($b \rightarrow \ell_{\text{np}}$),
 323 or non-prompt from other origins ($j \rightarrow \ell_{\text{np}}$). A good agreement between data and simulations is
 324 observed overall. Some small discrepancy is visible mainly for extreme values of the b-tagging
 325 discriminator and small SIP_{3D} for non-prompt leptons, which could be also be partially from
 326 different relative abundances of leptons from heavy flavour vs light flavour processes in data
 327 with respect to simulations, or a slightly different levels of prompt lepton contamination.

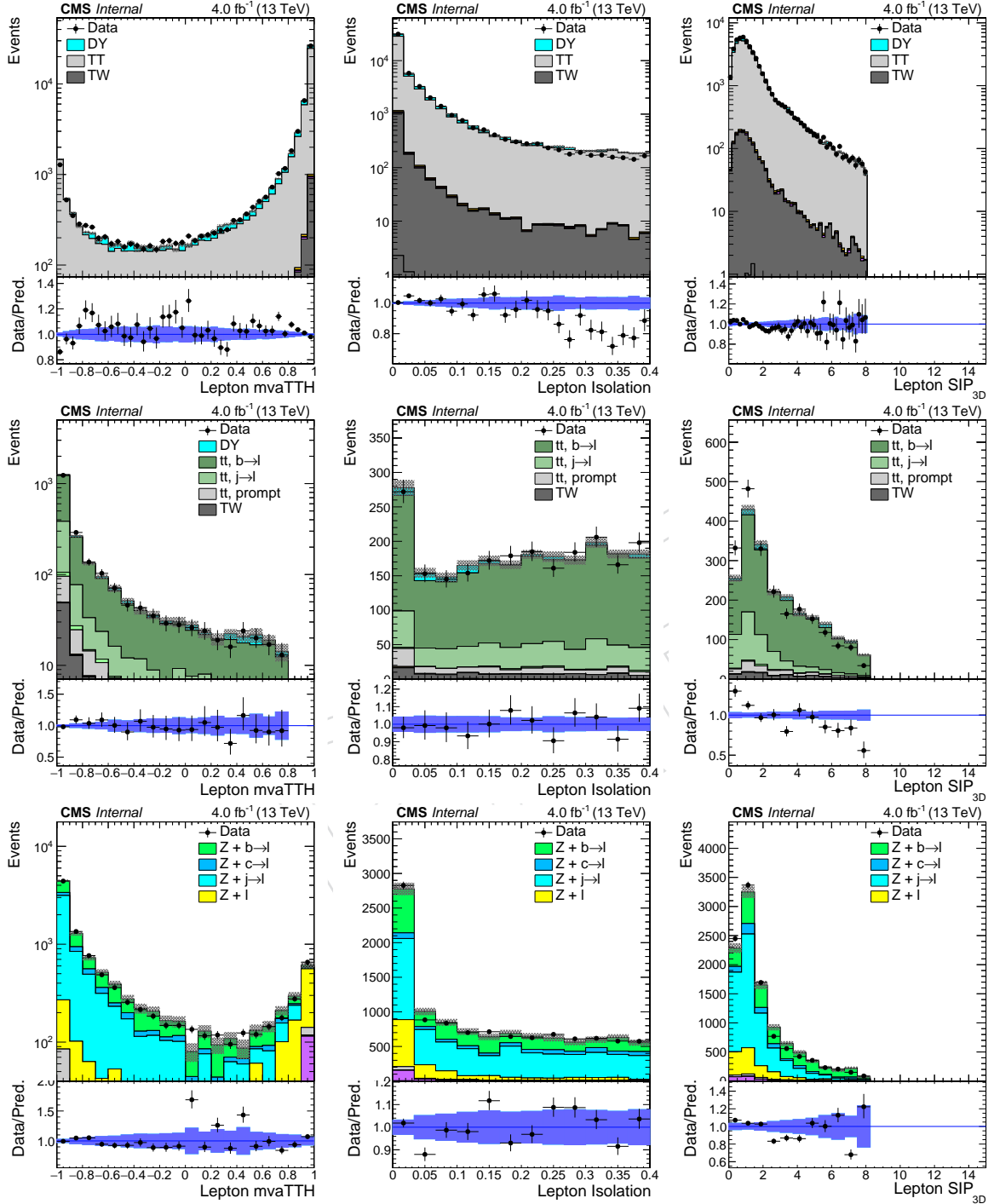


Figure 9: Comparison of the distributions for the lepton MVA (left), mini-isolation (center), and SIP_{3D} (right) between data and simulations in control regions enriched in prompt leptons (top) or non-prompt leptons (bottom), as described in the text. The uncertainty shown on the simulation is only statistical.

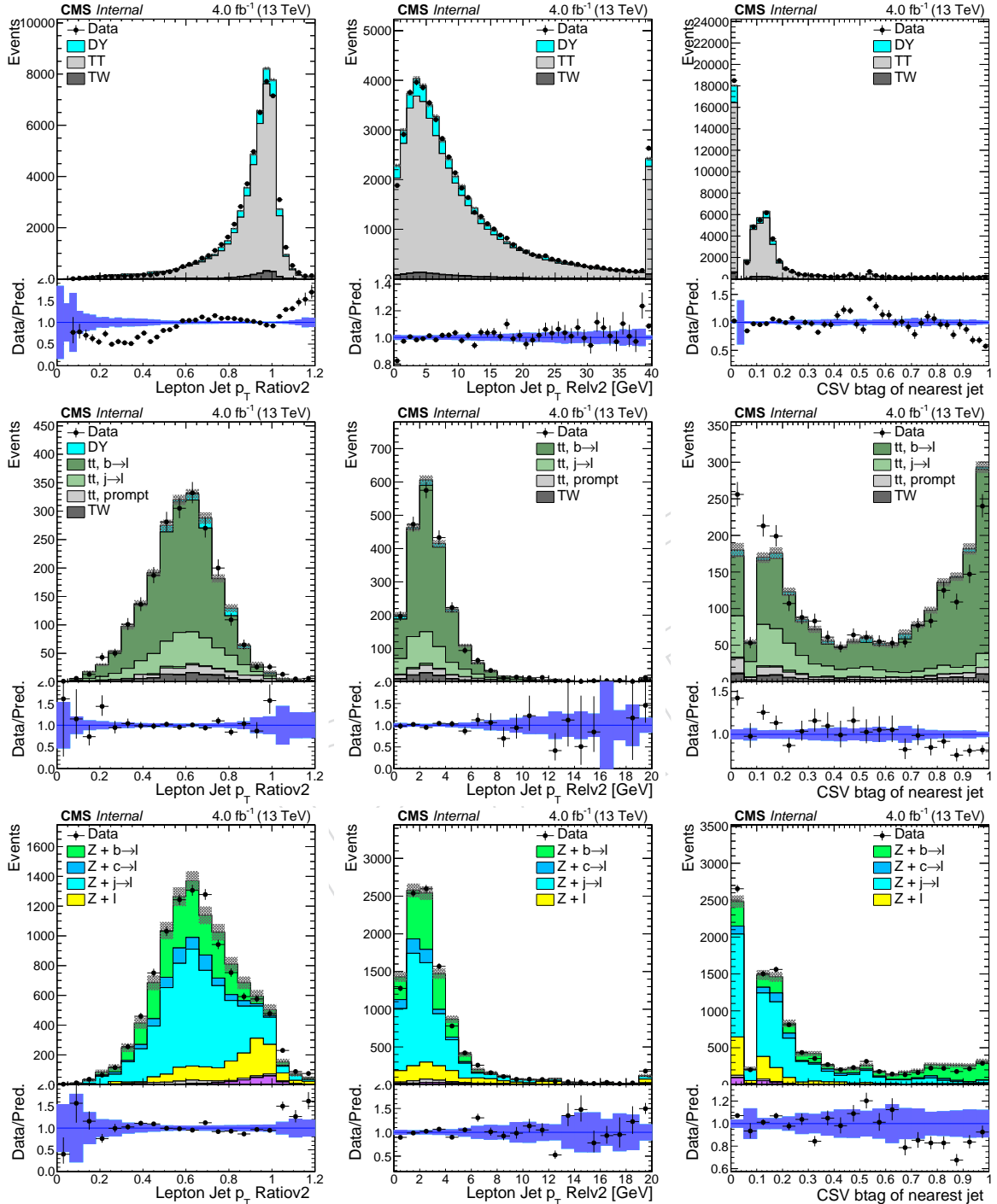


Figure 10: Comparison of the distributions for the lepton p_T^{ratio} (left), p_T^{rel} (center) and the b-tagging discriminator of the associated jet (right), between data and simulations in control regions enriched in prompt leptons (top) or non-prompt leptons (bottom), as described in the text. The uncertainty shown on the simulation is only statistical.

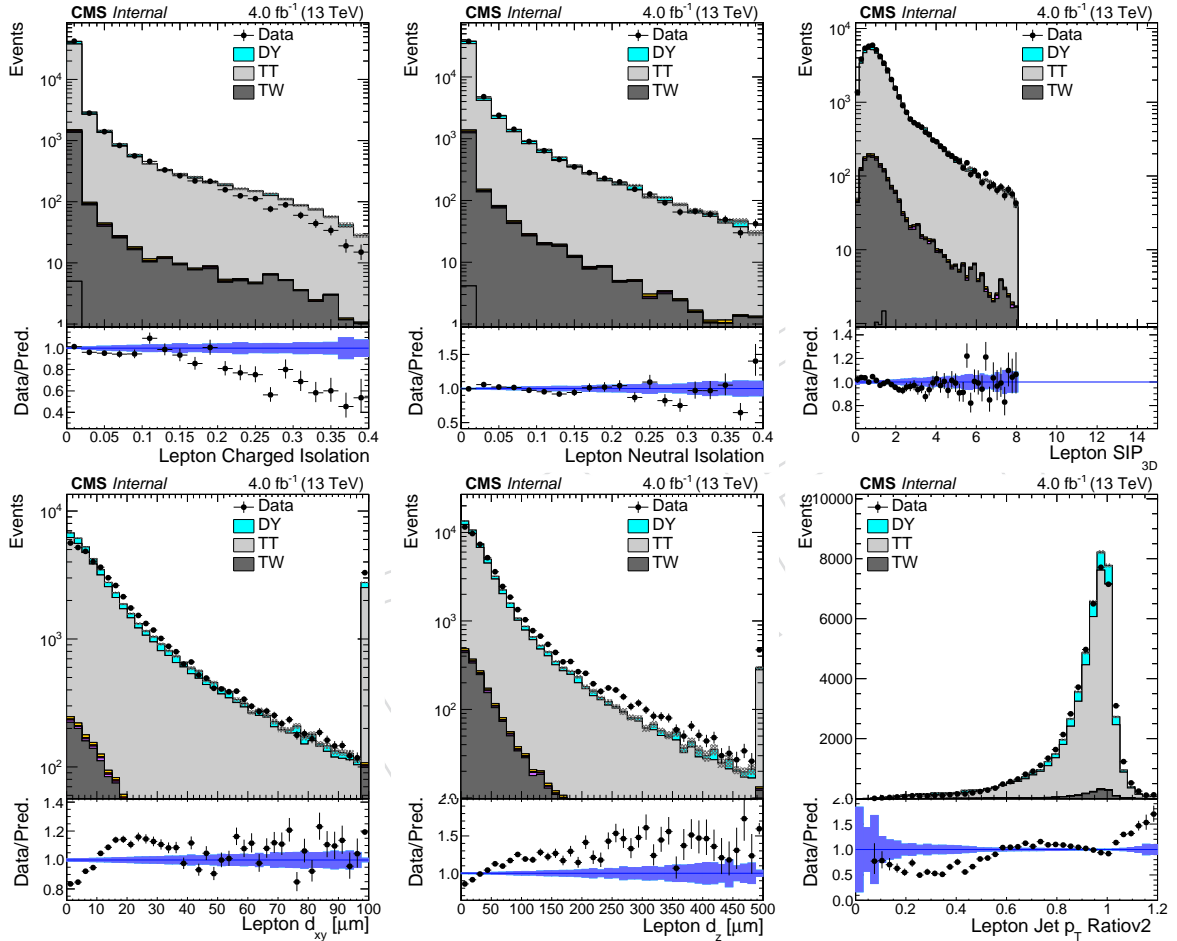


Figure 11: Summary of the input variables to the lepton MVA in a $t\bar{t}$ enriched sample, in data and simulation. The uncertainty shown on the simulation is only statistical.

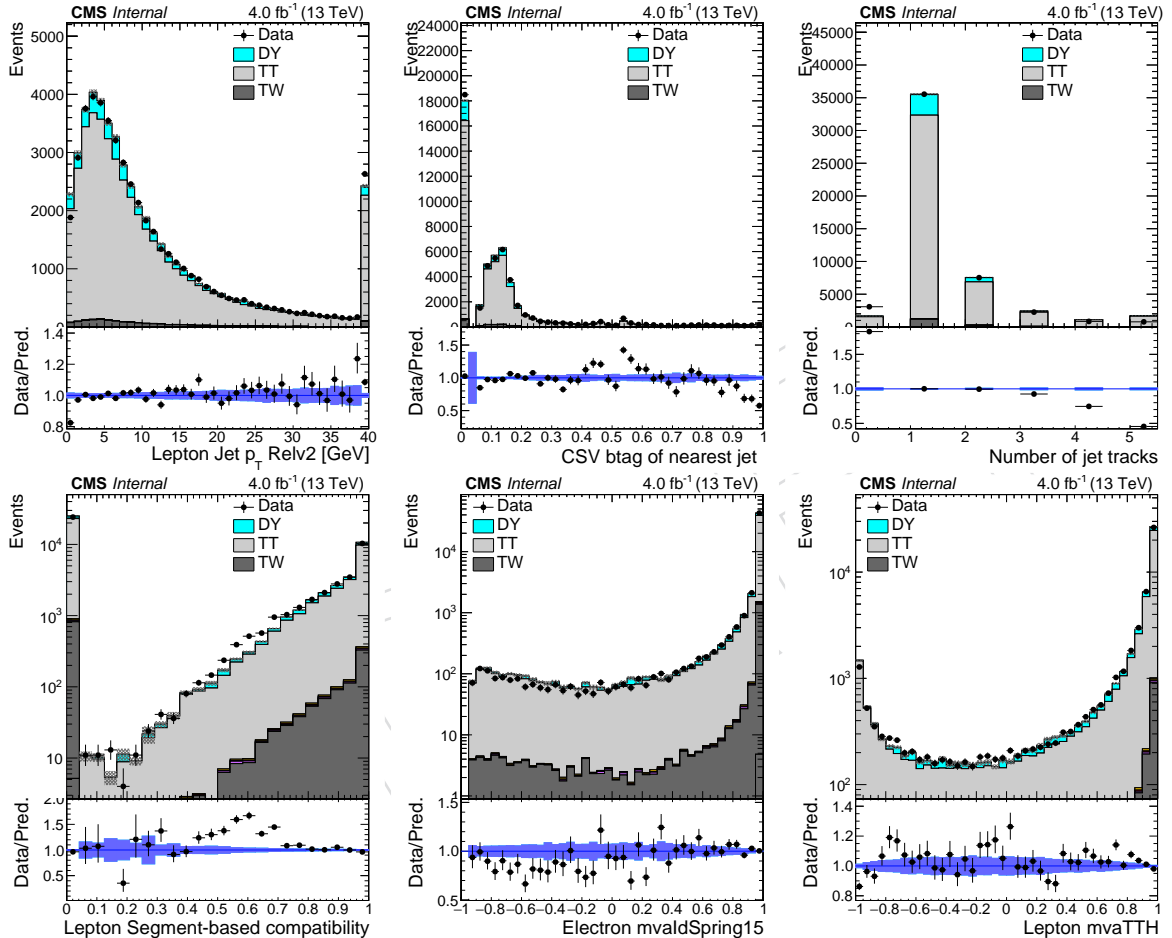


Figure 12: Summary of the input variables (continued) to the lepton MVA and output discriminator in a $t\bar{t}$ enriched sample, in data and simulation. The uncertainty shown on the simulation is only statistical.

328 **3.4.1 Loose selection efficiency**

The reconstruction and loose identification efficiency are computed both for muons and electrons using the Tag and Probe technique with $Z \rightarrow \ell^+ \ell^-$ events, in data and in simulation separately. The efficiency scale factor is therefore defined as:

$$\rho(p_T, \eta) = \frac{\varepsilon_{\text{data}}(p_T, \eta)}{\varepsilon_{\text{MC}}(p_T, \eta)}, \quad (5)$$

where $\varepsilon_i(p_T, \eta)$ is the efficiency measured for a given lepton in the process i (data or simulation). The scale factor is used afterward to correct the weight of the simulated event. The full simulation correction from the lepton side is thus given by the product of all scale factors :

$$\rho = \prod_{j \in \text{leptons}} \prod_{i \in \text{efficiencies}} \rho_i(p_T(j), \eta_j) \quad (6)$$

329 We apply scale factors for the loose electron selection efficiency that have been derived in the
 330 context of the SUSY lepton SF working group. Figure 13 shows the scale factors for the loose
 331 muon selection. The efficiency of tight selection cuts has been measured with the same pro-
 332 cedure, with respect to the loose selection. Systematics on these scale-factors related to the
 333 method have been evaluated and are of the order of 2% for both lepton flavors, in all the con-
 334 sidered kinematic range. These results have derived with Muon and EGamma POG official
 335 tools and are described in details here [27], *on a subset (4.0fb^{-1}) of the data used for extracting the*
 336 *results presented in this note. We expect to update to more recent versions of the scale factors when they*
 337 *will become available.*

338

339 **3.4.2 Tight vs Loose selection efficiency**

340 The efficiencies of applying the tight selection as defined in Tables 6 and 7, on the loose leptons
 341 are determined using a tag and probe method on a sample of DY-enriched events. The denom-
 342 inator definitions for these efficiencies includes the $SIP_{3D} < 8$ as it is already included in the
 343 loose lepton efficiencies described in Section 3.4.1. Numerator cuts for the same-sign dilepton
 344 efficiencies include the tight-charge requirement.

345 Number of passed and failed probes are determined from a fit to the invariant mass of the
 346 dilepton system. The resulting efficiencies are shown in Figures 14, 15, 16, and 17.

347 We use these (η, p_T) dependent scale factors to correct the simulation. A flat uncertainty of 3%
 348 which is of the order of the current statistical uncertainty is assigned to these scale factors.

349 **3.5 Taus**

350 Hadronically decaying taus (τ_h) are reconstructed using the hadron-plus-strips algorithm [28].
 351 τ_h candidates are required to pass the “decay mode finding” discriminator, either being recon-
 352 structured in 1- or 3-prong decay modes with or without additional π^0 ’s. In addition, they have
 353 to fulfill $p_T > 20 \text{ GeV}$ and $|\eta| < 2.3$, following Tau POG recommendations.

354 The tau identification criteria applied are based on a tau discriminator, using an MVA specifi-
 355 cally trained with $t\bar{t}$ and $t\bar{t}H$ events with an isolation cone of $\Delta R = 0.3$ [29], which increases the
 356 efficiency of the tau isolation in $t\bar{t}H$ with respect to the default discriminators using an isolation
 357 cone of $\Delta R = 0.5$. The medium working point is used for the tau selection (“byMediumIsola-
 358 tionMVArun2v1DBdR03oldDMwLT”).

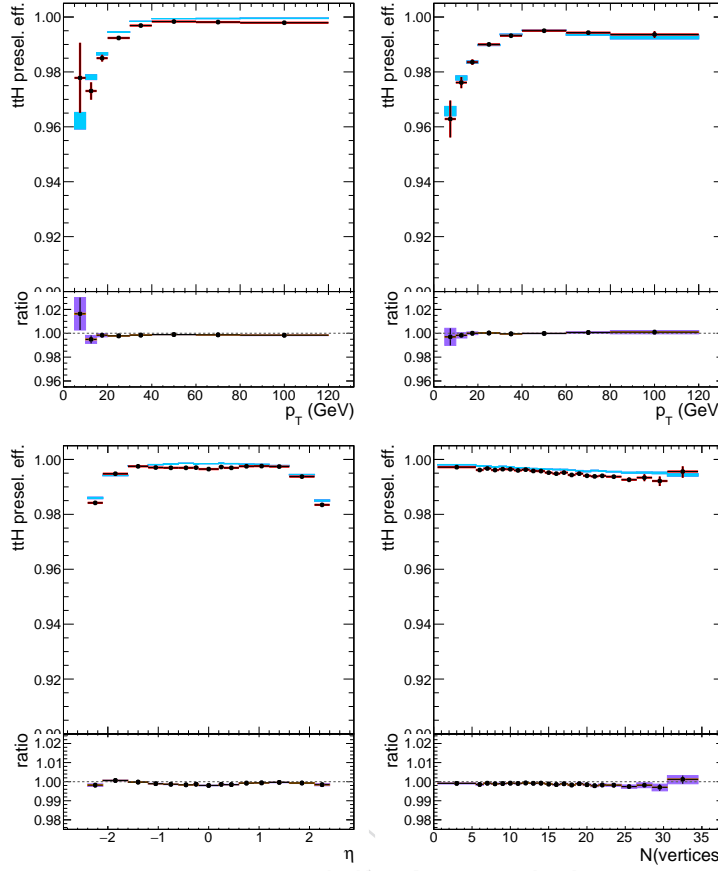


Figure 13: From left to right: muon data and simulation efficiency for the preselection ($\text{SIP} < 8$, $\text{miniRelIso} < 0.4$) requirement in the barrel and endcap regions, and muon data and simulation efficiency for the loose impact parameters cuts.

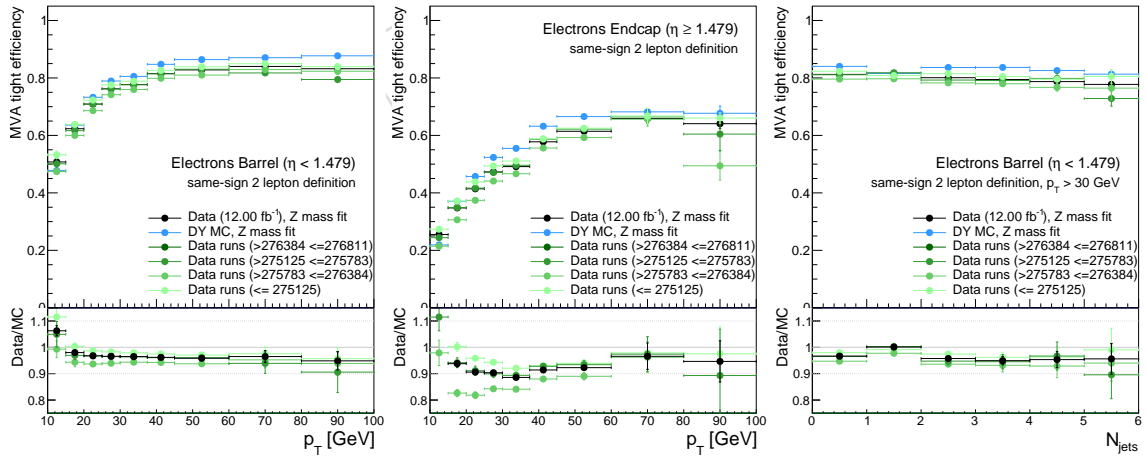


Figure 14: Tight vs loose selection efficiencies for electrons, for the same-sign dilepton lepton definition (i.e. including the tight-charge requirement).

359 Reconstructed τ_h candidates are removed if they overlap within $\Delta R = 0.4$ with *loose* electrons
 360 or muons. No dedicated discriminators against background from prompt electrons and muons
 361 are applied since the contribution from background events with additional prompt electrons
 362 and muons passing the τ_h selection criteria but not the muon and electron pre-selection require-

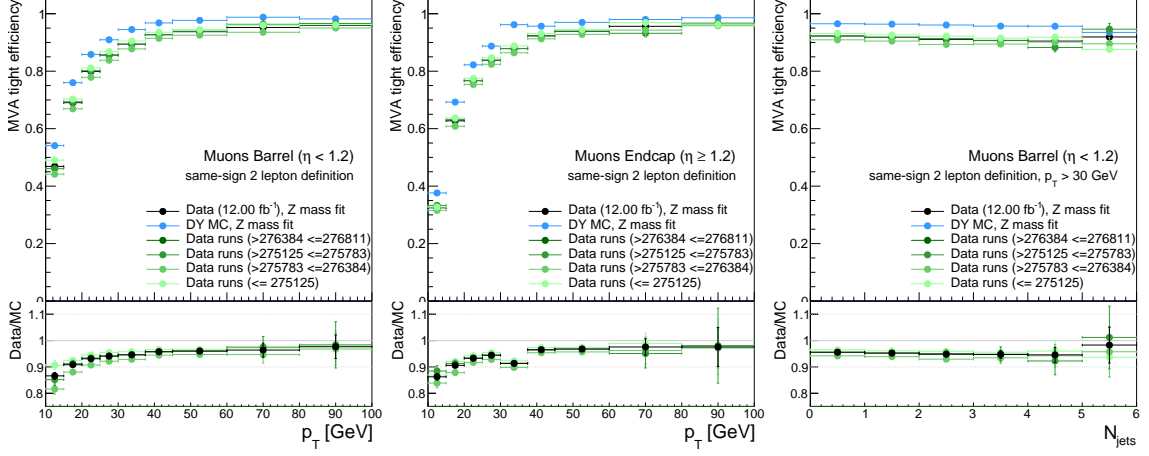


Figure 15: Tight vs loose selection efficiencies for muons, for the same-sign dilepton lepton definition (i.e. including the tight-charge requirement).

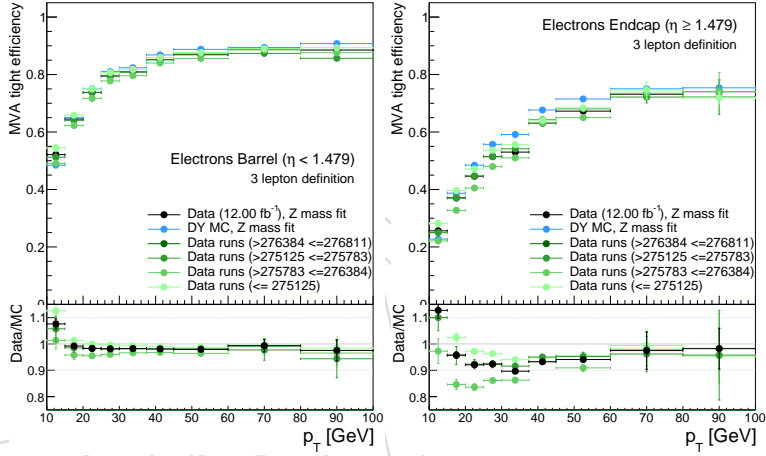


Figure 16: Tight vs loose selection efficiencies for electrons, for the three lepton channel (i.e. not including the tight-charge requirement).

363 ments is negligible.

364 4 Event selection

365 The event selection aims at rejecting events that do not match the decay signatures targeted
366 by this analysis. We require that at least two leptons passing the tight selection are present in
367 the event. Moreover, events where a pair of loose leptons with an invariant mass smaller than
368 12 GeV is found are rejected, as they are not modeled by the simulation.

369 For all events passing the selection, we require at least two jets with transverse momentum
370 greater than 25 GeV be reconstructed in the $|\eta| < 2.4$ region. We also require that both jets
371 satisfy the loose working point of the CSV b-tag algorithm, or that at least one of them satisfies
372 the medium working point, as a top quark pair decaying into b-jets is present in all signal
373 events.

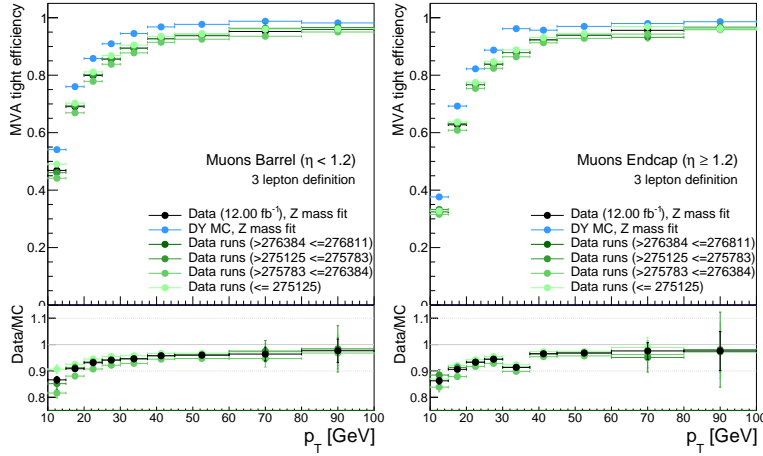


Figure 17: Tight vs loose selection efficiencies for muons, for the three lepton channel (i.e. not including the tight-charge requirement).

4.1 Two lepton same-sign category

In events where no additional tight lepton with a transverse momentum greater than 10 GeV is present, we require that the two tight leptons have the same charge and transverse momenta greater than 25 GeV and 10 GeV respectively. These events constitute the two lepton same-sign ($2lss$) category of the analysis. If the sub-leading lepton is an electron, and only for this category, its transverse momentum requirement is tightened to 15 GeV.

In addition to the requirements described above, we discard $2lss$ events that contain less than four jets with transverse momentum greater than 25 GeV and $|\eta| < 2.4$ in the final state.

The event is also rejected if the two selected leptons do not pass the requirements aimed at rejecting leptons from conversions and those on the quality of the charge measurement described in Section 3. The background from electrons from Z decays, where the charge of one electron is mismeasured, is further reduced by vetoing events where the di-electron invariant mass differs by less than 10 GeV from the Z mass. For the same reason, we also require that the $E_T^{\text{miss}} LD$ variable is larger than 0.2 in di-electron events.

4.2 Three lepton category

The three lepton ($3l$) category consists of events that contain three tight leptons with a transverse momenta greater than 20, 10 and 10 GeV respectively. No requirement is applied on the possible presence of an even larger number of leptons; i.e., this category implicitly includes events with four or more leptons.

In order to reject backgrounds from processes with Z bosons in the final state, we require that no pair of same-flavor opposite-sign loose leptons has an invariant mass closer than 10 GeV to the mass of the Z boson. We then add an $E_T^{\text{miss}} LD > 0.2$ requirement. The $E_T^{\text{miss}} LD$ threshold is tighter (0.3) if the event has a pair of leptons with the same flavor and opposite sign. For events with large jet multiplicity (≥ 4 jets), where the contamination from the Z background is smaller, no requirement on $E_T^{\text{miss}} LD$ is applied. The event is also rejected if the three selected leptons do not pass the conversion veto requirements, or if the sum of their charges is not equal to +1 or -1.

The observed event yields in data for each final state and the expectations from the different physical processes are summarised in table 8.

	$\mu\mu$	ee	$e\mu$	3ℓ
$t\bar{t}W$	18.87 ± 0.87	7.49 ± 0.56	26.25 ± 1.07	12.79 ± 0.70
$t\bar{t}Z/\gamma^*$	5.81 ± 0.52	7.70 ± 0.68	16.14 ± 1.28	24.44 ± 0.97
WZ	1.15 ± 0.18	0.98 ± 0.18	2.30 ± 0.26	5.13 ± 0.36
rare SM bkg.	1.59 ± 0.55	1.10 ± 0.37	2.42 ± 0.61	4.69 ± 0.74
WW same-sign	1.15 ± 0.07	0.49 ± 0.04	1.52 ± 0.08	
non-prompt (MC)	25.68 ± 1.53	11.96 ± 1.08	44.12 ± 1.93	30.58 ± 1.40
charge mis-ID (MC)		5.84 ± 1.79	7.03 ± 1.82	
non-prompt (data-driven)	33.37 ± 1.20	23.11 ± 1.11	61.90 ± 1.73	51.17 ± 1.80
charge mis-ID (data-driven)		6.67 ± 0.14	9.91 ± 0.14	
all backgrounds (MC)	54.25 ± 1.93	35.57 ± 2.31	99.79 ± 3.20	77.63 ± 2.01
all backgrounds (data-driven)	61.94 ± 1.67	47.54 ± 1.49	120.44 ± 2.50	98.22 ± 2.31
$t\bar{t}H$	9.04 ± 0.77	3.42 ± 0.48	10.17 ± 0.93	12.45 ± 0.86
data	74	45	154	106

Table 8: Expected and observed yields after the selection in all final states. The rare SM backgrounds include ZZ, triboson, tttt, tbZ, $W^\pm W^\pm qq$, and WW produced in double-parton interactions. Uncertainties are statistical only.

403 Figures 18-28 and 29-32 show the main event observables (lepton and jet multiplicities and
404 spectra, energy sums) for events passing the 2ℓ and 3ℓ selections.

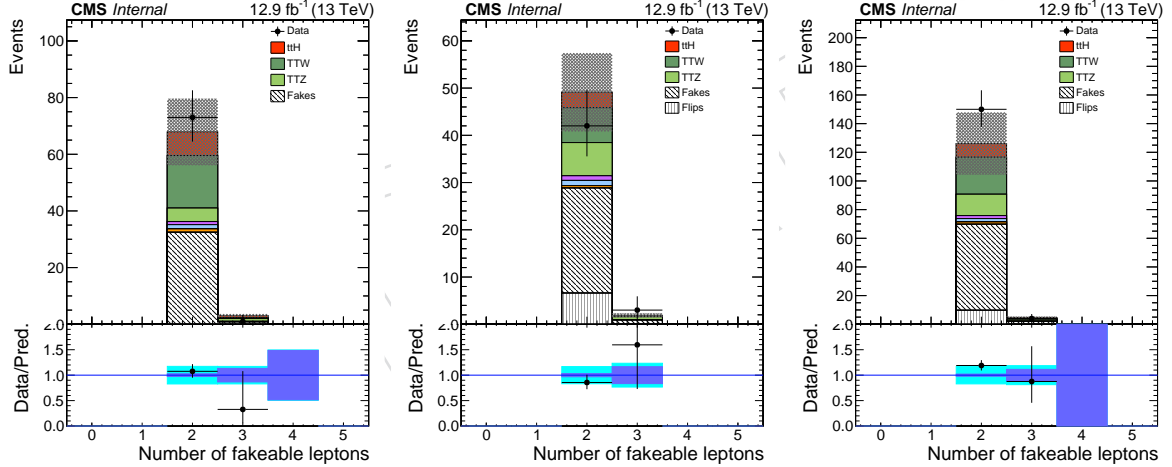


Figure 18: Number of leptons passing the fakeable object requirements in the 2ℓ ($\mu\mu$, ee , $e\mu$) selections.

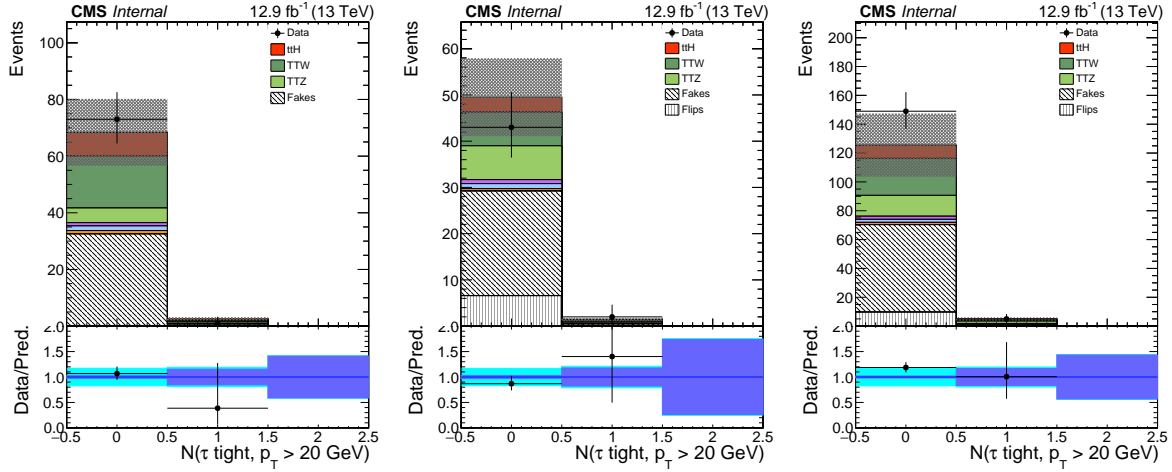


Figure 19: Number of reconstructed τ_h leptons passing the requirements described in Section 3.5 in the 2ℓ ($\mu\mu$, ee , $e\mu$) selections.

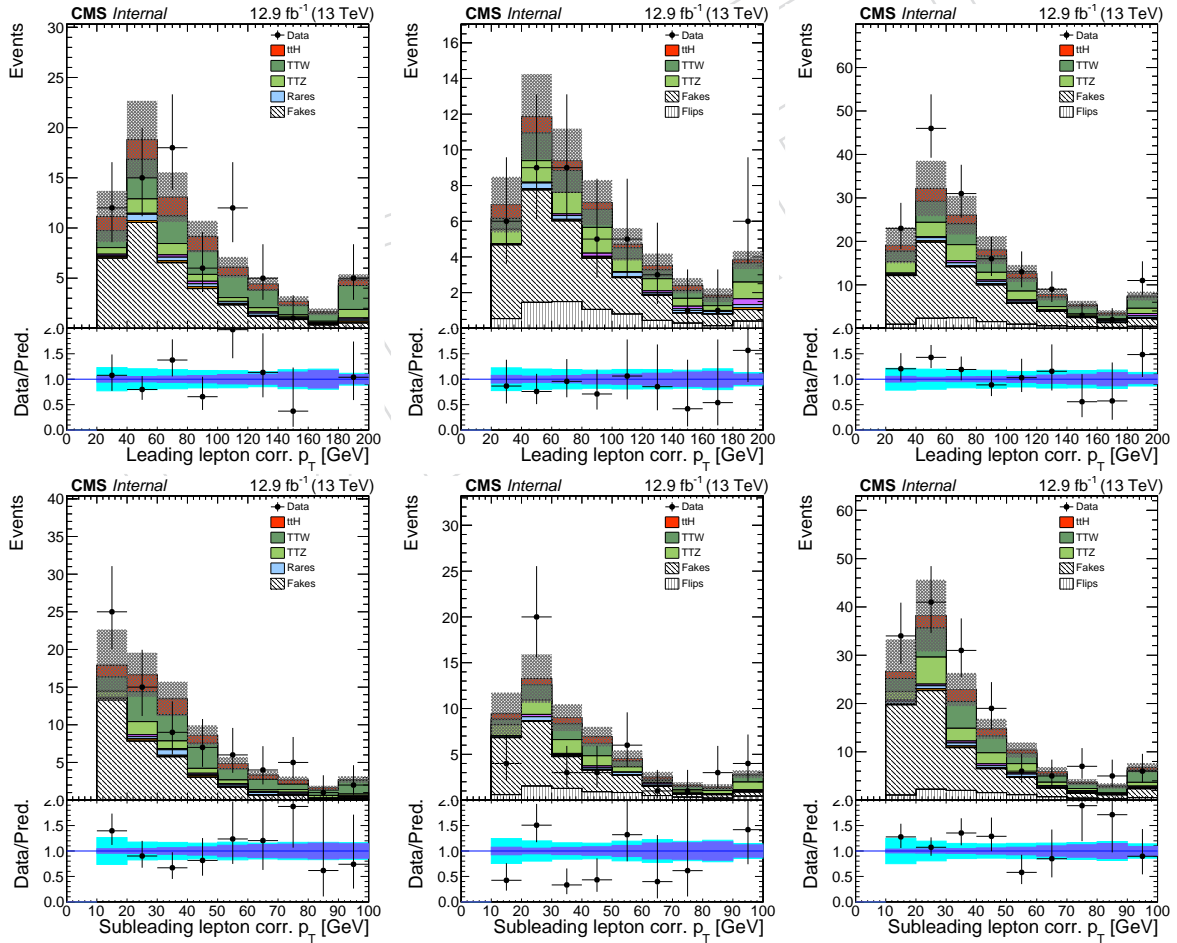
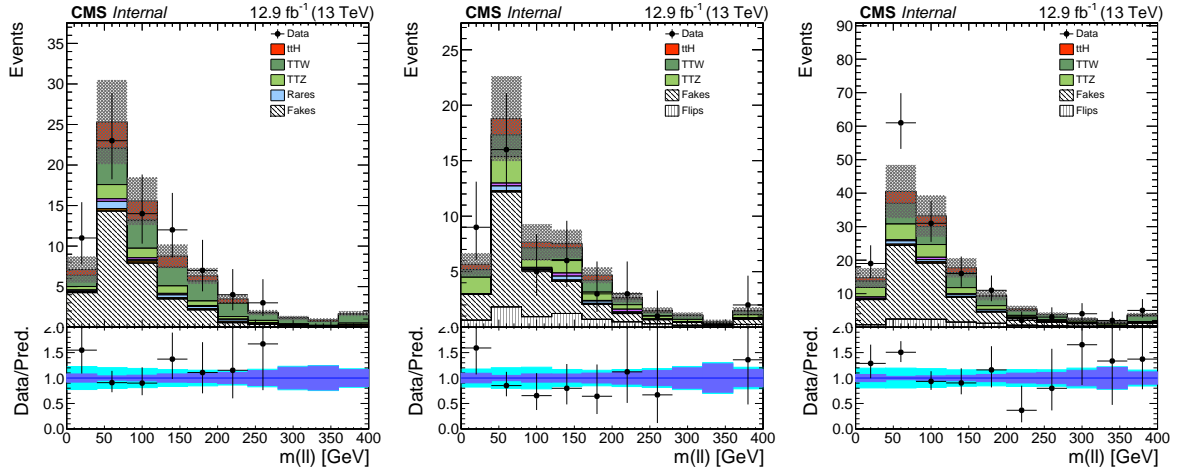
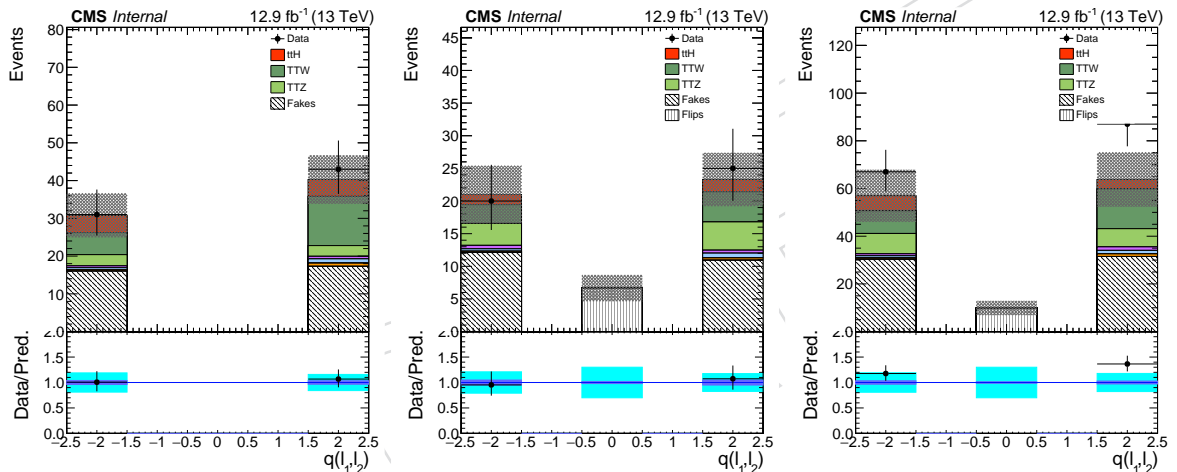
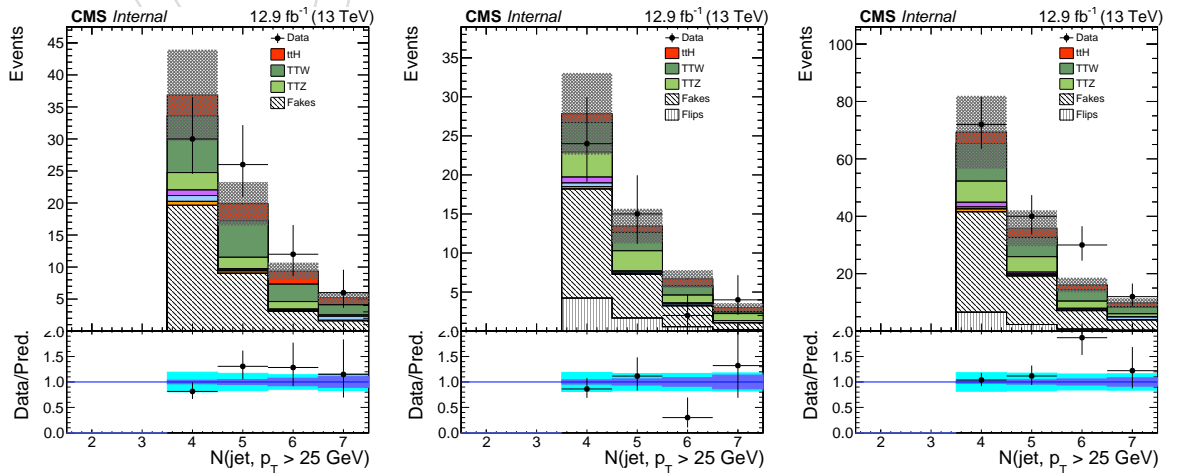


Figure 20: Lepton transverse momentum spectra in the 2ℓ ($\mu\mu$, ee , $e\mu$) selections.

Figure 21: Di-lepton invariant mass spectra in the 2ℓ ($\mu\mu$, ee , $e\mu$) selections.Figure 22: Sum of lepton charges in the 2ℓ ($\mu\mu$, ee , $e\mu$) selections.Figure 23: Jet multiplicity in the 2ℓ ($\mu\mu$, ee , $e\mu$) selections.

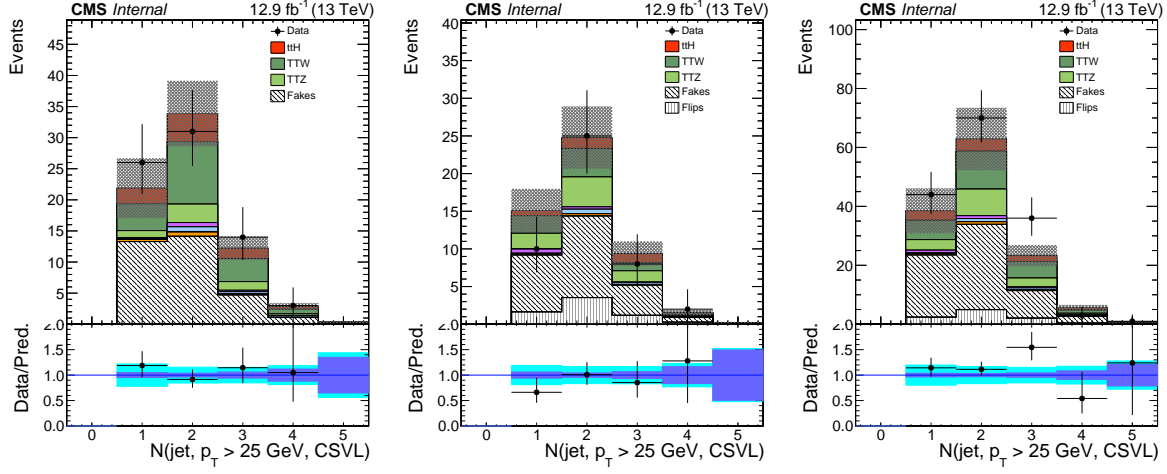


Figure 24: Multiplicity of jets passing the loose working point of the CSV tagger in the 2ℓ ($\mu\mu$, ee , $e\mu$) selections.

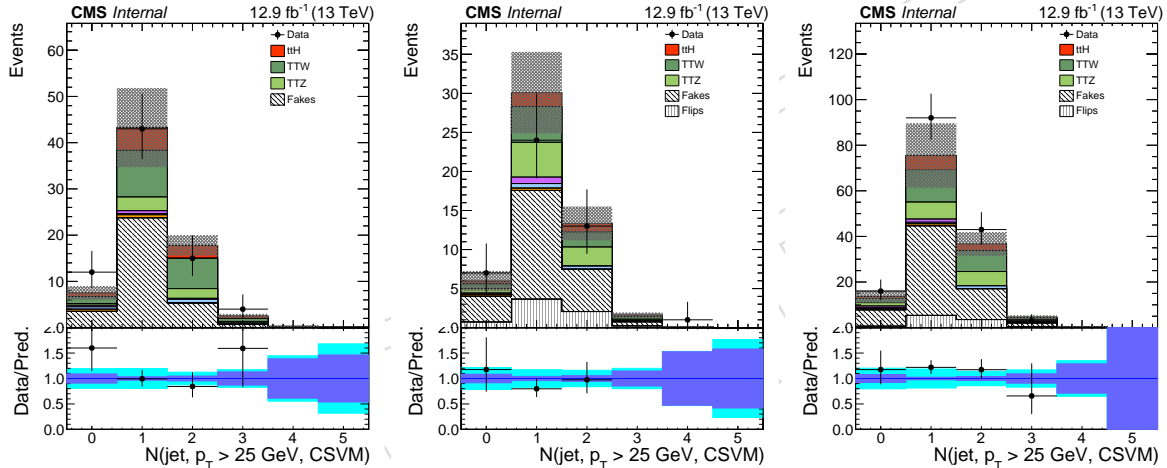


Figure 25: Multiplicity of jets passing the medium working point of the CSV tagger in the 2ℓ ($\mu\mu$, ee , $e\mu$) selections.

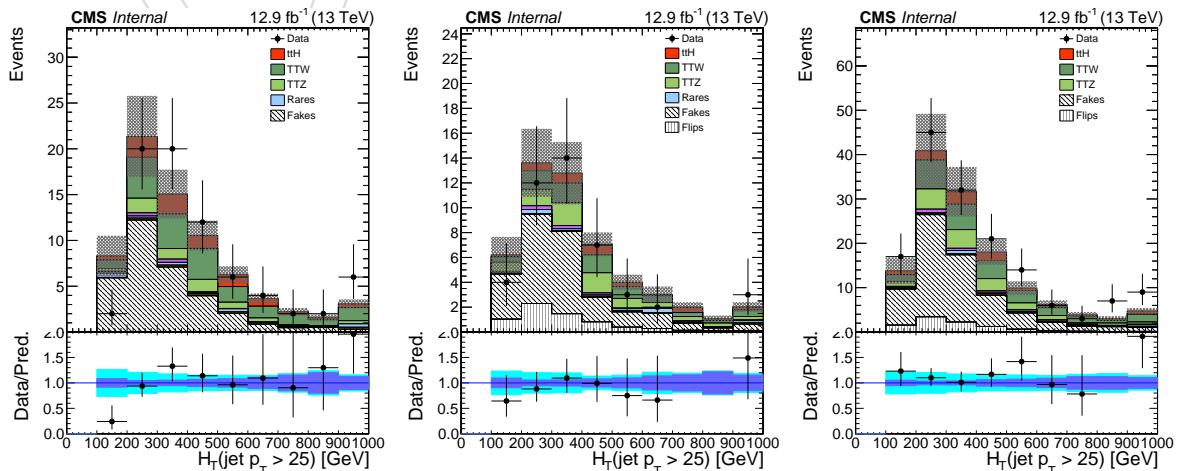
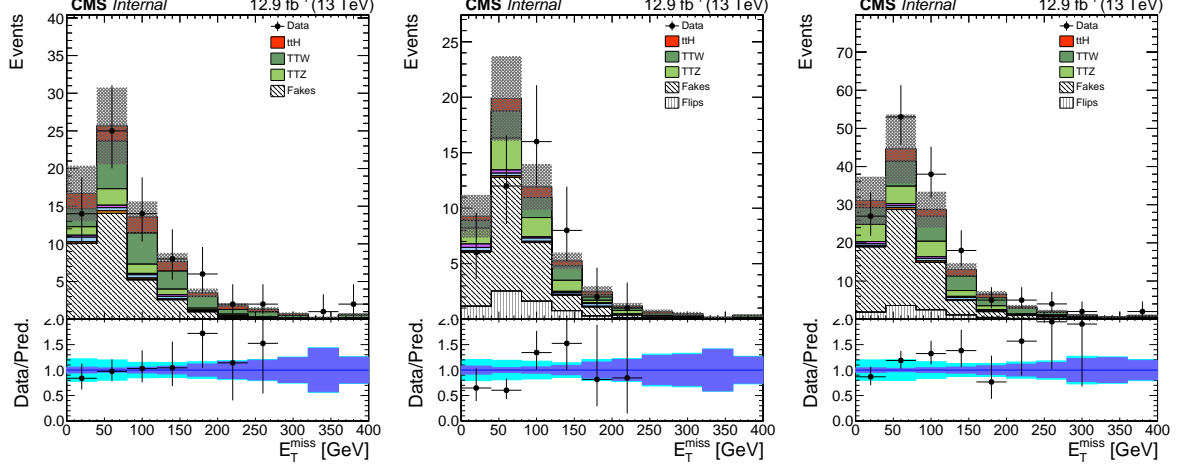
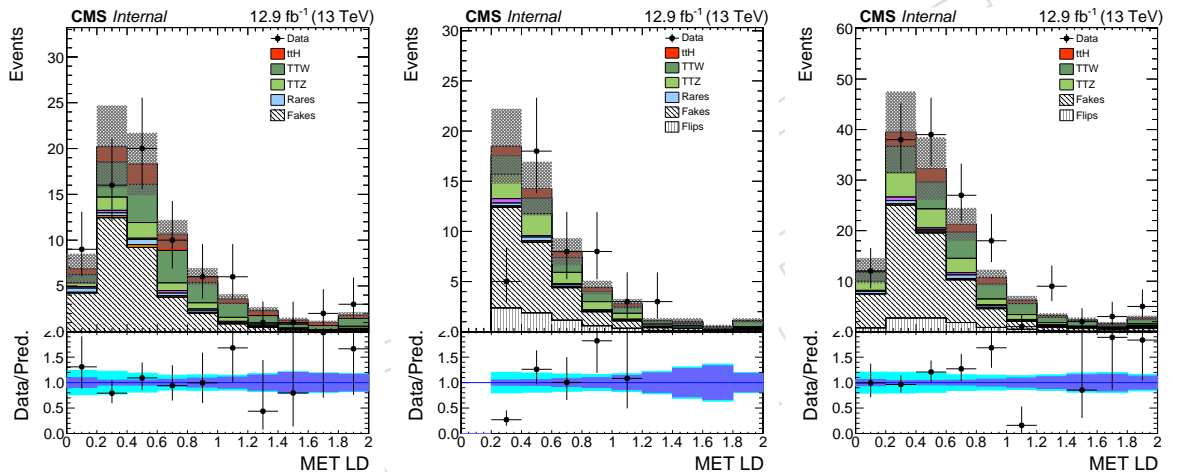
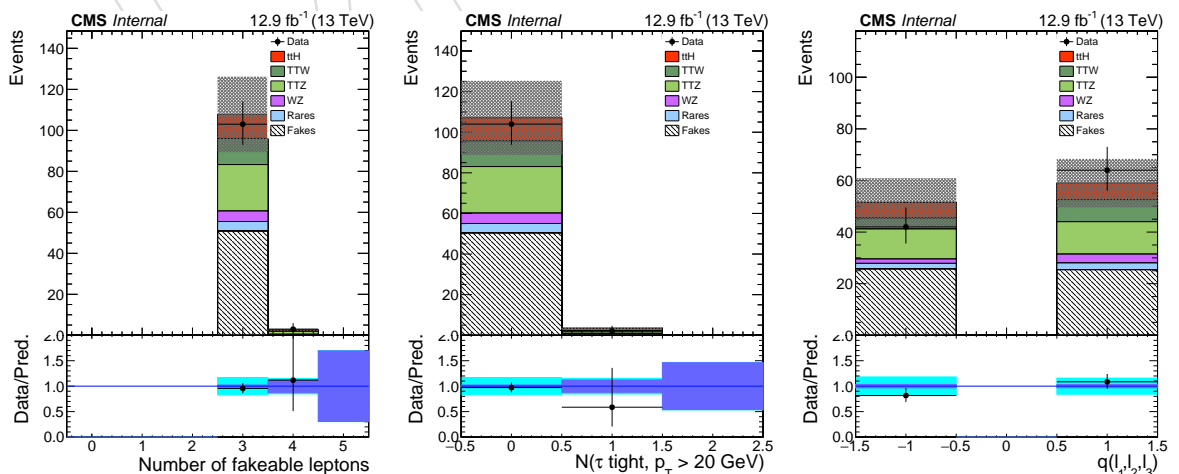


Figure 26: H_T spectra in the 2ℓ ($\mu\mu$, ee , $e\mu$) selections.

Figure 27: E_T^{miss} spectra in the 2ℓ ($\mu\mu$, ee , $e\mu$) selections.Figure 28: E_T^{miss} LD spectra in the 2ℓ ($\mu\mu$, ee , $e\mu$) selections.Figure 29: Number and charge of leptons passing the fakeable object requirements and τ_h leptons passing the requirements described in Section 3.5 in the 3ℓ selection.

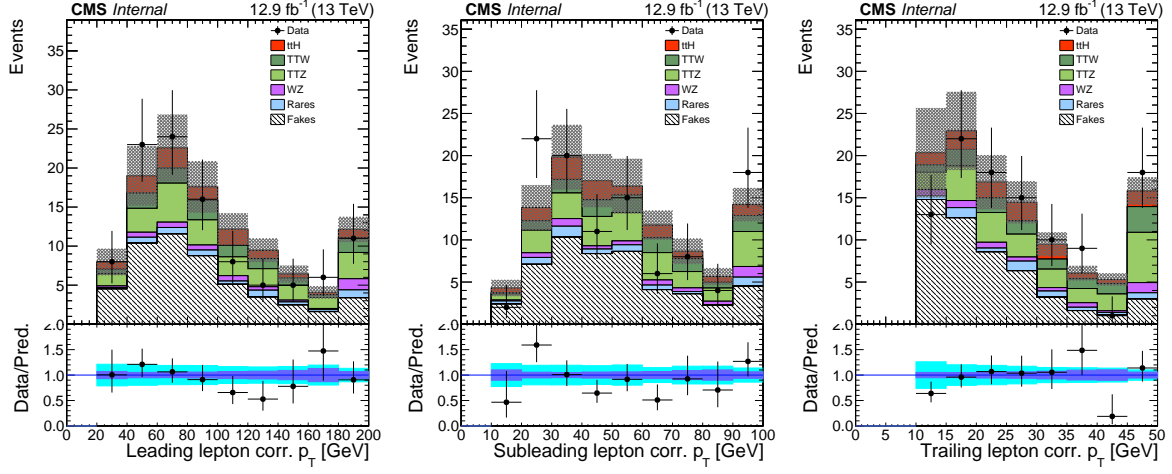


Figure 30: Lepton transverse momentum spectra in the 3ℓ selection.

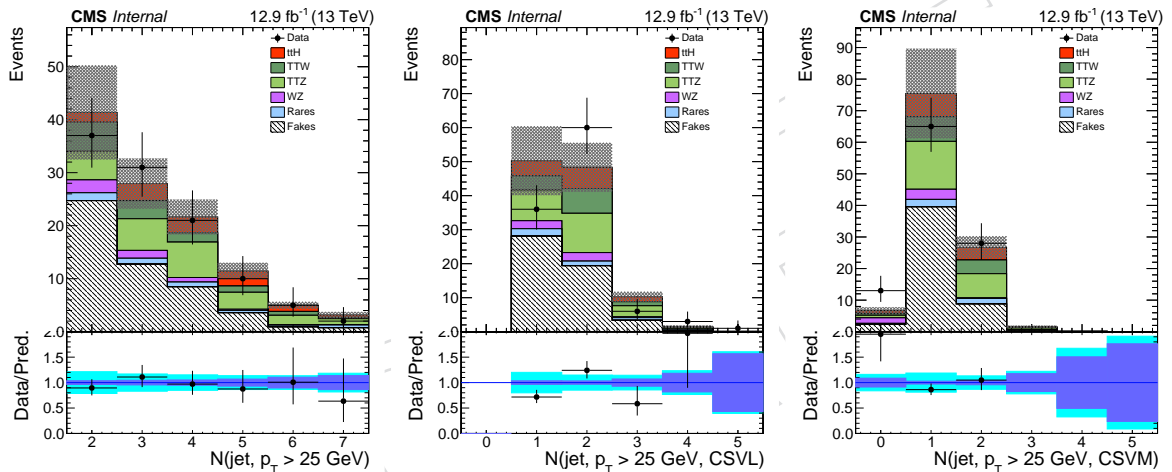


Figure 31: Jet multiplicities (all jets, jets passing the loose working point of the CSV tagger, jets passing the medium working point of the CSV tagger) in the the 3ℓ selection.

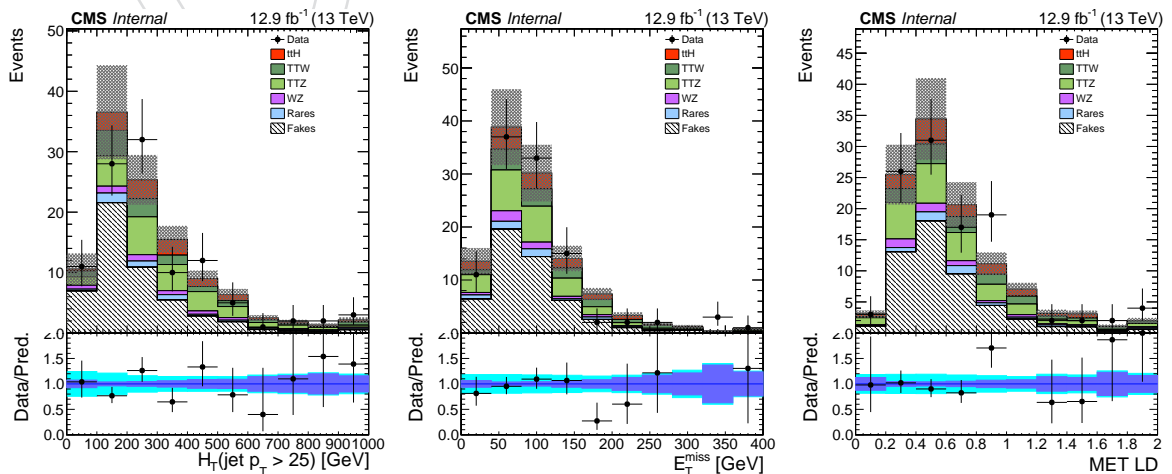


Figure 32: H_T , E_T^{miss} and $E_T^{\text{miss}} LD$ distributions in the 3ℓ selection.

405 5 Signal extraction

406 Despite the event selection requirements previously described, the post-selection yields are
 407 still dominated by the backgrounds, and have insufficient statistics to determine the presence
 408 of the $t\bar{t}H$ signal, making further discrimination necessary. The approach adopted in this search
 409 is to split the selected events into several mutually exclusive categories with different signal to
 410 background ratios. In each of these categories the signal is extracted from the distribution of a
 411 suitable discriminating variable.

412 In order to exploit the topological characteristics and specificities of the $t\bar{t}H$ signal with respect
 413 to the most dominant backgrounds, the output of the boosted decision tree (BDT), trained
 414 using a selection of kinematic variables, is used as the discriminating variable for the signal
 415 extraction. In this analysis, the samples used for BDT training and evaluation are from the
 416 2015 analysis. The generator-level information in the 2015 samples, produced in the RunI-
 417 IFall15MiniAODv2 (CMSSW 76X) campaign and described in [25], is identical to the current
 418 samples used in the RunIISpring16MiniAODv1 (CMSSW 80X) campaign. Therefore any po-
 419 tential difference in kinematics is currently neglected. In later versions of this note, the BDT
 420 training and evaluation will be repeated using the RunIISpring16MiniAODv1 samples.

421 Both final states with two same sign leptons ($2lss$) and at least three leptons ($\geq 3l$) have dom-
 422 inant backgrounds originating from the $t\bar{t}$ and $t\bar{t}V(V=W/Z)$ processes. In order to have an
 423 efficient discrimination against both of these processes, a two-dimensional (2D) BDT approach
 424 is introduced. For each of the $2lss$ and $\geq 3l$ final states, the BDT is separately trained against
 425 the $t\bar{t}$ and $t\bar{t}V$, selecting a set of kinematic variables that provide the largest separation in each
 426 training. The BDT outputs of the training against these two processes are used to construct the
 427 2D space, effectively a scatter plot of the two discriminators. The consequent 2D distribution
 428 is then partitioned to rectangular sectors and $t\bar{t}H$ signal and background contributions of each
 429 sector are summed and folded to a one-dimensional histogram. With a convenient partitioning
 430 of the 2D space, the resulting difference of the signal and background shapes is enhanced with
 431 respect to the one-dimensional case, for example against the $t\bar{t}$, and that is provided by the
 432 training of the additional BDT, against the $t\bar{t}V$ process.

433 In the two same sign lepton category and for the training against the $t\bar{t}$ background, the input
 434 variables are the following: the maximum absolute pseudorapidity of the two leading leptons,
 435 the multiplicity of hadronic jets, the minimum distance between the leading lepton and closest
 436 jet, the minimum distance of the trailing lepton and closest jet, the missing transverse energy,
 437 the average separation between the two jets and the transverse mass of the leading lepton and
 438 missing transverse energy. The training against the $t\bar{t}V$ process relies of the following variables:
 439 the maximum absolute pseudorapidity of the two leading leptons, the transverse mass of the
 440 leading lepton and missing transverse energy, the multiplicity of hadronic jets, the minimum
 441 distance between the leading lepton and closest jet, the minimum distance of the trailing lepton
 442 and closest jet, the leading lepton transverse momentum and the trailing lepton transverse
 443 momentum. The training is performed using a relaxed event selection, that require at least two
 444 preselected same sign leptons with leading and trailing lepton transverse momentum larger
 445 than 20 and 10 GeV, respectively, then either two loose selected b-jets or one medium b-tagged
 446 jet and also at least four jets in the event. Figure 33 shows a comparison of the simulated
 447 signal ($t\bar{t}H$) and background ($t\bar{t}$ or $t\bar{t}V$) processes for each of the input variables to the BDT
 448 discriminator.

449 The three lepton category has the following variables for the training against the $t\bar{t}$ background:
 450 the maximum absolute pseudorapidity of the two leading leptons, the transverse mass of the
 451 leading lepton and missing transverse energy, the multiplicity of hadronic jets, the missing HT,

452 the average distance of the two jets, the minimum distance between the leading lepton and
 453 closest jet and the minimum distance of the trailing lepton and closest jet. For the training
 454 against the $t\bar{t}V$ background, the input variables are: the maximum absolute pseudorapidity
 455 of the two leading leptons, the transverse mass of the leading lepton and missing transverse
 456 energy, the multiplicity of hadronic jets, the minimum distance between the leading lepton
 457 and closest jet, the minimum distance of the trailing lepton and closest jet, the leading lepton
 458 transverse momentum and the third lepton transverse momentum.

459 Furthermore, the performance of the matrix element method (MEM, as described in Appendix B,
 460 on page 78) in discriminating the $t\bar{t}H$ signal and the $t\bar{t}V$ background in the three lepton category
 461 warrants its inclusion as input to the training against the $t\bar{t}V$ processes. Therefore the logarithm
 462 of the three MEM weights for $t\bar{t}H$, $t\bar{t}W$, and $t\bar{t}Z$, are added as input to the BDT training in this
 463 category.

464 Because the currently available Monte-Carlo statistics prevent us from training with the full
 465 event selection, a relaxed selection has been applied instead for training. This relaxed selec-
 466 tion requires at least three preselected leptons where neither lepton pair has an invariant mass
 467 within 10 GeV of the mass of the Z boson, the leading, trailing and sub-trailing lepton trans-
 468 verse momentum larger than 20, 10 and 10 GeV, respectively, the MET LD requirement applied
 469 and at least two loose selected b-jets in the event. In Figure 34 a comparison of the simulated
 470 signal ($t\bar{t}H$) and background ($t\bar{t}$ or $t\bar{t}V$) processes for each of the input variables to the BDT
 471 discriminator is presented.

472 Figures 35 and 36 show the separation power of each of the BDT discriminators, while Fig-
 473 ures 37 and 38 show the distributions of these discriminators.

474 The 2D plane spanned by the output of the two discriminators is binned in order to maximize
 475 the analysis sensitivity with the available statistics, as shown in Figure 39. The binning of the
 476 2D plane is specified in the Table 9.

Table 9: Coordinates of the bins that represent the partitioning of the 2D BDT plane.

	bin 1	bin 2	bin 3	bin 4	bin 5	bin 6	bin 7
$2lss(t\bar{t})$	(-1.0, -0.2]	(-0.2, 0.1]	(0.1, 0.4]	(0.1, 0.4]	(0.4, 1.0]	(0.4, 1.0]	(0.4, 1.0]
$2lss(t\bar{t}V)$	(-1.0, 1.0]	(-1.0, 1.0]	(-1.0, 0.3]	(0.3, 1.0]	(-1.0, 0.1]	(0.1, 0.4]	(0.4, 1.0]
$3\ell(t\bar{t})$	(-1.0, -0.3]	(-0.3, 0.3]	(-0.3, 0.3]	(0.3, 1.0]	(0.3, 1.0]		
$3\ell(t\bar{t}V)$	(-1.0, 1.0]	(-1.0, 0.25]	(0.25, 1.0]	(-1.0, 0.25]	(0.25, 1.0]		

477 Figure 39 shows the event yield as a function of the bins defined above.

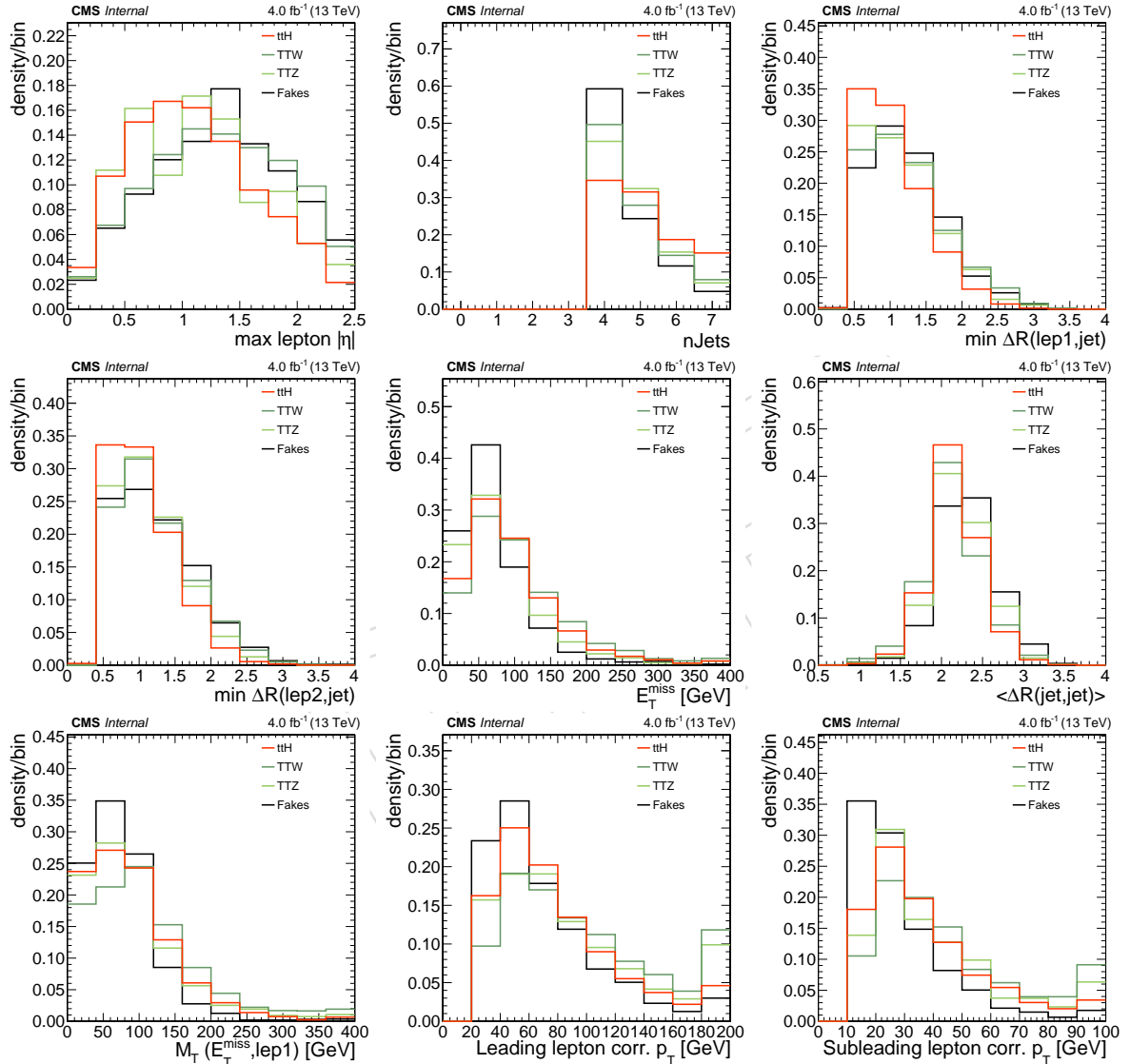


Figure 33: The separation power of the variables used for BDT trainings, in the two same sign leptons channel.

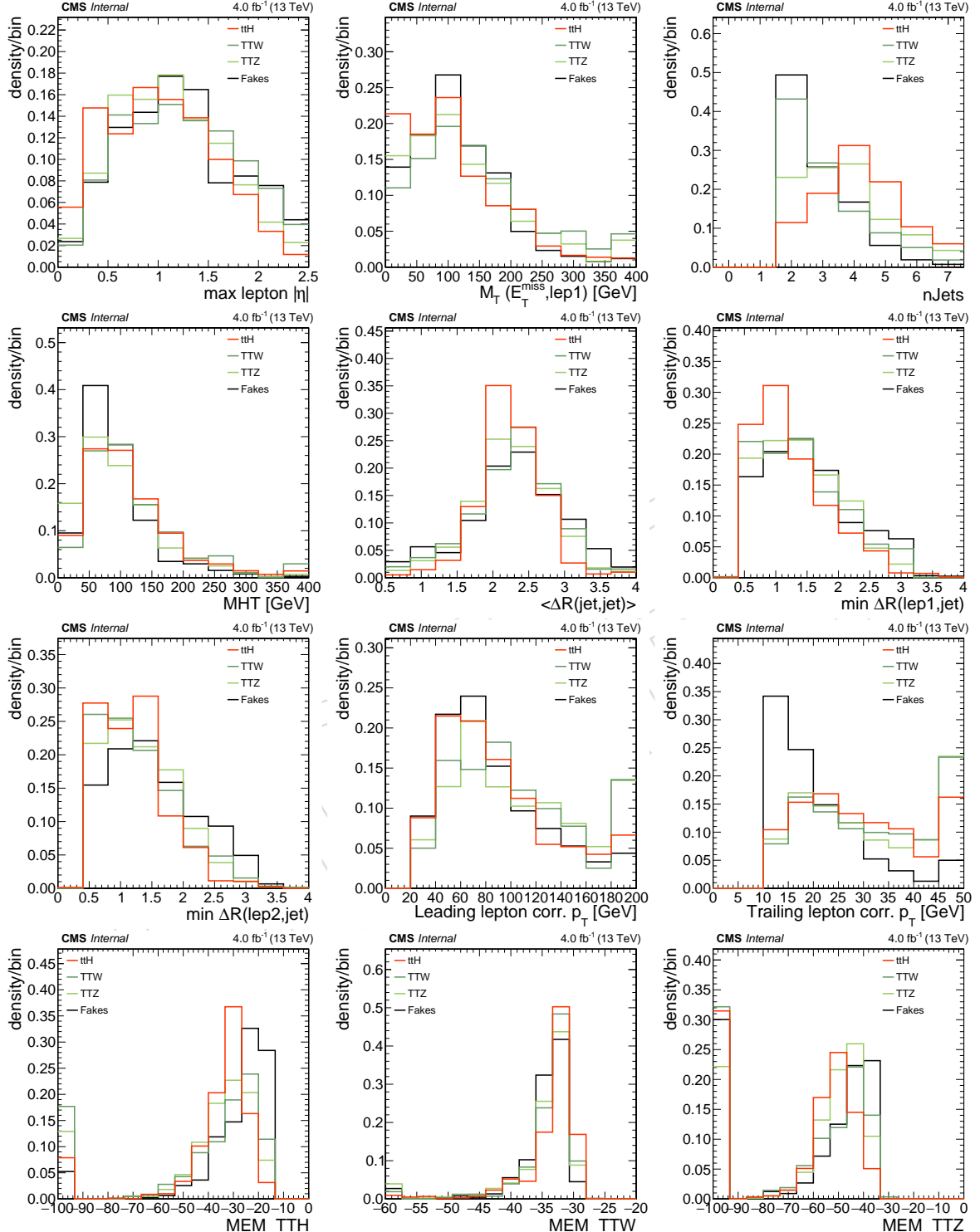


Figure 34: The separation power of the variables used for BDT trainings, in the three lepton channel.

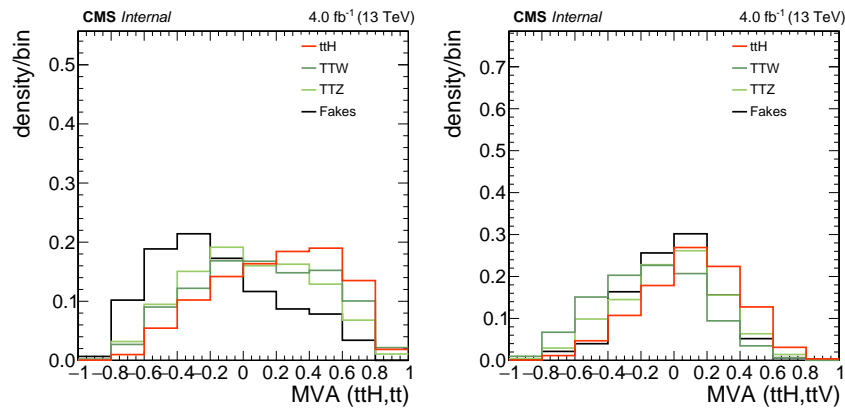


Figure 35: The separation power of the BDT output against the $t\bar{t}$ background (left) and $t\bar{t}V$ (right) background, in the two same sign leptons channel.

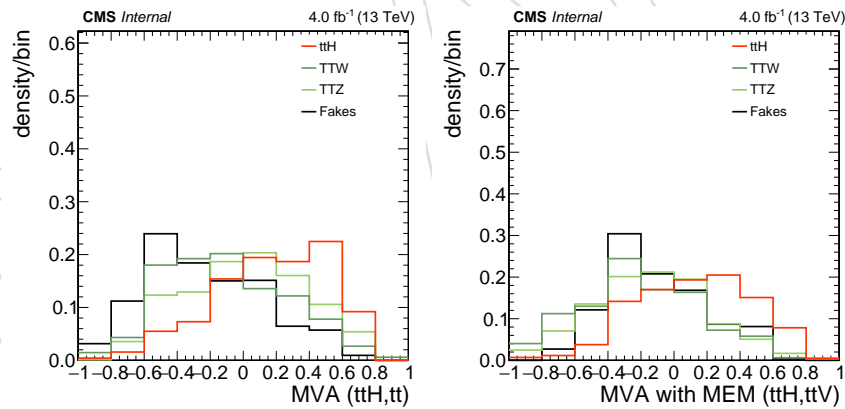


Figure 36: The separation power of the BDT output against the $t\bar{t}$ background (left) and $t\bar{t}V$ (right) background, in the three lepton channel.

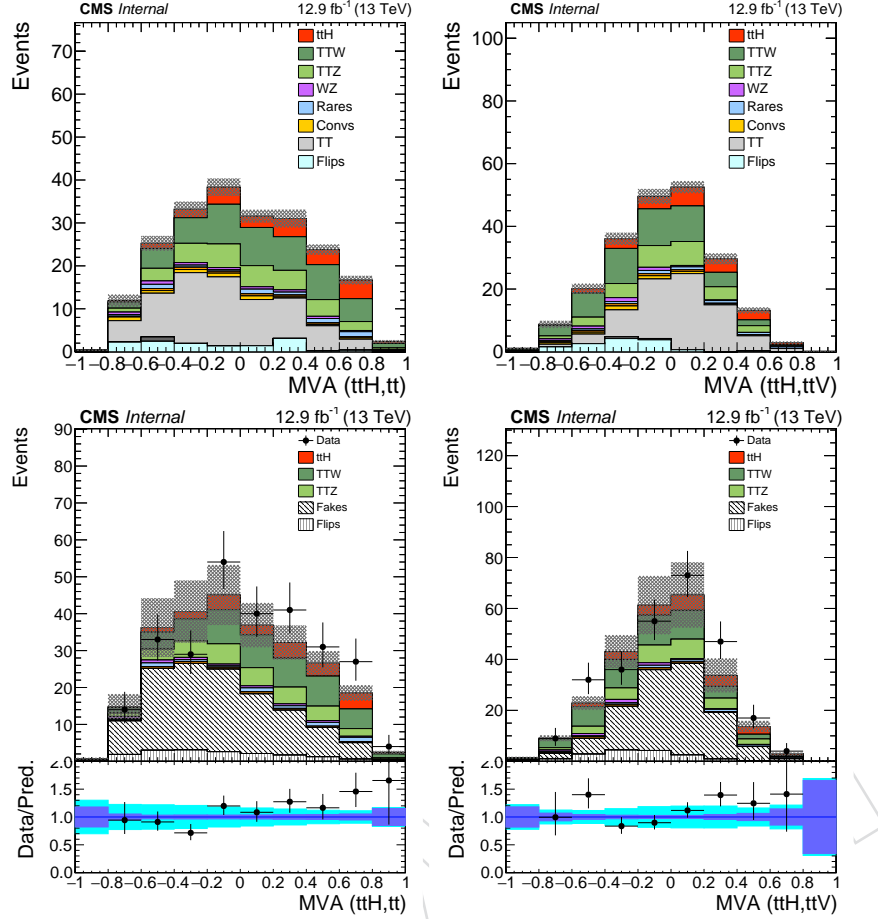


Figure 37: Distribution of the discriminator against the $t\bar{t}$ bar (left) and $t\bar{t}V$ (right) backgrounds, in the two same sign leptons channel, with reducible background prediction from MC (top) and from data (bottom).

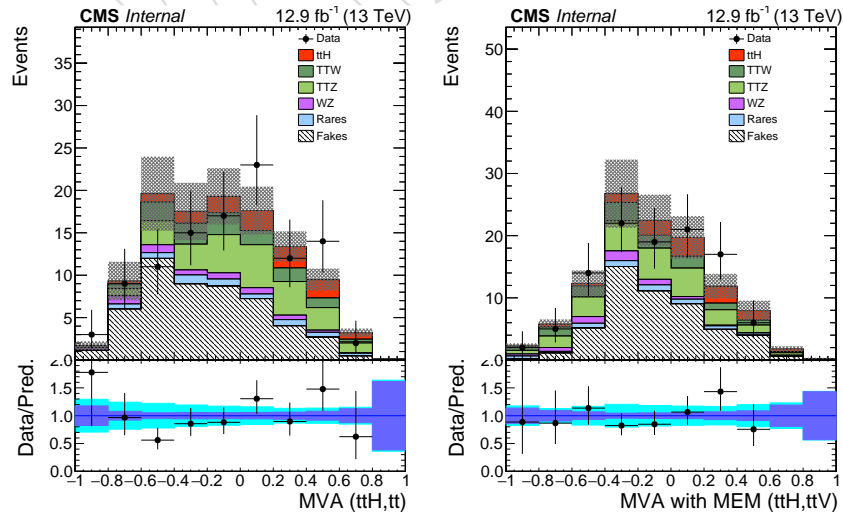


Figure 38: Distribution of the discriminator against the $t\bar{t}$ bar (left) and $t\bar{t}V$ (right) backgrounds, in the three lepton channel, with reducible background prediction from MC (top) and from data (bottom).

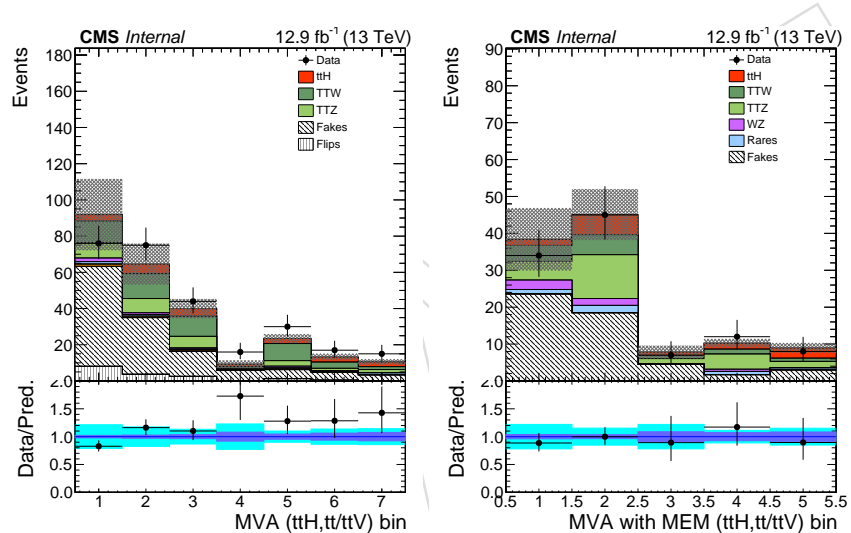


Figure 39: Binned distributions of the pair of discriminators in 2lss (left) and 3l (right) channels.

478 **5.1 Event subcategories**

479 The two same sign lepton events are further divided into categories with zero or at least one
 480 hadronic tau, as described in Section 3.3. The category with zero taus is split into lepton
 481 flavours: two electrons, two muons and electron and muon. These three categories, except
 482 the two electrons, are further divided according to the presence (or absence) of two medium
 483 tagged b-jets, the b-tight (b-loose) categories. Due to a low expected yield, the events with at
 484 least one hadronic tau are not split by flavour or b-tag and are considered inclusively.

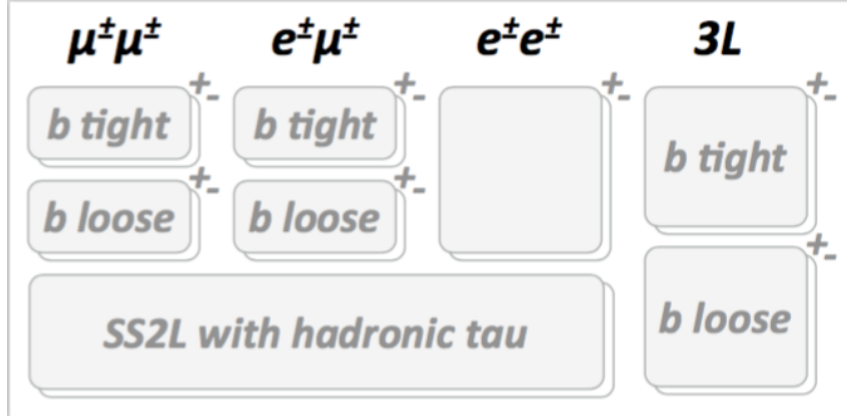


Figure 40: Diagram of all event categories in the analysis. Categories are based on lepton multiplicity and flavor, b-jet composition, and the sign of the sum of the lepton charges.

485 The events with at least three leptons are taken inclusively in terms of the requirement on the
 486 presence of hadronic taus and are only separated into the b-tight and b-loose categories.

487 Finally, to exploit the charge asymmetry present in several backgrounds (ttW, WZ, single top
 488 and W+jets), but not present in ttH, events in each of the categories described above are further
 489 categorized by the positive or negative sum of the lepton charges. The summary of all event
 490 categories is summarized in Figure 40.

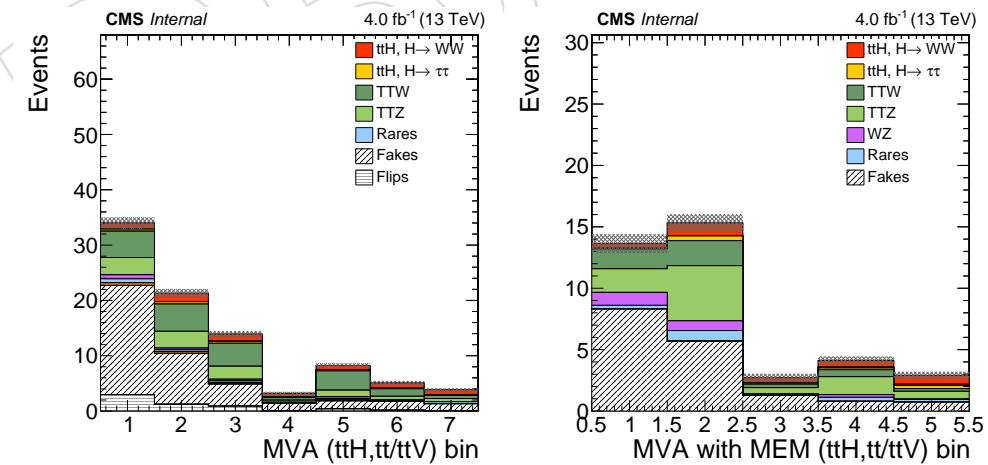


Figure 41: Decay composition of the ttH signal in 2lss (left) and 3l (right) channels.

491 6 Signal modeling

492 The signal is modelled using simulated events. In this version of the note, we present the
 493 same BDT outputs used in the 2015 analysis. The generator-level information is identical to the
 494 2015 samples, thus little change is expected. The plots in this section will be updated to reflect
 495 BDT output with 2016 samples in later versions of this note. The simulation has two different
 496 sources of systematic uncertainty. The first source of uncertainty is correction factors applied
 497 to the simulation in order to better reproduce the detector conditions and performance in data.
 498 The second source is assumptions made in the theoretical models that were used to produce
 499 the simulation. We account for uncertainties from both sources.

500 6.1 Correction factors and experimental uncertainties

501 *The results presented in this note have preliminary versions of the scale factors for lepton, b-tagging and
 502 trigger efficiency applied. We expect to update them with the corresponding version derived for the full
 503 ICHEP 2016 dataset as soon as they will become available.*

504 As discussed in Section 3, we use scale factors to correct for differences in lepton performance
 505 between data and simulation. The scale factors account for the differences in the trigger, lepton
 506 Loose and Tight selections. Each of these scale factors has an uncertainty associated with it as
 507 discussed in that section, and it's propagated in the final uncertainties on signal yields.

508

509 The corrections that we apply to jet energies in simulation have uncertainties associated with
 510 them [19]. The uncertainties are parameterised as a function of p_T , η . We assess the impact of
 511 the uncertainties by shifting the jet energy correction factors for each jet up and down by $\pm 1\sigma$
 512 and re-calculating all kinematic quantities. The effect on the shape of the BDT discriminators
 513 used in the signal extraction is shown in Fig. 42. Systematic effects both on normalization and
 514 shape are taken into account in extracting the results.

515 In the RunI analysis we found that the uncertainty from the jet energy resolution plays a negli-
 516 gible role in this analysis.

517 The uncertainties on the correction for the data/sim differences in the b-tagging performance
 518 described in 3 are parameterised as a function of p_T , η , and jet flavor. We assess their effect
 519 on the analysis by shifting the weight of each jet up and down by $\pm 1\sigma$ of the appropriate
 520 uncertainty and recalculating the overall event weight.

521 6.2 Theoretical uncertainties

522 The theoretical uncertainties on the NLO prediction for the inclusive $t\bar{t}H$ production cross sec-
 523 tion amount to +5.8–9.2% from unknown higher orders in the perturbative series and 3.6%
 524 from the knowledge of the parton distribution functions (PDFs) and α_s [30]. These uncertain-
 525 ties are propagated to the final normalization of the signal yields.

526 In addition to the overall normalisation, systematic uncertainties of theoretical origin on the
 527 distribution of the events in the final discriminating variables are considered, estimated con-
 528 ventionally by varying the normalisation and factorisation scales up and down by a factor of
 529 two and matching threshold between matrix element and parton shower (Fig. 43). In the cur-
 530 rent version of the results the shape uncertainties on the BDTs output are of the order of 2% to
 531 3%.

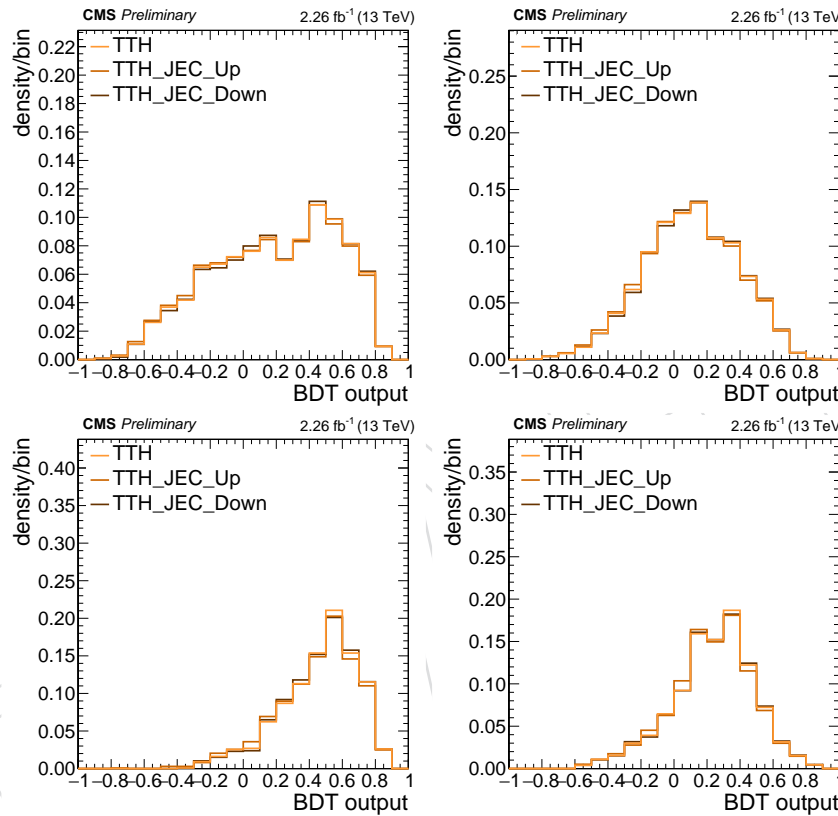


Figure 42: The BDT output distribution of the ttH signal, shown for the training against ttbar (left) and ttV (right) in the two same sign leptons (upper) and three lepton (lower) final state, with the jet energy scale variations of one standard deviation included in order to estimate the shape uncertainties.

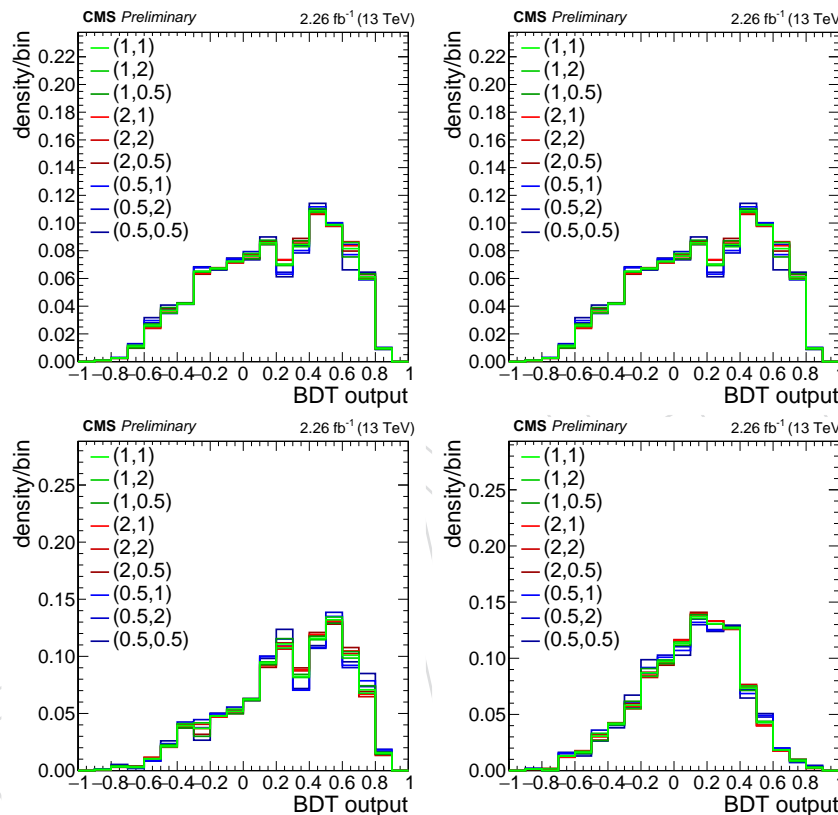


Figure 43: The BDT output distribution of the ttH signal, shown for the training against ttbar (left) and ttV (right) in the two same sign leptons (upper) and three lepton (lower) final state, with variations of the renormalization and factorization scale included in order to estimate the shape uncertainties.

532 7 Background predictions

533 7.1 Irreducible backgrounds

534 Irreducible backgrounds from $t\bar{t}W$, $t\bar{t}Z$ and $t\bar{t}WW$, are estimated from simulated events. The
 535 2015 BDT outputs are used here as for the signal modelling, and will be updated in later ver-
 536 sions of this note. Just like for the signal, corrections are applied for the different performance
 537 the individual physics objects between data and simulation measured in control regions in
 538 data. The effect of the JEC uncertainties on the final discriminator shapes is shown for $t\bar{t}W$, $t\bar{t}Z$
 539 in Fig. 44 and Fig. 45.

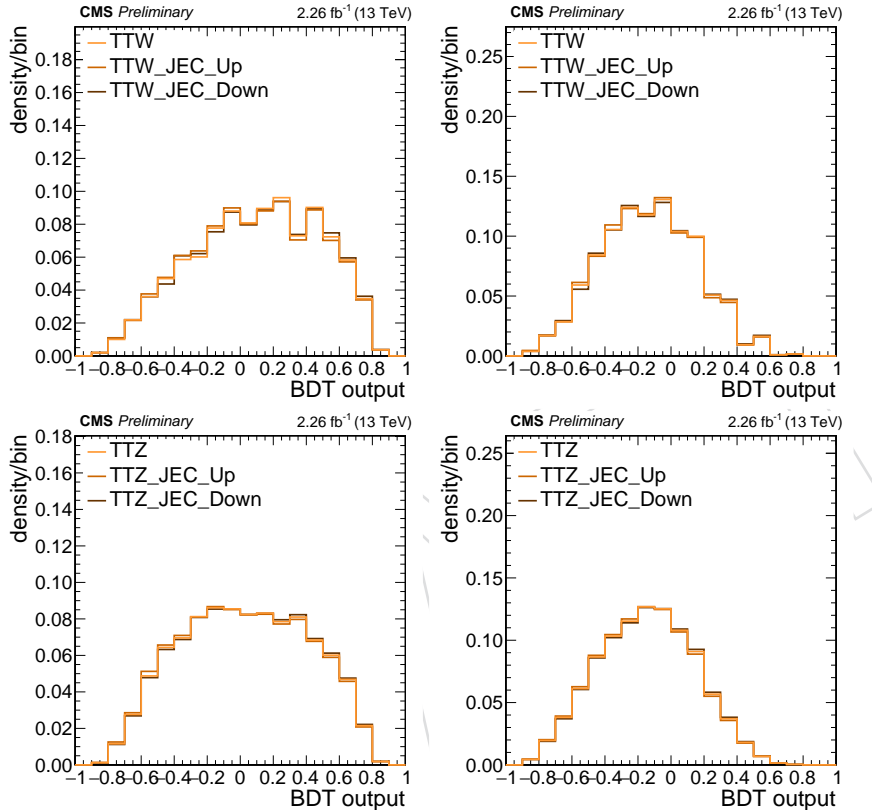


Figure 44: The BDT output distribution of the $t\bar{t}W$ and $t\bar{t}Z$, shown for the training against $t\bar{t}\bar{b}$ (left) and $t\bar{t}V$ (right) in the two same sign leptons final state, with the jet energy scale variations of one standard deviation included in order to estimate the shape uncertainties.

540 In the RunI analysis, the contribution of the $t\bar{t}WW$ process was found to be at least an order of
 541 magnitude smaller than $t\bar{t}W$ and $t\bar{t}Z$. At 13 TeV, NLO (arXiv 1405.0301 table 6), the cross section
 542 is a factor of 5 higher than at 8 TeV (partially because of the k factor as at 8 TeV we only had
 543 LO, and 13 TeV NLO/LO 1.5). Therefore if it was negligible at 8 TeV it still is.

544 The inclusive production cross sections for the $t\bar{t}W$ and $t\bar{t}Z$ processes are taken from the latest
 545 NLO computation, with theoretical uncertainties from unknown higher orders of 12% and 10%
 546 respectively, and uncertainties from the knowledge of the parton density functions and α_s of
 547 2% and 3% respectively [30].

548 In addition to the overall normalisation, systematic uncertainties of theoretical origin on the
 549 distribution of the events in the final discriminating variables are considered, estimated con-
 550 ventionally by varying the normalisation and factorisation scales up and down by a factor of
 551 two and matching threshold between matrix element and parton shower. These results are
 552 shown both for $t\bar{t}W$ and $t\bar{t}Z$ in Fig. 46 and 47. In the current version of the results the shape

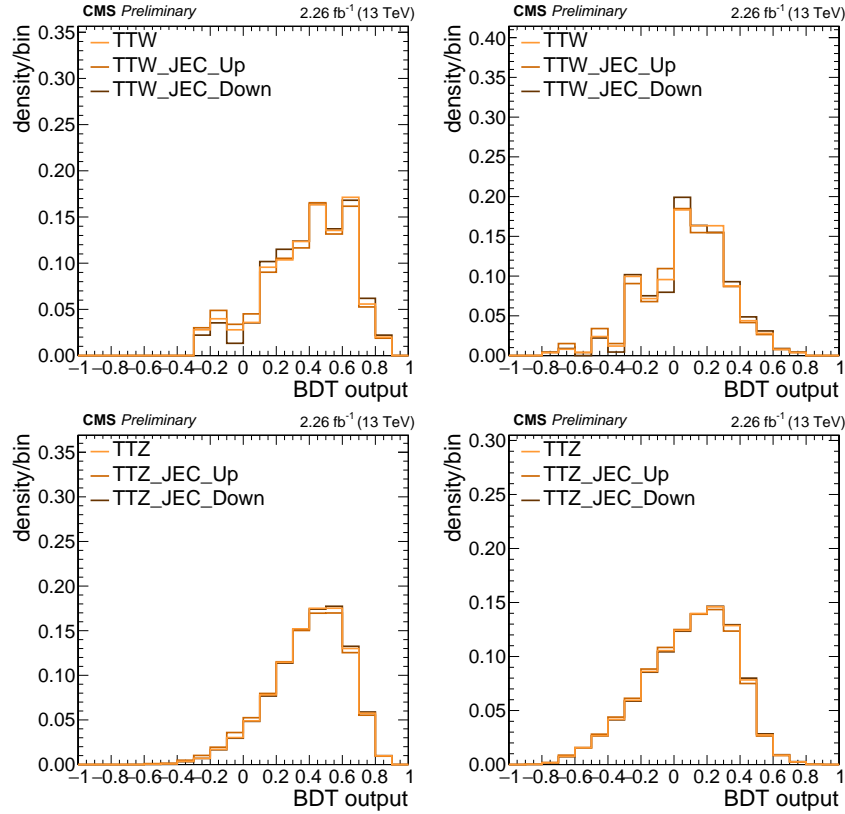


Figure 45: The BDT output distribution of the ttW and ttZ, shown for the training against ttbar (left) and ttV (right) in the three lepton final state, with the jet energy scale variations of one standard deviation included in order to estimate the shape uncertainties.

uncertainties on the BDTs output are of the order of 2% to 4%.

The cross section for the $t\bar{t}\gamma^*$ process with $\gamma^* \rightarrow \ell^+\ell^-$ process becomes large for decreasing virtuality of the γ^* , i.e. for small invariant masses of the dilepton pair. While in the analysis we reject events with low mass dileptons, the $t\bar{t}\gamma^*$ process can still contribute as a background when one of the two leptons is not reconstructed; this in particular can happen in kinematic configurations where the conversion is very asymmetric and one of the two leptons has transverse momentum below the acceptance.

Since the nominal $t\bar{t}Z$ MC sample is generated with the requirement $m_{\ell^+\ell^-} > 10$ GeV, to estimate this background we rely on an additional $t\bar{t}\gamma^*$ MC sample generated in the remaining part of the phase space. This additional sample is generated with LO MADGRAPH, and the details of the generation and normalization can be find here [31].

In the case of electrons, in addition to the $t\bar{t}\gamma^*$ background there is a similar topology of events from $t\bar{t}\gamma$ production where the photon converts early in the detector material, one conversion electron is not reconstructed and the remaining can then be misidentified as prompt electron¹. This background, despite being reducible, is not covered by the reducible background estimation obtained extrapolating from leptons failing the MVA requirement, described later in section 7.4, since the electron arising from the converted photon will be isolated, unlike non-prompt electrons from hadron decays or misidentified charged hadrons. We therefore rely on simulations normalized to NLO QCD cross section from Madgraph5_aMC@NLO.

572

¹If both electrons are reconstructed, then the conversion veto applied in the electron selection will reject both.

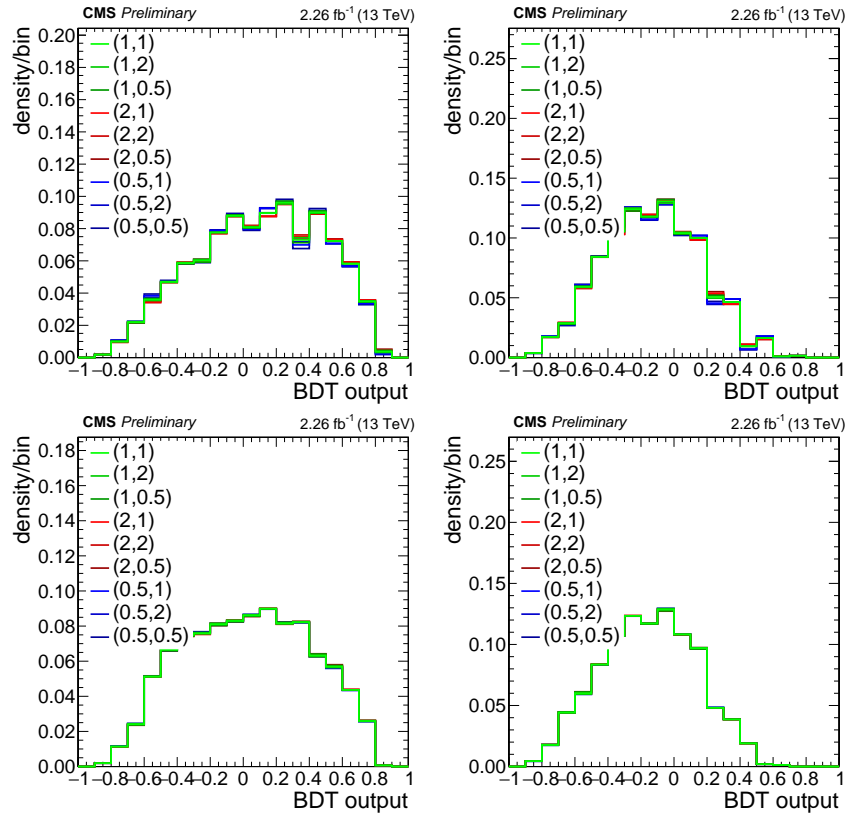


Figure 46: The BDT output distribution of the ttW and ttZ, shown for the training against ttbar (left) and ttV (right) in the two same sign leptons final state, with variations of the renormalization and factorization scale included in order to estimate the shape uncertainties.

573 In addition to the experimental uncertainties, we assign a systematic uncertainty of 30% to the
 574 overall normalization of $t\bar{t}\gamma$ and a systematic uncertainty of 50% on the overall normalization
 575 of $t\bar{t}\gamma^*$.

576 7.2 Di-bosons backgrounds

577 WZ and ZZ production with the gauge boson decaying to electrons, muons or taus can yield
 578 the same leptonic final states as the signal, if considering also events where not all leptons
 579 are identified. While the ZZ background is greatly reduced by the cut on MET LD, the WZ
 580 background remains an important contribution to the three and more leptons signal region.

581 When not requiring additional hadronic jets in the final states, these processes are predicted
 582 theoretically at NLO accuracy, and the inclusive cross sections have been successfully mea-
 583 sured at the LHC. However these good agreement does not translate automatically to the signal
 584 regions used in this search, which always require the presence of at least one b-tagged jet.

585 Since dibosons are preferentially produced in association with jets from light quarks or glu-
 586 ons, it is possible to isolate a clean control region of WZ plus hadronic jets by inverting the
 587 b-tagging requirements of the signal region and also inverting the $Z \rightarrow ll$ veto. The approach
 588 chosen for estimating the background is therefore to use simulated events but normalizing the
 589 overall event yields in control regions of WZ plus two not b-tagged jets. This reduces the sys-
 590 tematic uncertainty on the prediction, since the theoretical uncertainty on the ratio of event
 591 yields between signal region and control region is much smaller than the uncertainty on the
 592 production cross section of diboson plus multijet. The majority of events from this background

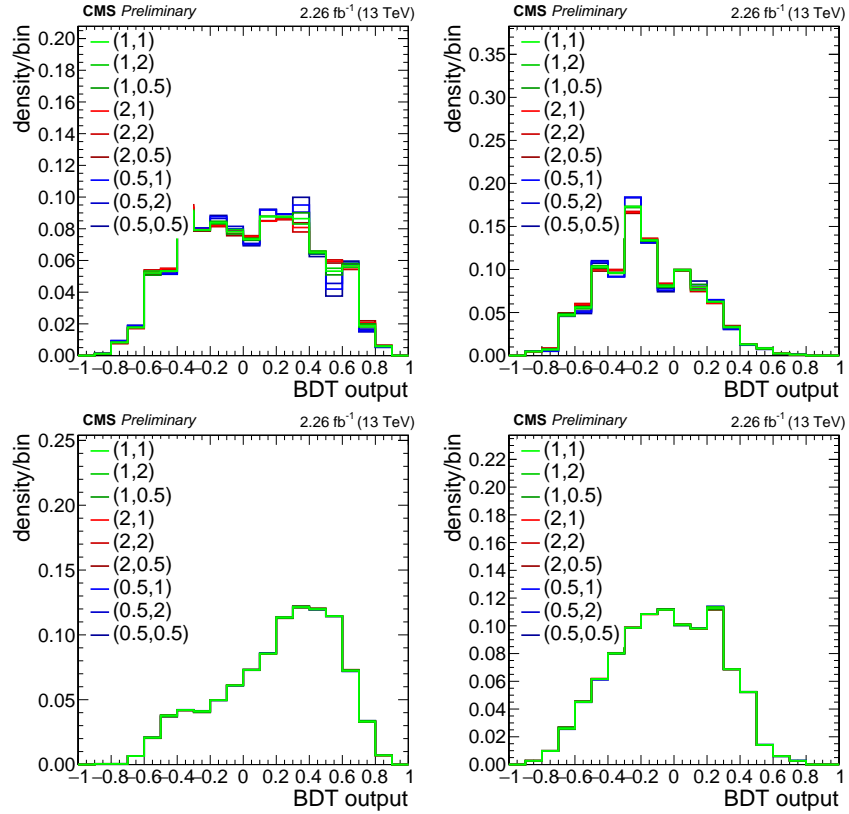


Figure 47: The BDT output distribution of the ttW and ttZ, shown for the training against ttbar (left) and ttV (right) in the three lepton final state, with the variations of the renormalization and factorization scale included in order to estimate the shape uncertainties.

593 in the signal region contain jets from gluons or light quarks mistagged as b-jets, for which the
594 extrapolation is affected only by uncertainties of experimental origin.

595 7.2.1 Measurement in data from events with no b-jets

596 The extraction of the WZ yield in the control region is performed via a one dimensional neg-
597 ative log likelihood fit of the shape of transverse mass of the lepton not associated to the Z
598 boson. The shape and normalization of the residual backgrounds are fixed to the expectations
599 from simulations. The measurement has been performed on 6.3 fb^{-1} data collected in 2016,
600 and yields a scale factor of 1.2 ± 0.1 (stat.) (*this scaling is not yet propagated to the signal extrac-*
601 *tion, it will be updated for the approval and we expect a negligible impact on the final result*). Figures
602 48, 49, and 50 show the good agreement observed in the WZ control region for the following
603 distributions:

- 604 • $m_T W(l)$
- 605 • E_T^{miss}
- 606 • selected jet multiplicity
- 607 • sum of lepton charges
- 608 • reconstructed Z invariant mass

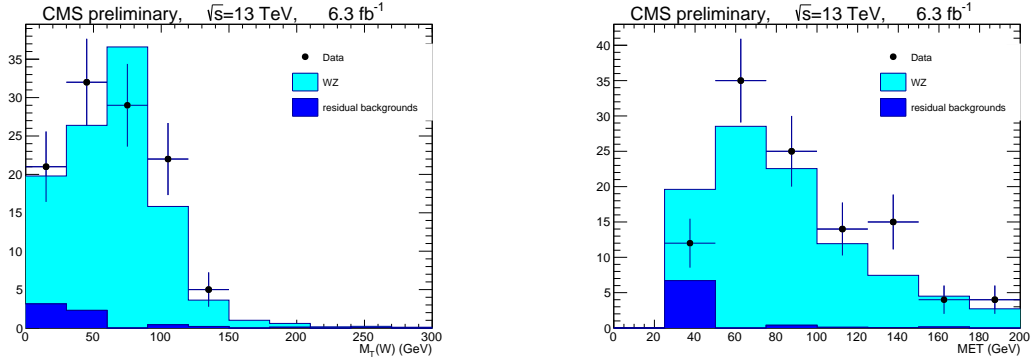


Figure 48: Distribution of the transverse mass of the lepton not associated to the reconstructed Z boson, $m_T(l)$, (left) and transverse missing energy, met , (right) after a fit of the WZ and background processes to the data.

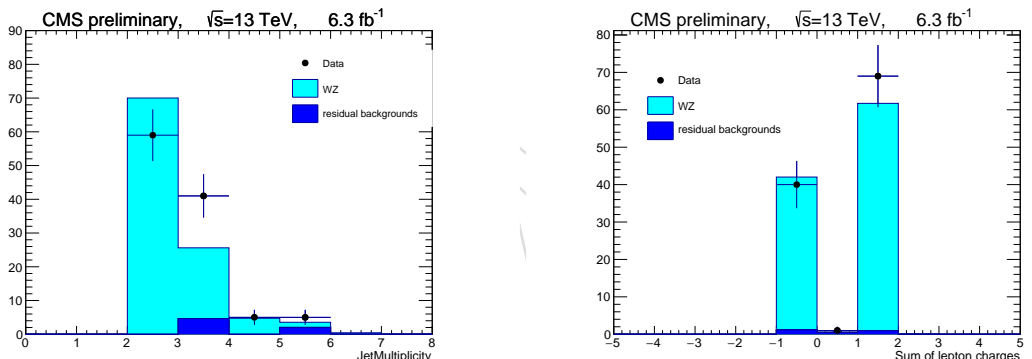


Figure 49: Distribution of the jet multiplicity (left) and sum of the leptons charges (right) after a fit of the WZ and background processes to the data

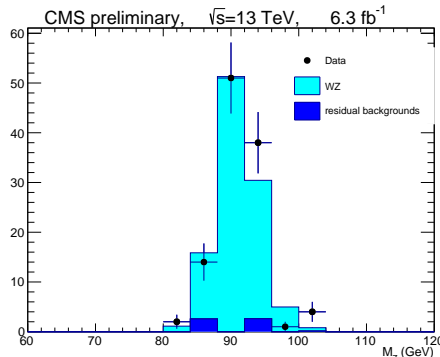


Figure 50: Distribution of the Z candidate invariant mass.

609 7.2.2 Extrapolation to events with b-jets

610 The ratio of the events yields between signal region and control region is measured in the
 611 simulation. The main systematics are expected to come from the b-tagging scale factors since
 612 most of the WZ plus two b-jets events are due to mistags:

$$\text{SR-b-loose/CR} : 0.0371 \pm 0.0041 \text{ (b-tagging)} \pm 0.0028 \text{ (theory)}$$

$$\text{SR-b-tight/CR} : 0.0015 \pm 0.0006 \text{ (b-tagging)} \pm 0.0001 \text{ (theory)}$$

613 Theoretical uncertainties arise from the modelling of the heavy flavour content of the jets in
 614 diboson plus multijet events. The expected flavour composition for WZ events passing the
 615 b-loose (resp. b-tight) jet selection is approximately 35% (13%) of events with mistagged jets
 616 from gluons or u,d,s quarks, 47% (50%) of events with a jet from a charm quark or antiquark, and
 617 the remaining fraction from events with at least one bottom quark or antiquark. Uncertainties
 618 on the extrapolation arising from the parton distribution functions are estimated by simulated
 619 reweighting of the events to different PDG sets and all their associated eigenvectors or replicas.

620 The overall uncertainty on the normalization of the WZ background is composed by the sta-
 621 tistical uncertainty in the control region, from the residual backgrounds in the control region,
 622 from the uncertainties on the b-tagging efficiencies, from the parton distribution functions and
 623 from the theoretical uncertainties on the extrapolation (dominated by the uncertainty on the
 624 flavor composition of the final state due to higher-order QCD terms).

625 7.3 Charge misassignment background

626 The background from processes with prompt opposite-sign lepton pairs like $t\bar{t}$ or DY+jets,
 627 where one of the two leptons has a wrongly assigned charge, is estimated from the measured
 628 charge misassignment probabilities and the events of a corresponding opposite-sign control re-
 629 gion. Naturally, this background is only relevant for the same-sign dilepton channels. Studies
 630 in MC show the charge misassignment probability for muons to be negligible, and we subse-
 631 quently restrict ourselves to electrons.

632 7.3.1 Measurement of the electron charge misassignment probabilities

633 The charge misassignment probability for electrons can be extracted from the data, in events
 634 with two same-sign electrons with invariant mass close to the mass of the Z boson. Electron
 635 pairs in the peak are sure to be from real opposite sign pairs with a wrongly assigned charge
 636 on one leg.

637 Charge misassignment probabilities are calculated for different bins of electron p_T and η by
 638 extracting same-sign and opposite-sign event yields categorized in the kinematics of the two
 639 lepton legs. In each category, the event yield of electron pairs from Z decays is determined
 640 from a fit to the invariant mass shape, and depends on the charge misassignment probabilities
 641 of each leg. The invariant mass shape is modeled with a crystal ball and Breit-Wigner function
 642 for the signal and an exponentially falling function for the backgrounds.

643 Electron kinematics are separated in three p_T (10–25 GeV, 25–50 GeV, and ≥ 50 GeV) and two
 644 η bins (0–1.479 and 1.479–2.5), resulting in a total of 21 distinct categories of electron pairs.
 645 The six charge misassignment probabilities are then determined in a simultaneous fit to the 21
 646 same-sign and opposite-sign event yields.

647 The resulting misassignment probabilities range between about 0.03% in the barrel and about
 648 0.4% in the end caps and are shown in Tab. 10 and Fig. 51.

Table 10: Electron charge misassignment probabilities (in percent) as determined in data (top) and Drell–Yan MC (bottom).

Data	$10 \leq p_T < 25 \text{ GeV}$	$25 \leq p_T < 50 \text{ GeV}$	$50 \text{ GeV} \leq p_T$
$0 \leq \eta < 1.479$	0.0337 ± 0.0133	0.0259 ± 0.0017	0.0403 ± 0.0049
$1.479 \leq \eta < 2.5$	0.1476 ± 0.0249	0.2599 ± 0.0079	0.3963 ± 0.0234
MC			
$0 \leq \eta < 1.479$	0.0608 ± 0.0042	0.0296 ± 0.0015	0.0177 ± 0.0040
$1.479 \leq \eta < 2.5$	0.1047 ± 0.0160	0.2376 ± 0.0074	0.3101 ± 0.0105

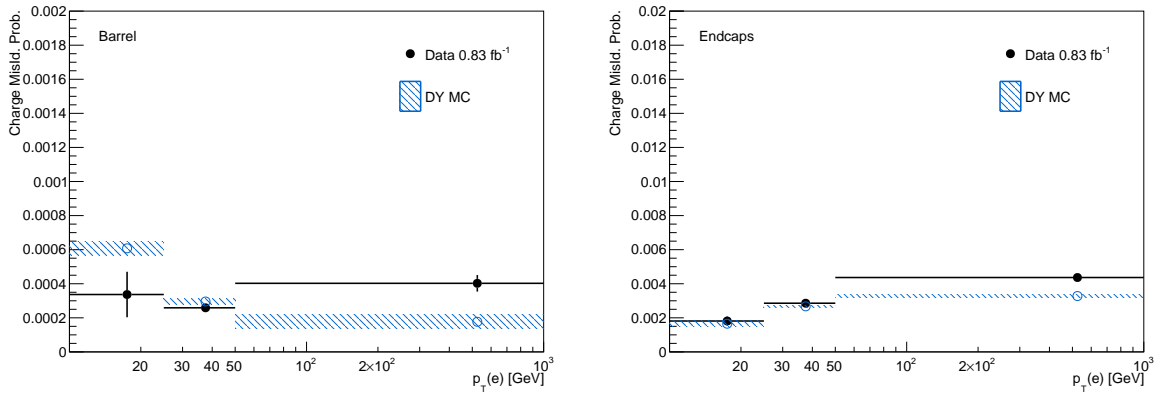


Figure 51: Electron charge misassignment probabilities as a function of p_T for electrons in the barrel (top) and endcaps (bottom).

649 7.3.2 Background estimation

650 Contributions from opposite-sign prompt leptons with charge-misassigned electrons to the
 651 same-sign dilepton channels with electrons (ee, and e μ) are then estimated from the events
 652 of a control region with identical selection except for the requirement of equal charge of the
 653 lepton pair. Each event in the control region is assigned a weight of $P(p_T, \eta)$ for each electron
 654 with a given p_T and η in the event (i.e. ee events get a weight of $P_1 + P_2$ and e μ events get a
 655 weight of P), where P is the measured charge misassignment probability.

656 The procedure is tested in two control regions: once using the same events that were used
 657 to measure the probabilities, dominated by DY events, and once in a selection with at least
 658 one medium b-tagged jet or two loose b-tagged jet and between 2 and 3 hadronic jets, with a
 659 significant contribution from t \bar{t} events. Event distributions in the two control regions where the
 660 background from charge misassigned electrons is estimated as described are shown in Fig. 52
 661 and 53.

662 From the statistical uncertainty of the measured probabilities and the good agreement of pre-
 663 dicted charge-flip yields with the observed data distributions in the control regions, we assign
 664 a generous 30% uncertainty on the predicted event yields from this background.

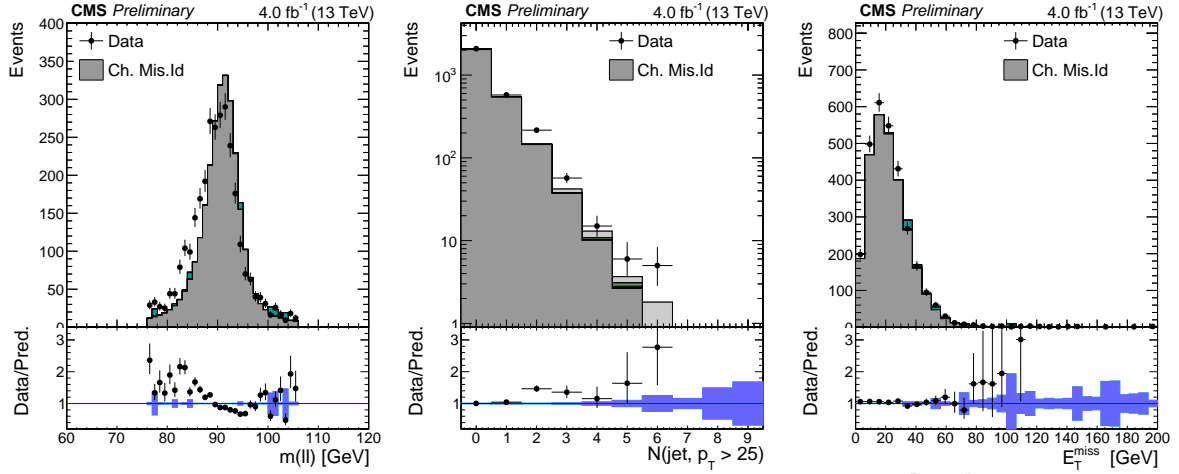


Figure 52: Charge misassignment closure test in DY dominated control region (where the misassignment probabilities are extracted from).

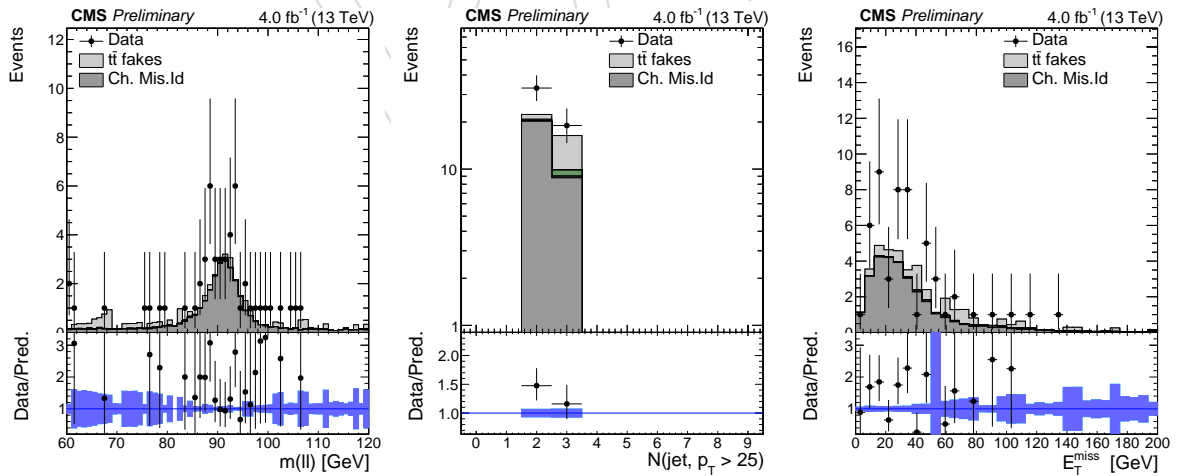


Figure 53: Charge misassignment closure test in a selection of exactly two same-sign electrons passing the full selection, between 2 and 3 hadronic jets, and at least one medium b-tagged jet or two loose b-tagged jets.

665 **7.4 Fake lepton background**

666 **7.4.1 Fakeable object definition tuning**

667 The main control region we use to measure the fake rate is enriched in QCD jet events, and
 668 is obtained selecting events with one loose lepton and an hadronic jet well separated from the
 669 lepton ($\Delta R > 0.7$).

670 For all muons and electrons with p_T above 30 GeV, events are selected at trigger level requiring
 671 a prescaled single lepton trigger (with no isolation requirements) and a particle flow jet with p_T
 672 30 GeV reconstructed at HLT (40 GeV for low- p_T muons). This implies that the fakeable objects
 673 in the measurement region all pass the lepton trigger, while in the application region this is not
 674 necessarily the case, as we include also events triggered by a single or double lepton trigger.
 675 In order to avoid a bias in the background estimate, we therefore need to have a definition of
 676 fakeable object so that the fake rate does not depend on whether the lepton passes the trigger
 677 selection or not.

678 We assess this using non-prompt leptons in simulated lepton-enriched QCD events, where we
 679 can compare the fake rate with and without requiring the lepton to pass the trigger, for different
 680 choices of the fakeable object selection. The study reveals two important features: first, the
 681 trigger turn-on imposes a cut on the reconstructed lepton p_T , and so it limits the amount of
 682 sideband available in the extrapolation for given bin in corrected lepton p_T . Because of this, a
 683 trigger with a given threshold, can only be used to measure the fake rate for significantly larger
 684 corrected p_T value, if we do not want the trigger threshold to bias the result. For example, for
 685 events collected by the HLT_Mu8 trigger, the fake rate is not biased only for corrected p_T above
 20 GeV (Fig. 54, left).

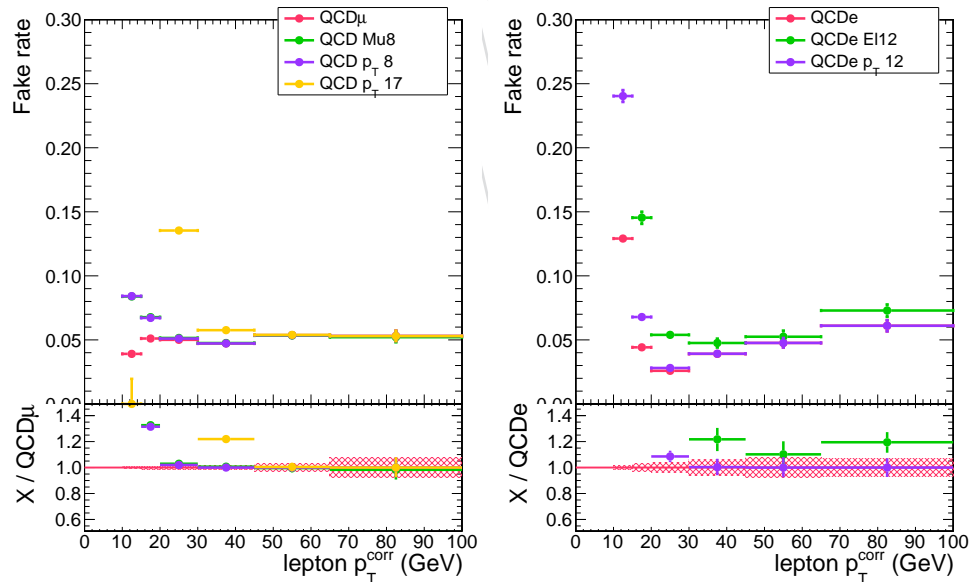


Figure 54: Left: fake rate for muons in the barrel, from simulated QCD events: with only the loose lepton selection requirement (pink), or after the HLT_Mu8 trigger (green), or after a requirement of $p_T > 8$ GeV at reconstruction level (violet, on top of the green). The $p_T > 8$ GeV requirement and the trigger selection do not bias the fake rate measurement above 20 GeV. Right: fake rate for electrons after trigger emulation cuts in the barrel, from simulated QCD events: with only the loose lepton selection requirement (pink), after a requirement of $p_T > 12$ GeV at reconstruction level (violet, on top of the pink above 30 GeV), and after the HLT_Ele12_CaloIdM_TrackIdM_PFJet30 trigger (green).

Because of these effects, we measure the fake rate for muons using a combination of the HLT_Mu3_PFJet40 trigger (for corrected $p_T \in [10, 20]$ GeV), the HLT_Mu8 trigger (for corrected $p_T \in [20, 45]$ GeV) and the HLT_Mu17 trigger (for corrected p_T above 45 GeV), and the fake rate for electrons using the HLT_Ele12_CaloIdM_TrackIdM_PFJet30 trigger (for $p_T > 30$ GeV).

Beyond the impact of the p_T threshold, the trigger can also bias the fake rate if it has requirements in identification or isolation that are not strictly looser than the selection used at the denominator. For muons, as long as we use triggers with no isolation requirements this is not the case. In the case of electrons, the identification criteria applied at HLT, cut-based, are different from those offline (mva-based), and so we would have a mismatch even for electrons well above the p_T threshold of the trigger.

We solve this, for electrons with corrected $p_T > 30$ GeV, by tightening the fakeable object definition including in it also some cut-based electron identification criteria. The selection criteria to emulate the trigger are chosen by comparing electron identification variables for non-prompt electrons in QCD MC events for electrons that pass or fail the trigger. The cuts have to be tight enough that for events passing them the fake rate does not depend strongly on whether the event passes or fails the trigger (Fig. 54, right). However, cuts need to be not too tight less they start causing a loss of signal efficiency, because they use the identification variables in a less optimal way than the mva electron identification. For the criteria we use in this analysis, the loss of efficiency introduced by these cuts for signal MC events that pass the full analysis selection and trigger is about 2% in both the dielectron and electron-muon final states.

The choice of the lepton identification criteria on the fakeable object determine, together with the working point used for the tight lepton definition, the the fake rate for fake leptons, while they do not affect substantially the fake rate for non-prompt leptons originating from the decay of heavy flavour hadrons. On the other hand, the cut on the b-tagging discriminator of the jet associated to the lepton in the fakeable object definition can alter the fake rate for non-prompt leptons from heavy flavour without affecting fake leptons which are mostly originating from light jets. Thus, we can tune this cut to make the two fake rates more similar, and thus reduce the uncertainties associated to the flavour dependency of the fake rate. The quality of the tuning can be evaluated comparing e.g. the fake rates in $t\bar{t}$ events in the application region for the b-loose and b-tight category, that have different flavour compositions (Fig. 55).

7.4.2 QCD measurement region definition cuts

For a fixed choice of the fakeable object and numerator, we can then assess how the fake in QCD events agrees with that of $t\bar{t}$, and how it depends on the cuts on the tag jet used to select the events. A comparison of fake rates for background leptons in $t\bar{t}$ and QCD is shown in Fig. 56, both inclusively and selecting only leptons from b-jets. Good agreement between the two MC samples is observed for electrons with $p_T > 30$ GeV and for muons of any p_T .

A comparison of fake rates for QCD events as function of the requirements on the recoiling jet in the QCD selection is illustrated in Fig. 57. For both leptons, we observe an excellent stability of the fake rate as function of the recoiling jet p_T , and only a moderate dependency on the b-tagging requirements of the away jet. So, we decide to define the measurement region requiring only $p_T > 30$ GeV on the recoling jet, and no b-tagging, to benefit from the largest event sample and reduce the statistical uncertainties in the measurements.

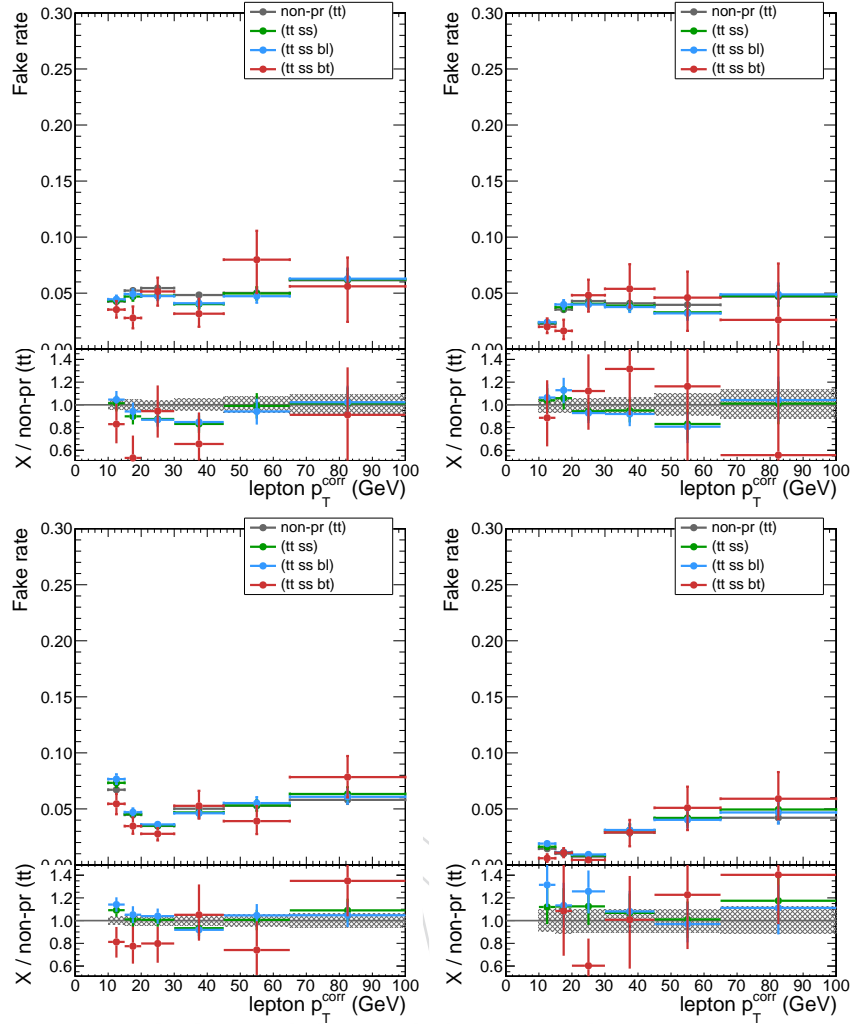


Figure 55: Fake rate for muons (top) and electrons (bottom) in the barrel (left) and endcaps (right), from simulated $t\bar{t}$ events, inclusively (gray), in same-sign events (green), in same-sign events in the b-loose category (blue), and in same sign-events in the b-tight category (red).

728 7.4.3 QCD measurement: prompt lepton contamination

729 An important challenge in measuring the fake rate in jet events in data is the contamination of
 730 prompt leptons, mostly from W and Z production in association with hadronic jets. In order
 731 to suppress the Z contamination, events with more than one loose lepton are vetoed, leaving
 732 mostly events with one leptons outside the acceptance or from $Z \rightarrow \tau_\ell \tau_h$. A good discrimi-
 733 nation between QCD events and W can be achieved from the transverse mass of the lepton
 734 and missing energy in the event, $M_T(\ell, E_T^{\text{miss}})$. The standard procedure is to apply a tight cut
 735 $M_T(\ell, E_T^{\text{miss}}) < 15 \text{ GeV}$ was applied, and the residual contamination was subtracted at numer-
 736 ator and denominator in each p_T bin using simulated W/Z + jets events. The simulation was
 737 normalized to the data from a fit to $M_T(\ell, E_T^{\text{miss}})$, in the sample of events at the fake rate nu-
 738 merator (i.e. passing the tight requirements), before the cut at 15 GeV.

For this analysis, we implemented two improvements on that procedure. The first improvement is a change in the discriminating variable used: the traditional transverse mass

$$M_T(\ell, E_T^{\text{miss}}) = \sqrt{2p_{T\ell}E_T^{\text{miss}}(1 - \cos \Delta\phi)}$$

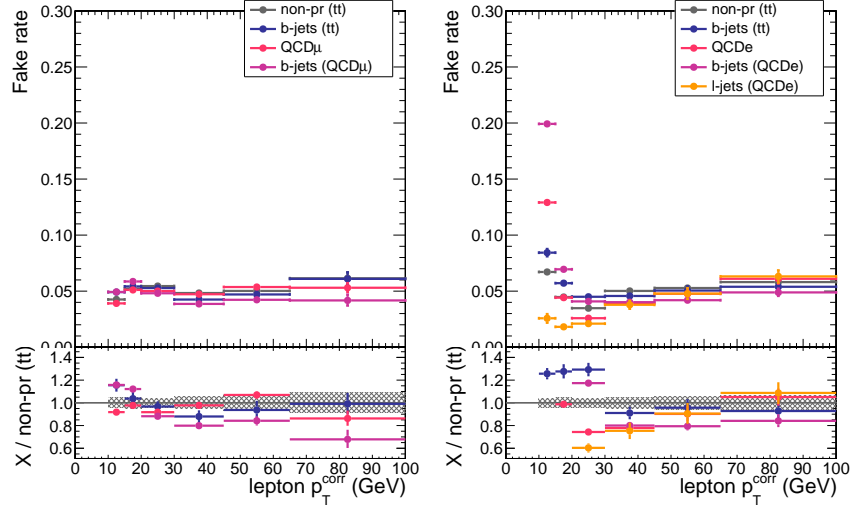


Figure 56: Fake rate for background leptons in the barrel, from simulated $t\bar{t}$ and QCD events, inclusively or selecting only those from B hadron decays. The left plot is for muons, the right one for electrons.

is obviously correlated with the lepton p_T , and so also with the lepton fake rate. To avoid this correlation, which can potentially introduce biases in the subtraction procedure, we define a new variable

$$M_T^{\text{fix}}(\ell, E_T^{\text{miss}}) := \sqrt{2p_T^{\text{fix}}E_T^{\text{miss}}(1 - \cos \Delta\phi)}$$

replacing the lepton p_T with a fixed number (35 GeV), and thus relying only on the lepton direction. This variable still has a good discriminating power against $W + \text{jets}$ but is much less correlated with the lepton p_T and so with the fake rate.

The second improvement is the introduction of two alternative ways to implement the subtraction of the prompt contamination. The first alternative procedure is the one used in the run 1 analysis, and documented in detail in Section 7.4.2 of AN-13-159, except that we update it to use $M_T^{\text{fix}}(\ell, E_T^{\text{miss}})$ instead of E_T^{miss} . The procedure relies on two measurement of the fake rate in data, one for small M_T^{fix} values and one for large and large M_T^{fix} values. Assuming the fake rate to be independent from M_T^{fix} , and taking from the simulation the ratio of $V + \text{jets}$ events expected in the two regions, it is possible to unfold the fake rate for QCD events from the two measurements:

$$f_{\text{QCD}} = \frac{f_S - r_{V+j}^{\text{SL}} f_L}{1 - r_{V+j}^{\text{SL}}} \quad \text{where} \quad r_{V+j}^{\text{SL}} = \left(\frac{N_{V+j}^S}{N_{V+j}^L} \right) / \left(\frac{N_{\text{data}}^S}{N_{\text{data}}^L} \right),$$

where f_i are the fake rates measured in data for small (S) and large (L) values of M_T^{fix} , N_{V+j}^i are the expected event yields from $V + \text{jets}$ and N_{data}^i are the observed events in data in the two regions at the denominator of the fake rate. This procedure can be performed separately in each bin of p_T , $|\eta|$. In addition to the statistical uncertainties on the fake rate measurement in the two regions and on r_{V+j}^{SL} , we also add a systematical uncertainty on r_{V+j}^{SL} from the difference in evaluating N_{V+j}^S / N_{V+j}^L at the denominator and numerator of the fake rate.

A second alternative procedure relies on a simultaneous fit of the M_T^{fix} distribution for passing and failing probes, in a very similar way to the method used in the tag and probe method at the Z peak by fitting the invariant mass of the dilepton pair to extract efficiencies for the signal even in the presence of background. In our case, fit is done using templates from simulation

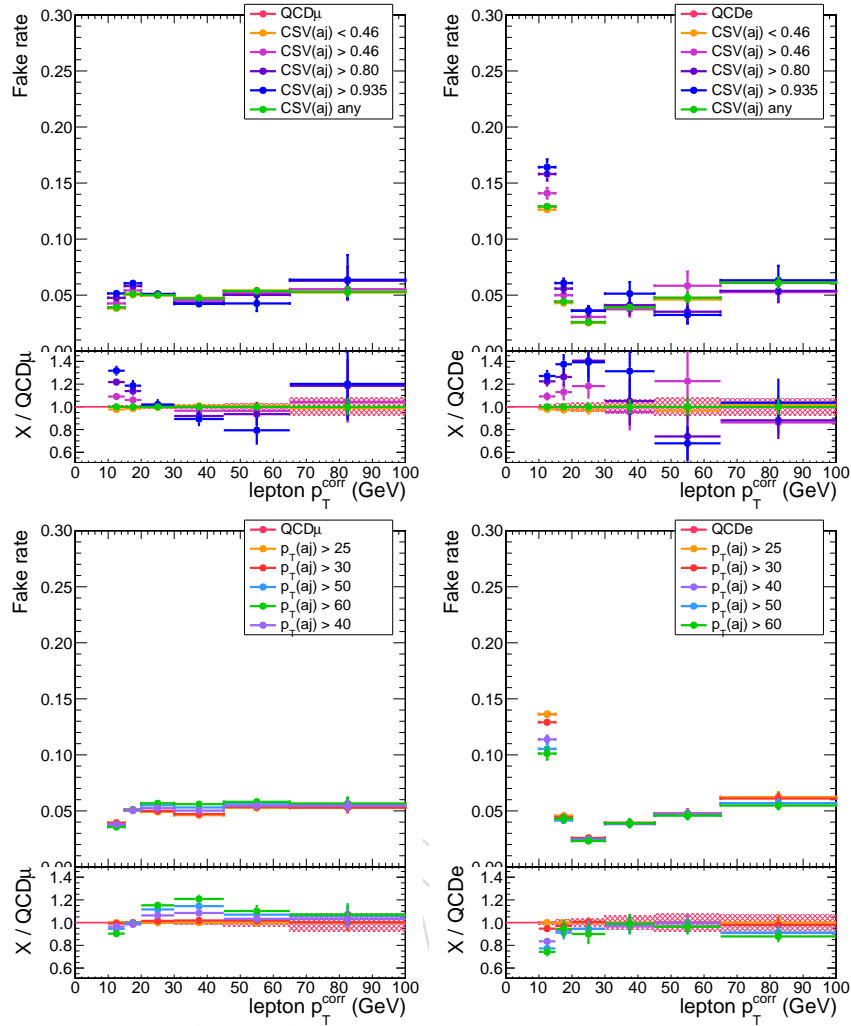


Figure 57: Fake rate for leptons in the barrel in simulated QCD and $t\bar{t}$ events, as varying the requirement on the recoiling jet. In the top row, different cuts are applied on the b-tagging discriminator of the jet, while in the bottom row different p_T thresholds are applied. Fake rates in the left column are for muons, those in the right column for electrons.

for the QCD and V + jets contributions. In addition to bin-by-bin statistical uncertainties on the templates, we include systematic shape uncertainties on the templates: we allow both a linear deformation of the template and a stretching of the template, as illustrated in Fig. 58. The shape systematics are assumed to be uncorrelated between QCD and V + jets, but totally correlated between passing and failing probes; the size of the deformation has been chosen to approximately cover the data to simulation differences observed across the various bins. The final uncertainty on the fake rate is obtained by profiling the likelihood of the simultaneous fit, and thus includes both the statistical and the systematical uncertainties.

Results of the measurement with all three subtraction methods are shown in Fig. 59. For the cut and subtraction method, the error bars include a systematical uncertainty of 10% on the subtraction, which dominates over the statistical uncertainties at larger p_T . Within uncertainties, the three methods agree among themselves and also with the fake rate in MC. Since we do expect at least some correlation in the uncertainties of the three measurements, we opt for a conservative combination of the three by taking as central value the weighted average and as uncertainty band the envelope of the three uncertainty bands.

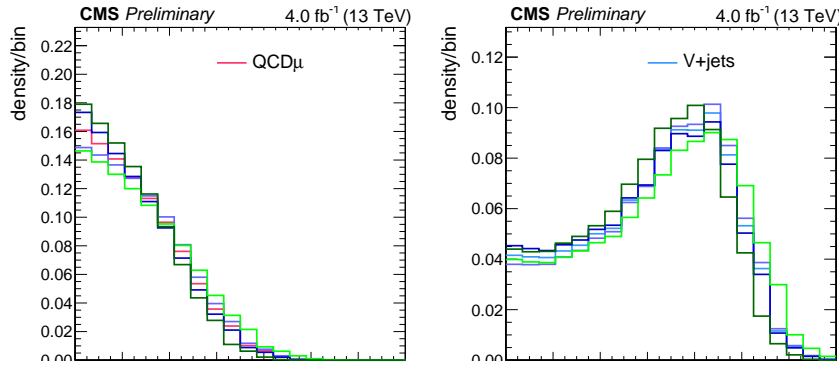


Figure 58: Shape uncertainties on the M_T^{fix} templates for muons in the barrel, in the bin of corrected p_T 20–30 GeV, for QCD events (left) and V + jets events (right)

7.4.4 Low p_T electrons

The fake rate for electrons with $p_T < 30$ GeV is derived using $Z + \ell$ events, where the leptons from the Z boson can be used to trigger the event without biasing the third lepton. This is justified by simulations, where the fake rate for non-prompt electrons $Z + \ell$ is found to be in good agreement with the one for non-prompt electrons in $t\bar{t}$ events (Fig. 60, left). Similarly to the measurement from QCD dijet events, a challenge is posed by the contamination from prompt leptons, in this case from WZ and ZZ production. As this control region differs from the QCD one only by the replacement of the tag jet with a Z boson, it is similarly possible to discriminate between the non-prompt and prompt leptons contributions on the basis of M_T^{fix} , and use the same subtraction methods (Fig. 60, right).

7.4.5 Results

The final fake rates for electrons and muons are shown in Fig. 61. Overall, a good agreement between data and predictions from simulations is observed. Uncertainties are larger for very low p_T , driven by statistical uncertainties, and at very high p_T , driven by the uncertainties on the subtraction of the prompt lepton contamination.

7.4.6 Fake rate application

The application of the fake rates follows the same principles already used for the analysis that was performed on the 8 TeV dataset.

In summary, a control region enriched in events with fake leptons, denoted as *application region* in the following, is selected by requiring that at least one of the selected leptons fails the tight lepton requirements.

The extrapolation from this control region to the signal region is performed by expressing the yields of events where k leptons pass the full selection and $n - k$ fail it in terms of the yields of events with n leptons among prompt and non-prompt ones, efficiencies and fake rates, for $n = 2$ or 3 and all possible values of k .

792

793 In two lepton events ($n = 2$), the background contribution in the signal region can be expressed

794 as:

$$N_{pp}^{\text{bkg}} = \frac{f_1}{1-f_1} N_{pf} + \frac{f_2}{1-f_2} N_{pf} - \frac{f_1 f_2}{(1-f_1)(1-f_2)} N_{ff}$$

795 under the approximation that the contribution of prompt leptons failing the selection can be
 796 neglected with respect to the contributions of non-prompt leptons. It is worth noting that the
 797 event yield observed in the signal region does not affect the background prediction.

798

799 Following the same logic, the background prediction in the three lepton category is obtained
 800 by weighting the events in the application region according to the following prescription:

- 801 • events with only one failing lepton are weighted by $f/(1-f)$, where f is the fake
 802 rate evaluated on the kinematic quantities of the failing lepton;
- 803 • events with two failing leptons (i, j) are weighted by $-f_i f_j / ((1-f_i)(1-f_j))$;
- 804 • events with all three failing leptons are weighted by $f_1 f_2 f_3 / ((1-f_1)(1-f_2)(1-f_3))$.

805 A proof of the results presented above can be found in [32].

806 7.4.7 Closure tests on simulated events

807 Closure tests are performed on simulated events in order to confirm that the methods described
 808 in the present Section are well suited to predict the reducible background after the event selec-
 809 tion requirements.

810 A fake rate extracted from non-prompt leptons in QCD MC, selected inclusively, is first applied
 811 to 2lss semi-leptonic $t\bar{t}$ simulated events where at least one of the two selected candidates fails
 812 the tight lepton requirements. Moreover, an alternative fake rate from non-prompt leptons in
 813 $t\bar{t}$ MC, selected inclusively as well, is applied to the same 2lss sample.

814 The test described above is performed in different event selections (separately for lepton fla-
 815 vors and analysis category). The difference in normalization between the two predictions, as
 816 well as their difference in the shape of the two kinematic discriminators against the $t\bar{t}$ and $t\bar{t}V$
 817 backgrounds, are propagated as a systematic uncertainty to the fit used to extract the signal.
 818 An example of the distributions can be found in Fig. 62.

819 Moreover, the uncertainty in the fake rate measurement is propagated to the final fit studying
 820 both the difference in background normalization from a coherent shift in the fake rate map, and
 821 the effect on the shape of the kinematic discriminators arising from possible trends in the fake
 822 rate map as a function of the lepton p_T and $|\eta|$ within the fake rate map uncertainty (Fig. 63).

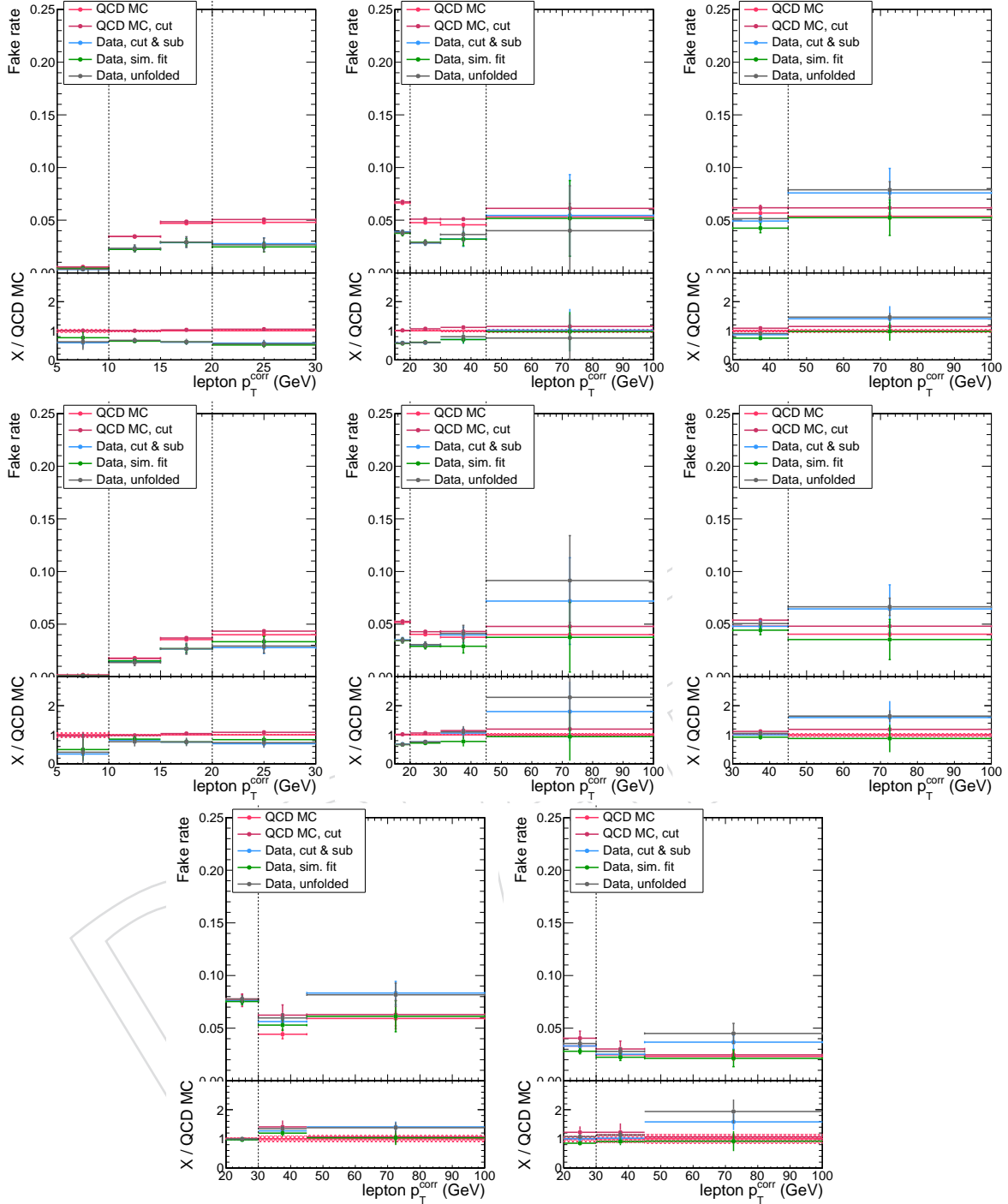


Figure 59: Fake rate measurement in data, for different subtraction methods, and compared with the predictions from simulation for non-prompt leptons from QCD MC. The first two rows are for barrel and endcap muons respectively. From left to right, muons passing the HLT_Mu3_PFJet40 trigger, the HLT_Mu8 trigger, the HLT_Mu17 trigger. The bottom row is for barrel and endcap electrons passing the HLT_Ele12_CaloIdM_TrackIdM_PFJet30 trigger. For illustration, the plots for each trigger include also p_T bins whose measurement is not used in the analysis. For this plot alone, the cut-based electron id requirements are included in the loose lepton definition also below 30 GeV, so that the fake rate is continuous.

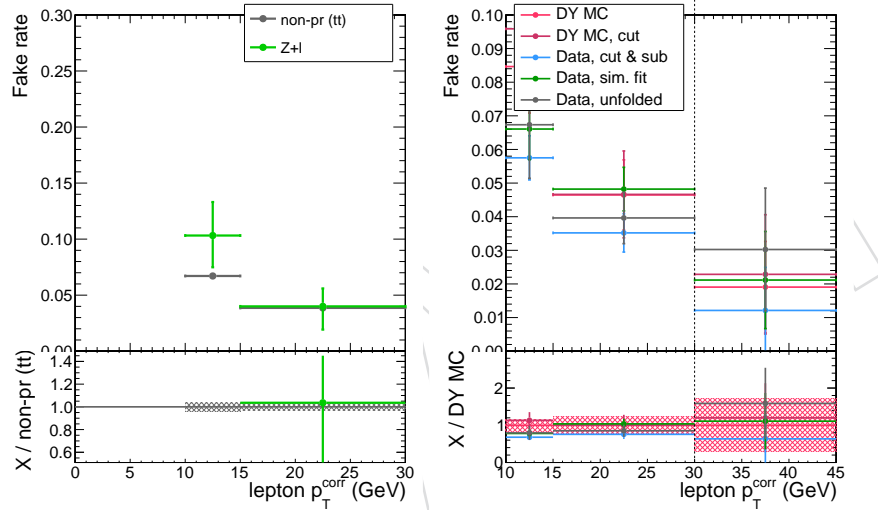


Figure 60: Left: comparison of fake rates for electrons in the barrel between simulated $Z + \ell$ and $t\bar{t}$ events. Right: measurements of the fake rate in data for electrons in the barrel, with different subtractions for the prompt contamination.

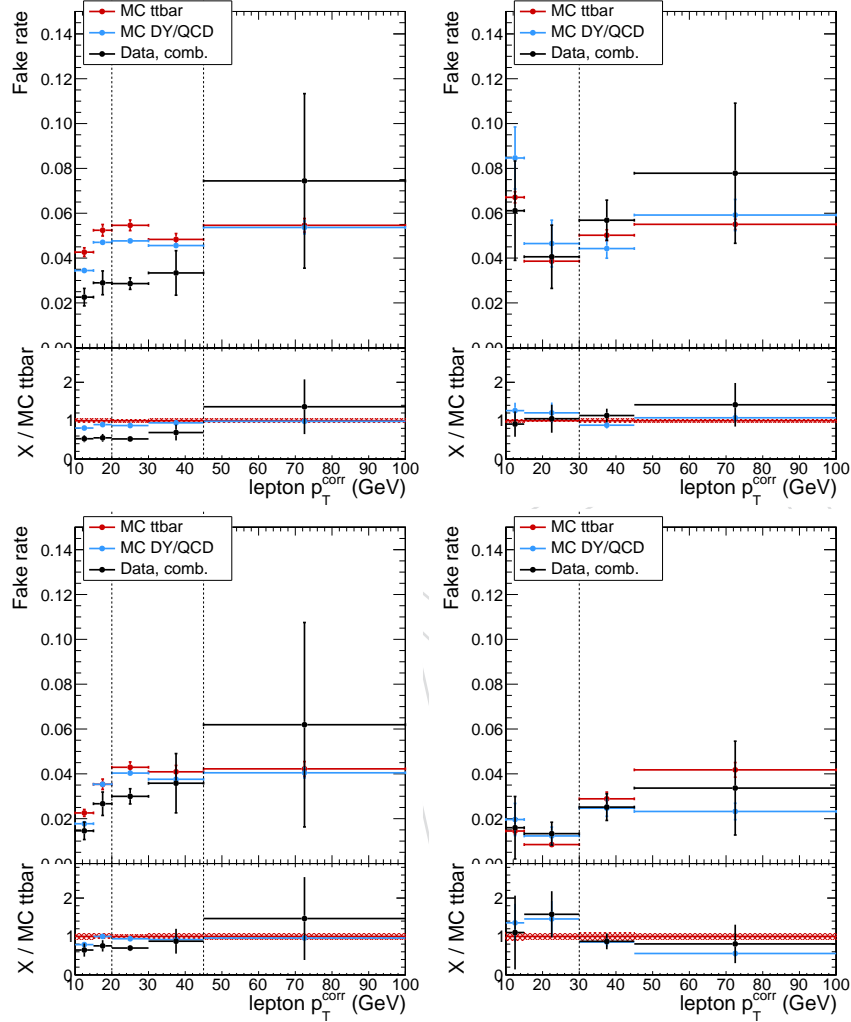


Figure 61: Summary of the fake rate measurement in events in data, compared with the predictions from simulated events in the measurement region (blue) and from non-prompt leptons in $t\bar{t}$ (red). Plots in the left column are for muons, those in the right column for electrons; the top row is for the barrel, the bottom for the endcaps. Measurements and expectations are derived from QCD events using different triggers, except for the electrons below 30 GeV for electrons which are derived from $Z + \ell$ events. The data values and uncertainties are the weighted average and envelope of the different prompt contamination subtraction algorithms.

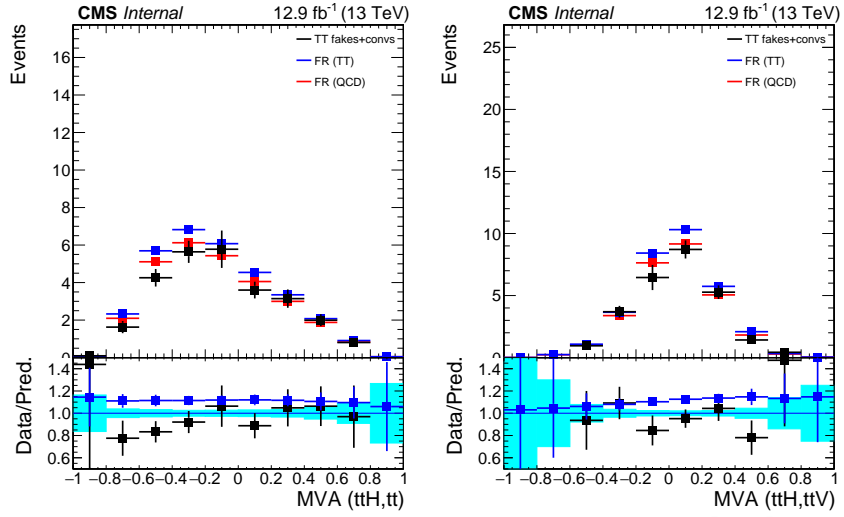


Figure 62: Shape of kinematic discriminators for semi-leptonic $t\bar{t}$ events, and for background predictions obtained in simulation using fake rates extracted in QCD and $t\bar{t}$ events.

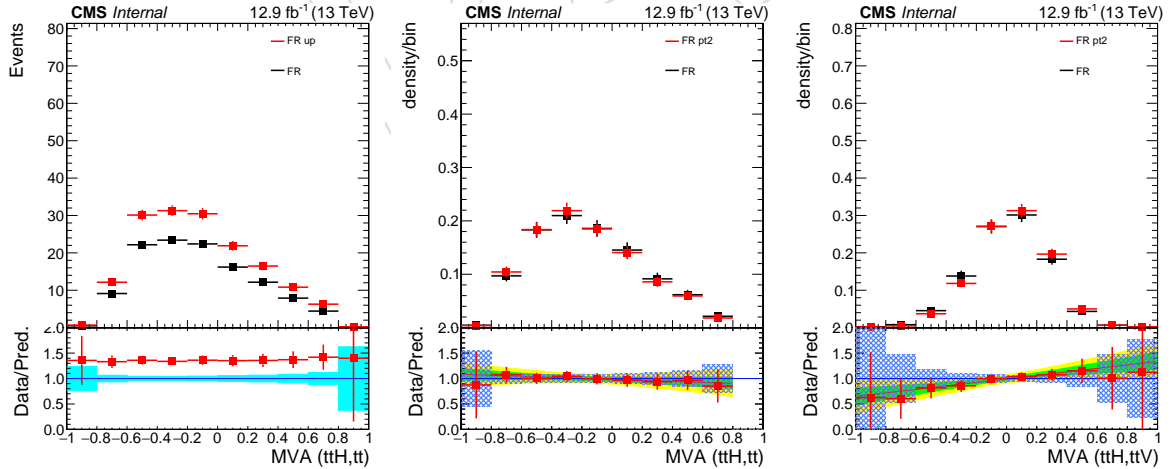


Figure 63: Left: example of the difference in background normalization arising from a coherent upwards shift of the fake rate map. Right: example of the difference induced on the shape of kinematic discriminators for semi-leptonic $t\bar{t}$ events, arising from trends in the fake rate map as a function of the lepton p_T and $|\eta|$.

8 Results

The results are interpreted by comparing the observed yields with the expectation from background and a 125 GeV SM Higgs boson. We introduce a signal strength parameter $\mu = \sigma/\sigma_{\text{SM}}$, and we scale by that value the expected yields from $t\bar{t}H$ without altering the branching fractions or the kinematics of the events.

Results in terms of the asymptotic 95% CL upper limit on μ are presented in Table 11. The observed (median expected) upper limit from the combination of all decay modes is 3.7 (1.2). The best fit signal strength is $2.1^{+0.9}_{-0.8}$ times the SM expectation, as shown in Table 12.

Category	Observed limit	Expected limit $\pm 1\sigma$
same-sign di-lepton	4.0	1.5 (+0.7) (-0.5)
tri-lepton	3.6	2.0 (+1.1) (-0.7)
combined	3.7	1.2 (+0.6) (-0.4)

Table 11: Expected asymptotic 95% CL upper limits on μ under the background-only hypothesis.

Category	μ fit $\pm 1\sigma$
same-sign di-lepton	2.2 (+1.0) (-0.9)
three lepton	1.4 (+1.2) (-0.9)
combined	2.1 (+0.9) (-0.8)

Table 12: Best fit of the signal strength parameter.

Combination with the result based on 2015 dataset

We perform a combination of the result presented in this note with the one [9] obtained from data collected in 2015 and corresponding to an integrated luminosity of 2.3 fb^{-1} . The combination is performed at datacard level, correlating the nuisances corresponding to the lepton efficiency, fake rate and jet energy scale uncertainties.

The result of the combination is shown in Table 13.

Dataset	μ fit $\pm 1\sigma$
2015	0.6 (+1.4) (-1.1)
2016	2.1 (+0.9) (-0.8)
combined	1.8 (+0.7) (-0.7)

Table 13: Best fit of the signal strength parameter, resulting from the combination of the 2015 and 2016 analyses.

837 A Control region plots

838 A.1 Lepton MVA sideband region

839 The 2lss selection is modified by requiring that only one of the two selected leptons fails the
 840 tight lepton requirements, but still passes those for the fakeable object. In this way, we select a
 841 region enriched in $t\bar{t}$ events, where the lepton that fails the tight requirement is a fake lepton.

842 It is worth noting that the contamination from QCD events is not taken into account by the
 843 simulation. We observe a good agreement between simulation and data in terms of the shape of
 844 observables used for the selection and as inputs to the BDT discriminators. The latter variables
 845 are shown in Fig. 67.

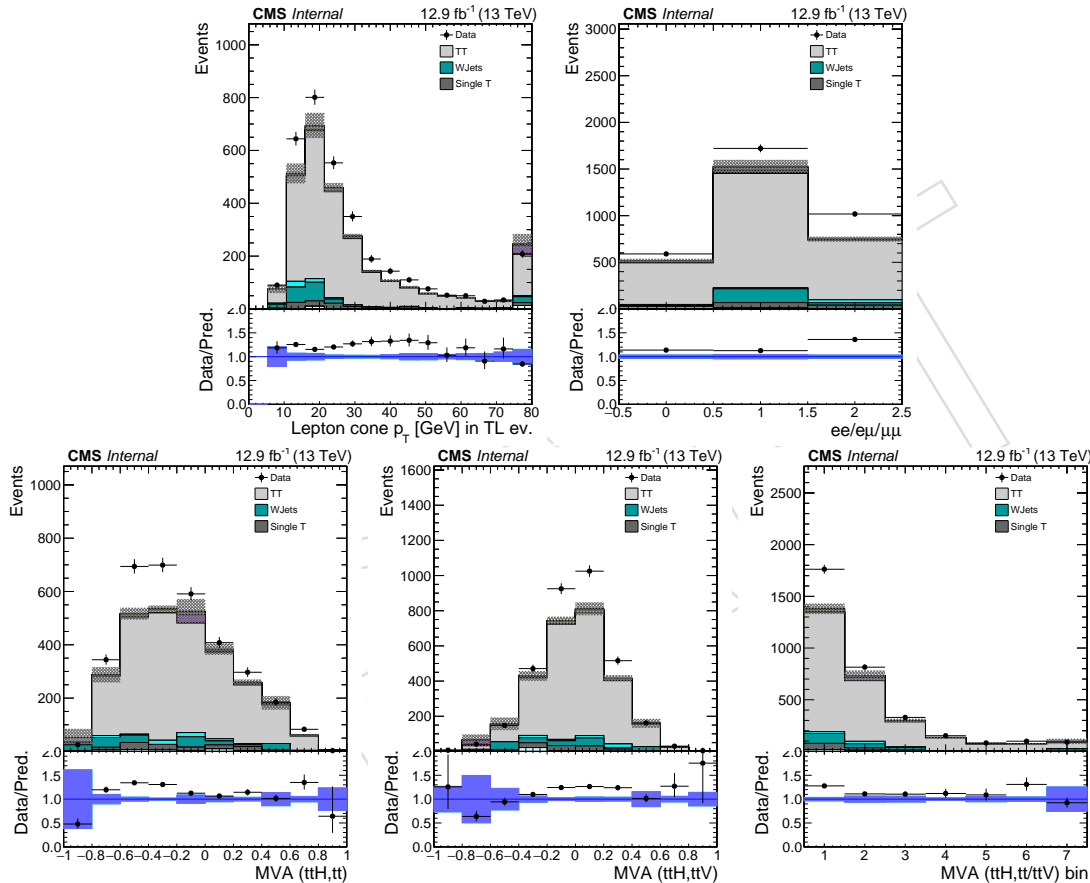


Figure 64: Data and simulation distributions in the 2lss control region with exactly one fakeable lepton failing the tight selection requirements. From top left to bottom right: the cone-corrected p_T of the failing lepton, the flavor of the lepton pair, the signal BDT discriminators against $t\bar{t}$ and $t\bar{t}V$ including the 2D-binned version as described in Section 5. Uncertainties are statistical only.

846 When further relaxing the selection to allow one or both leptons to fail the tight lepton re-
 847 quirements, the relative QCD contribution increases, as can be inferred by the plots shown in
 848 Fig. 68.

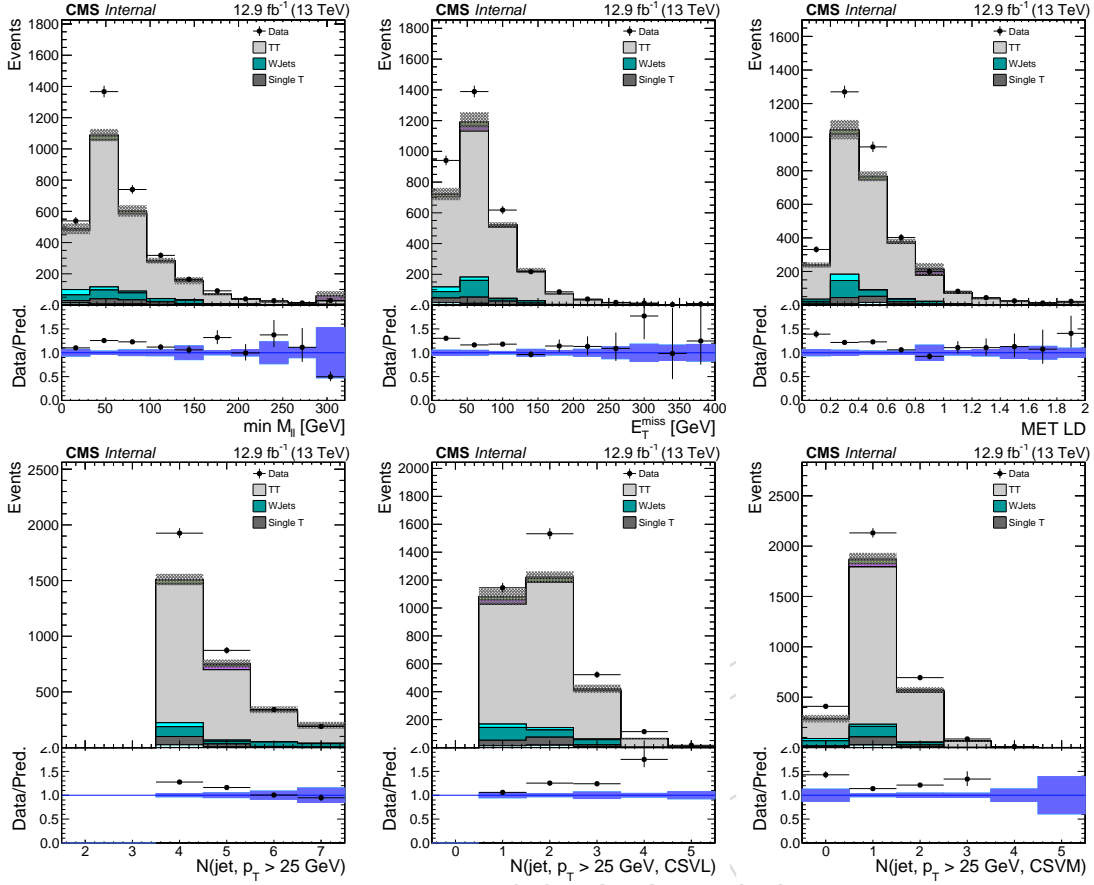


Figure 65: Data and simulation distributions in the 2lss control region with exactly one fakeable lepton failing the tight selection requirements. From top left to bottom right: the minimum invariant mass of loose di-lepton pairs, E_T^{miss} , $E_T^{\text{miss}} \text{LD}$, multiplicity of inclusive and b-tagged jets. cone-corrected p_T of the failing lepton, the flavor of the lepton pair, the signal BDT discriminators against $t\bar{t}$ and $t\bar{t}V$. Uncertainties are statistical only.

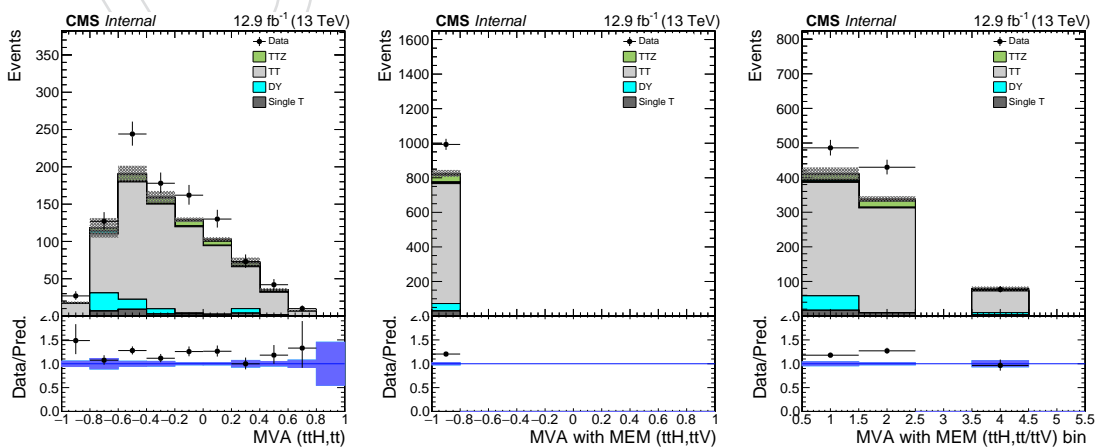


Figure 66: Same as Fig. 64, for the 3l category of the analysis.

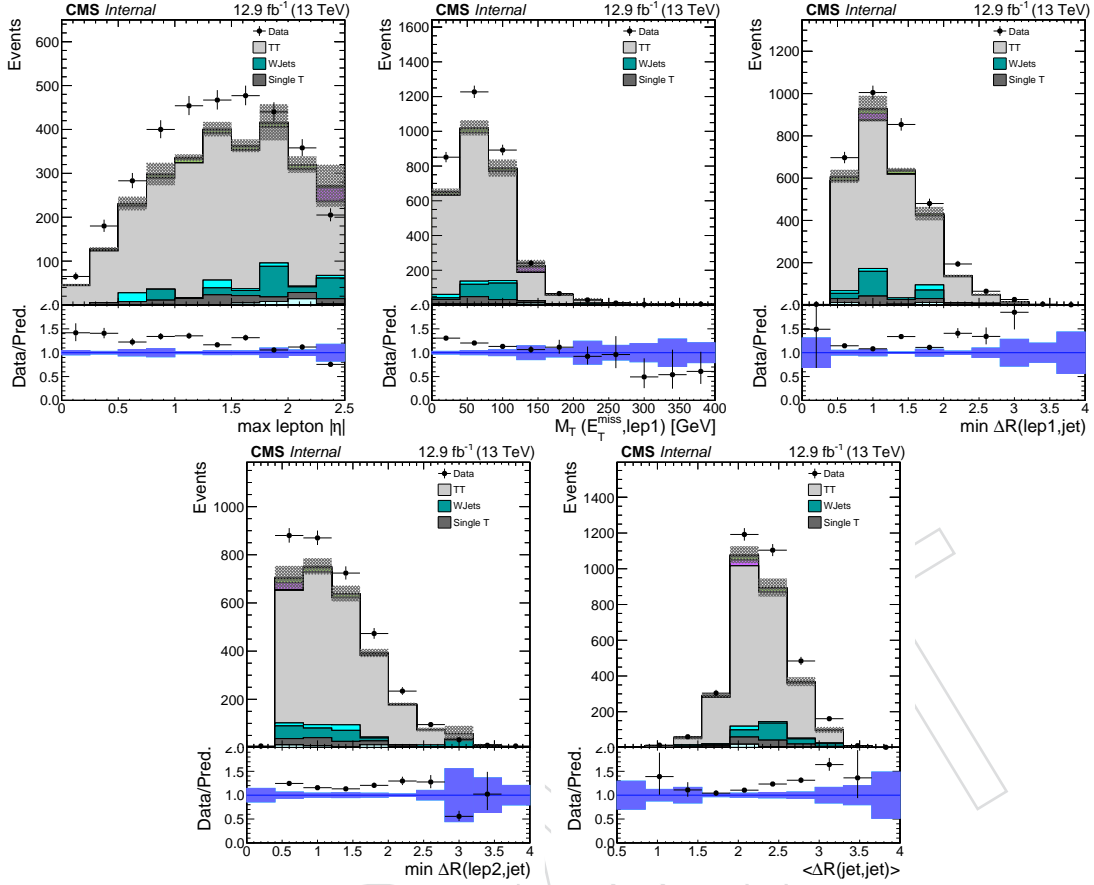


Figure 67: Distributions of several BDT input variables in the 2lss control region with exactly one fakeable lepton failing the tight selection requirements. Uncertainties are statistical only.

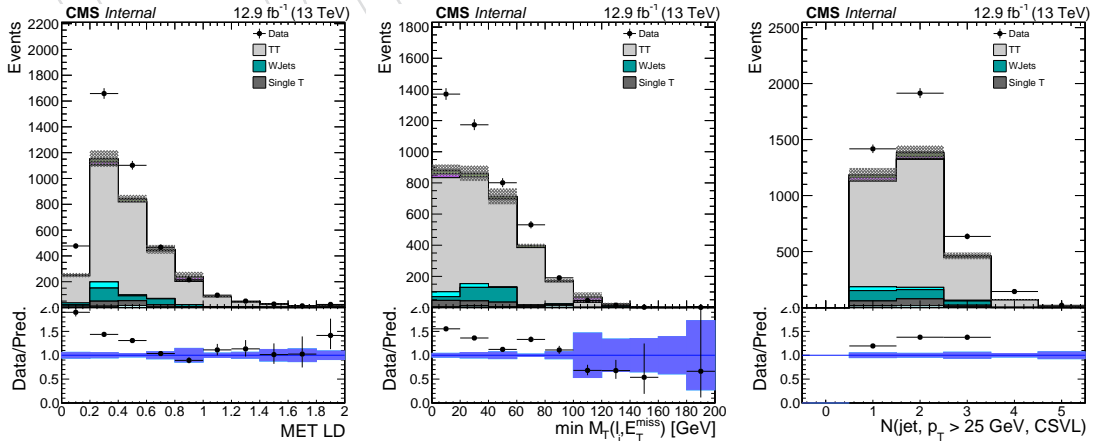


Figure 68: Distributions and simulation distributions in the 2lss control region where at least one fakeable lepton fails the tight selection requirements. Uncertainties are statistical only. QCD multi-jet events that are not included among the simulated physics processes here.

849 **A.2 Jet multiplicity sideband region**

850 This 2lss control region is enriched in fakes from $t\bar{t}$. It is obtained by requiring exactly three
 851 reconstructed jets in the final state, in the place of the requirement of at least four that is applied
 852 in the standard 2lss selection.

853 Fakes from W+jets are estimated by the fake rate method described in Section 7.4, applied on
 854 MC events, while all other processes are predicted by the simulation. Distributions of event
 855 observables are shown in Fig. 69-71.

856 Estimating instead the background from fake leptons and charge mis-assignment from data, as
 857 described in Section 7.4, we obtain the distributions shown in Fig. 72-74. In all cases we observe
 858 a satisfactory data/MC agreement, within the statistics currently available.

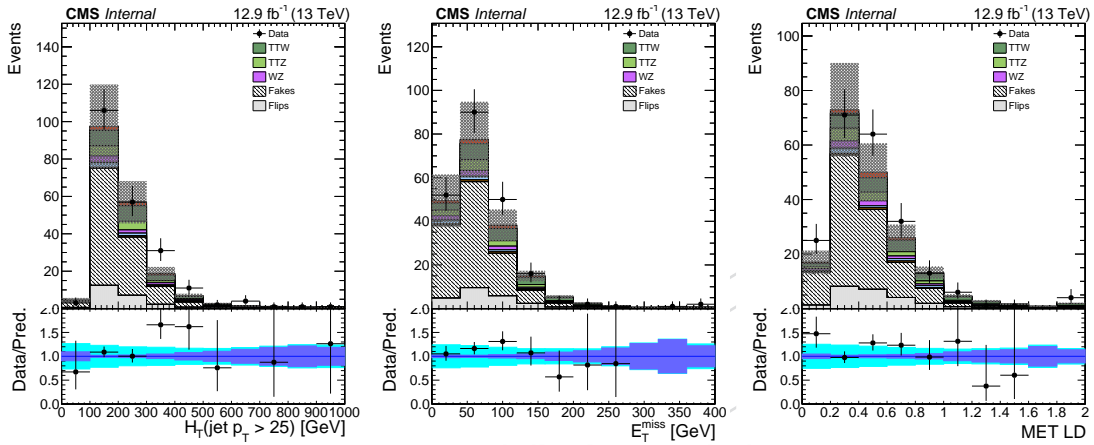


Figure 69: Data and simulation distributions in the 2lss control region with exactly three jets in the final state. From left to right: the H_T , the E_T^{miss} , the $E_T^{\text{miss}} \text{LD}$. Uncertainties are statistical only.

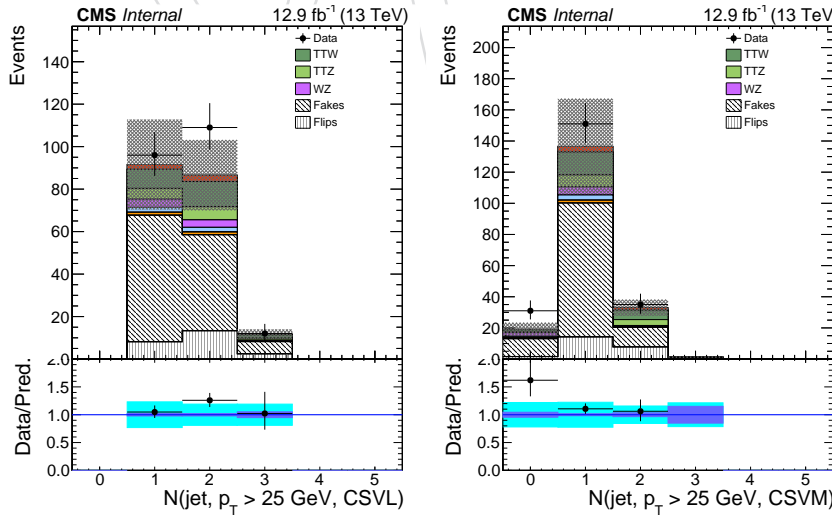


Figure 70: Data and simulation distributions for the number of jets passing the loose and medium working points of the CSV b-tagger, in the 2lss control region with exactly three jets in the final state. Uncertainties are statistical only.

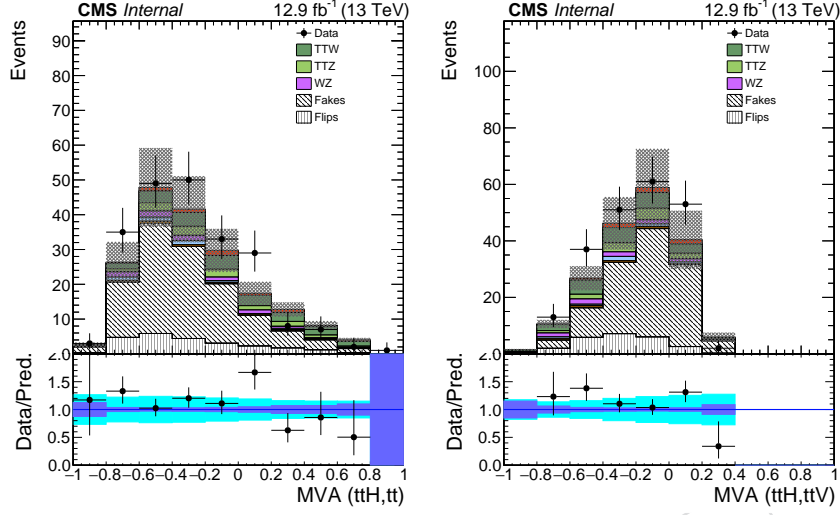


Figure 71: Data and simulation distributions of the discriminators against $t\bar{t}$ and $t\bar{t}V$ in the 2lss control region with exactly three jets in the final state. Uncertainties are statistical only.

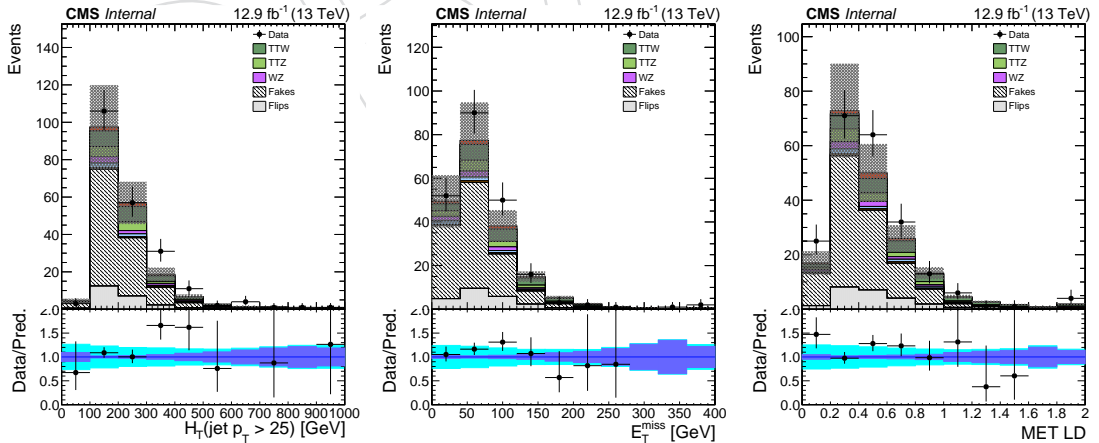


Figure 72: Data and simulation distributions in the 2lss control region with exactly three jets in the final state, with data-driven techniques applied to estimate the background from fake leptons and charge mis-assignment. From left to right: the H_T , the E_T^{miss} , the $E_T^{\text{miss}} \text{LD}$.

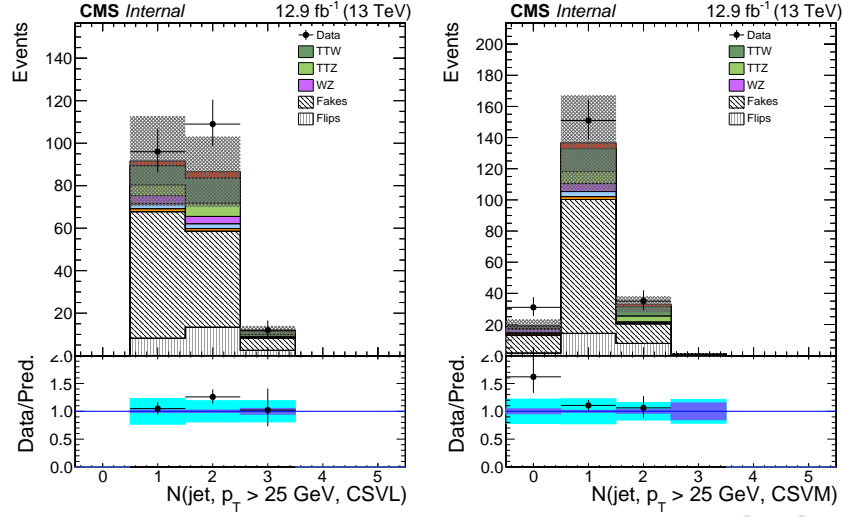


Figure 73: Data and simulation distributions for the number of jets passing the loose and medium working points of the CSV b-tagger in the 2lss control region with exactly three jets in the final state, with data-driven techniques applied to estimate the background from fake leptons and charge mis-assignment.

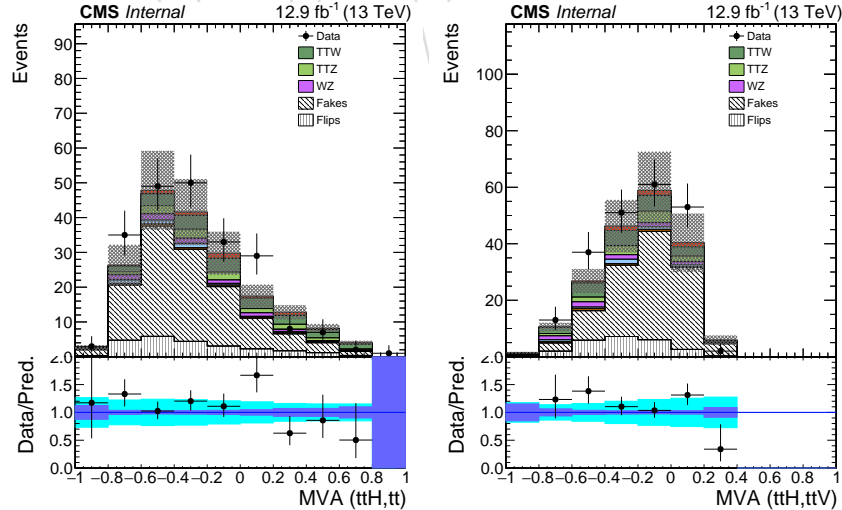


Figure 74: Data and simulation distributions of the discriminators against $t\bar{t}$ and $t\bar{t}V$ in the 2lss control region with exactly three jets in the final state, with data-driven techniques applied to estimate the background from fake leptons and charge mis-assignment.

859 **A.3 $t\bar{t} \rightarrow e^\pm \mu^\mp b\bar{b} \nu\bar{\nu}$**

860 This control region is enriched in $t\bar{t}$ events, and aims at validating the jet-related observables
 861 used in the analysis. The selection we apply is the same as in the 2lss category of the analysis,
 862 with the following modifications:

863

- 864 • the two selected leptons are required to be of opposite sign and flavor (one electron
 865 and one muon);
- 866 • the requirement on the number of jets is relaxed to ≥ 2 ;
- 867 • the requirements on the number of b-jets is relaxed to at least one jet passing the
 868 medium working point of the CSV tagger;

869 Distributions of some event observables are shown in Fig. 75.

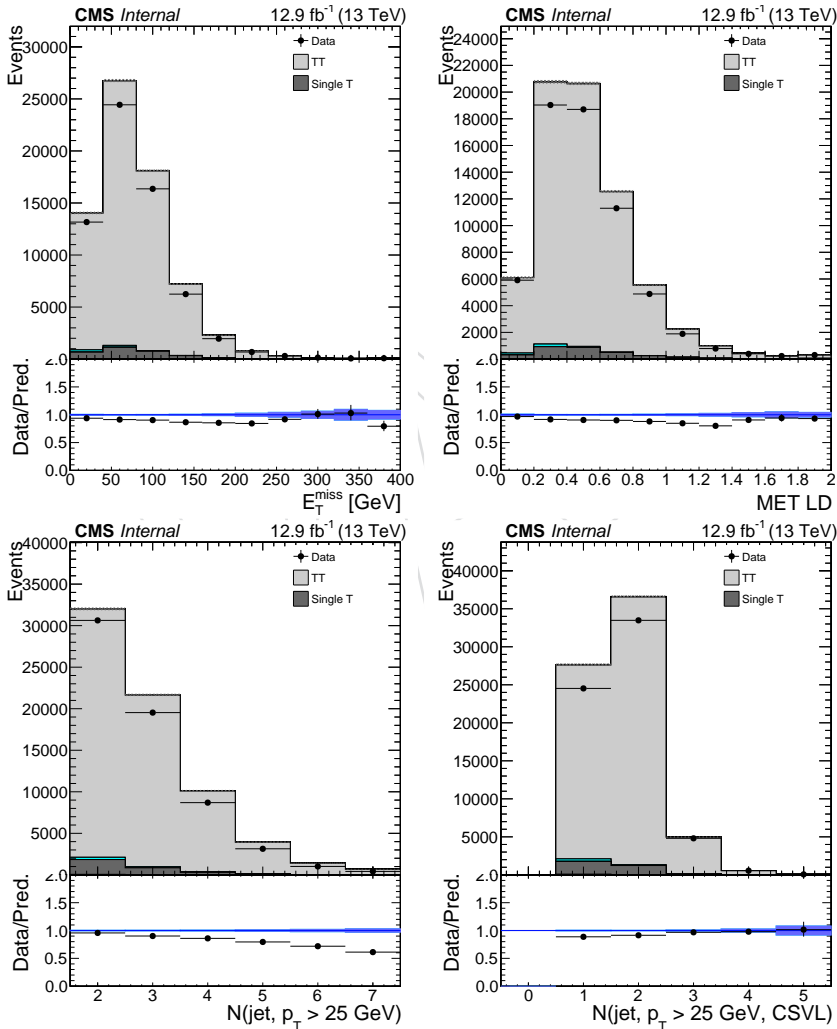


Figure 75: Data and simulation distributions in the $t\bar{t} \rightarrow e^\pm \mu^\mp b\bar{b} \nu\bar{\nu}$ control region. From top left to bottom right: the E_T^{miss} , the $E_T^{\text{miss}} \text{LD}$, the jet multiplicity and the number of jets passing the loose working point of the CSV tagger. Uncertainties are statistical only.

870 In order to disentangle the mismodeling of jet multiplicity in ttbar MC from the differential
 871 description of the other observables, we perform the same study in exclusive bins of jet multi-
 872 plicity (exactly 2, 3 or 4 jets) and normalize the total yield in the simulation to that observed
 873 in data. Figures 76-79 show a good description of the tested observables (b-jet multiplicity is
 874 expected to improve when the dedicated scale factors will be applied).

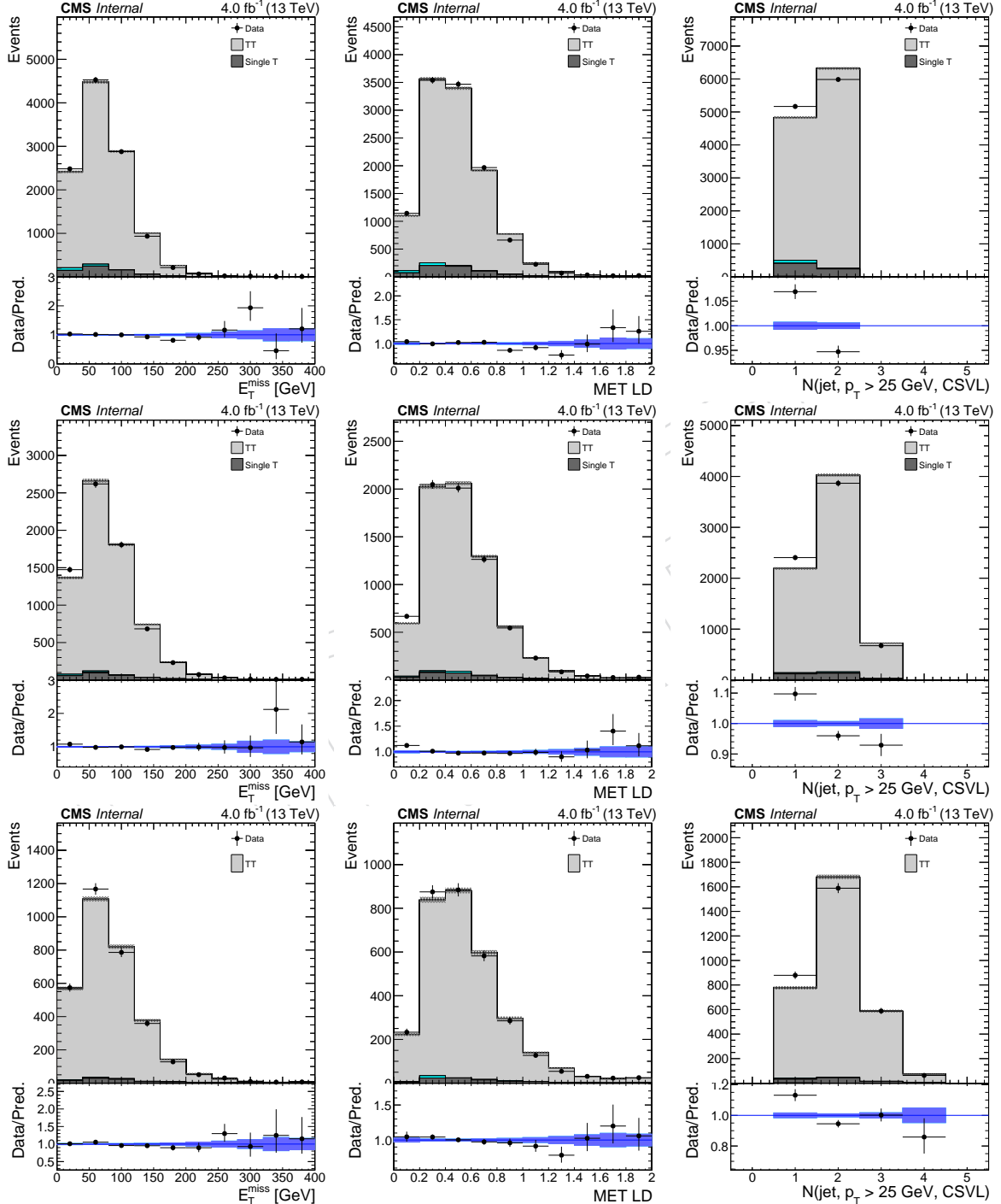


Figure 76: Data and simulation distributions in the $t\bar{t} \rightarrow e^\pm \mu^\mp b\bar{b} \nu\bar{\nu}$ control region, with exactly 2 jets (top row), 3 jets (central row) and 4 jets (bottom row) in the final state. Simulation is normalized to data. Uncertainties are statistical only. B-tag scale factors are not applied.

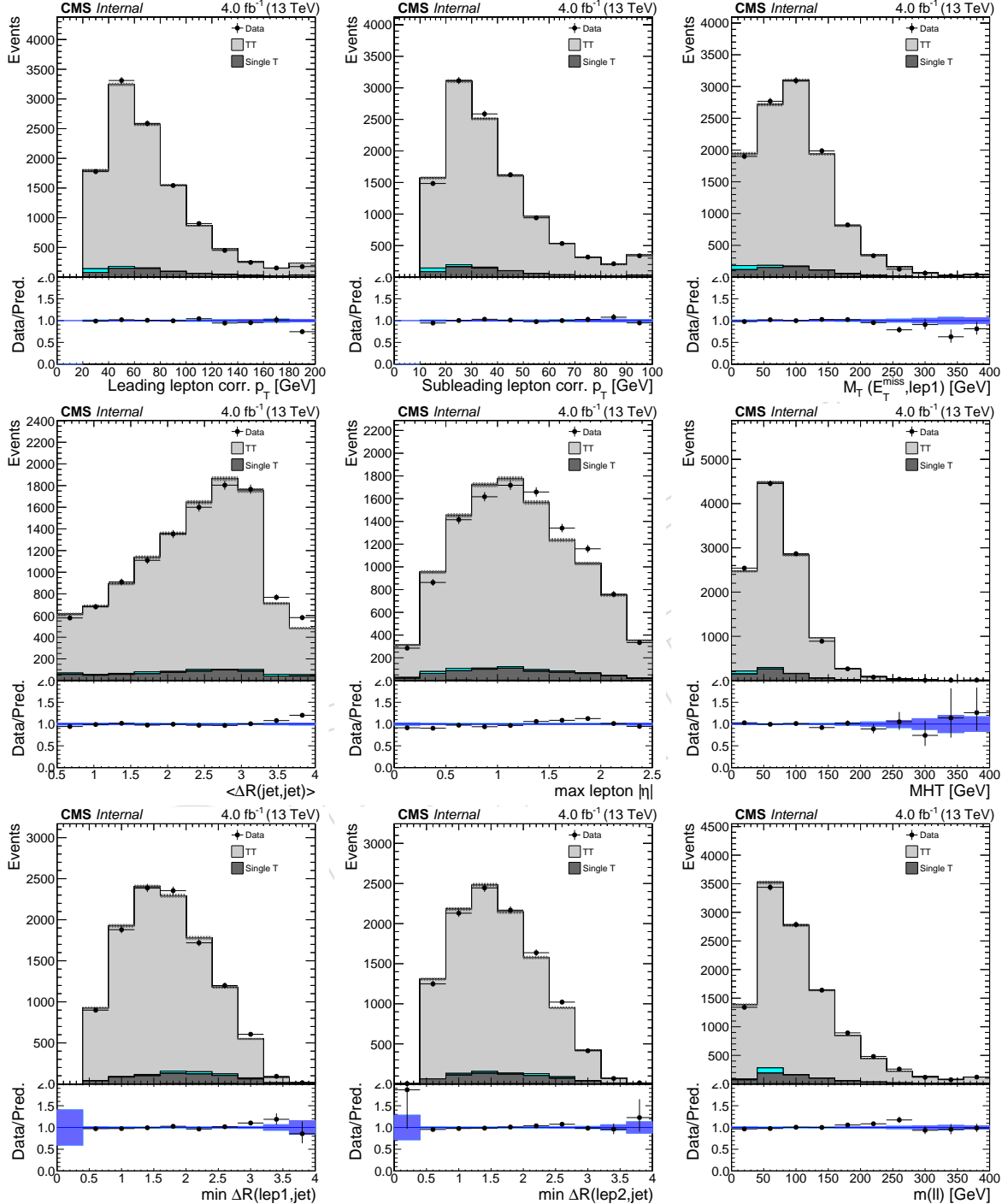


Figure 77: Data and simulation distributions in the $t\bar{t} \rightarrow e^\pm \mu^\mp b\bar{b} \nu\bar{\nu}$ control region, with exactly 2 jets in the final state. Simulation is normalized to data. Uncertainties are statistical only. B-tag scale factors are not applied.

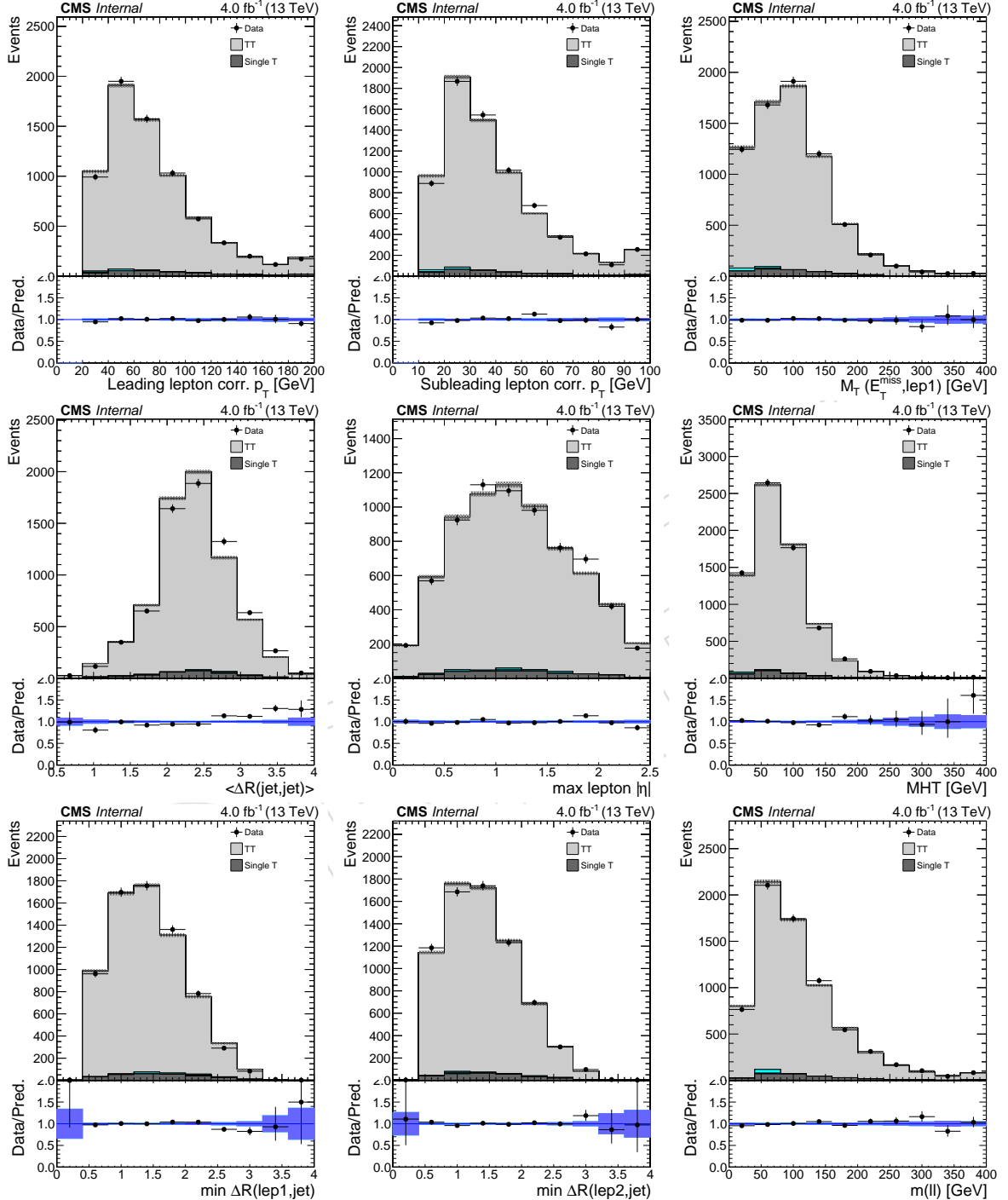


Figure 78: Data and simulation distributions in the $t\bar{t} \rightarrow e^\pm \mu^\mp b\bar{b} \nu\bar{\nu}$ control region, with exactly 3 jets in the final state. Simulation is normalized to data. Uncertainties are statistical only. B-tag scale factors are not applied.

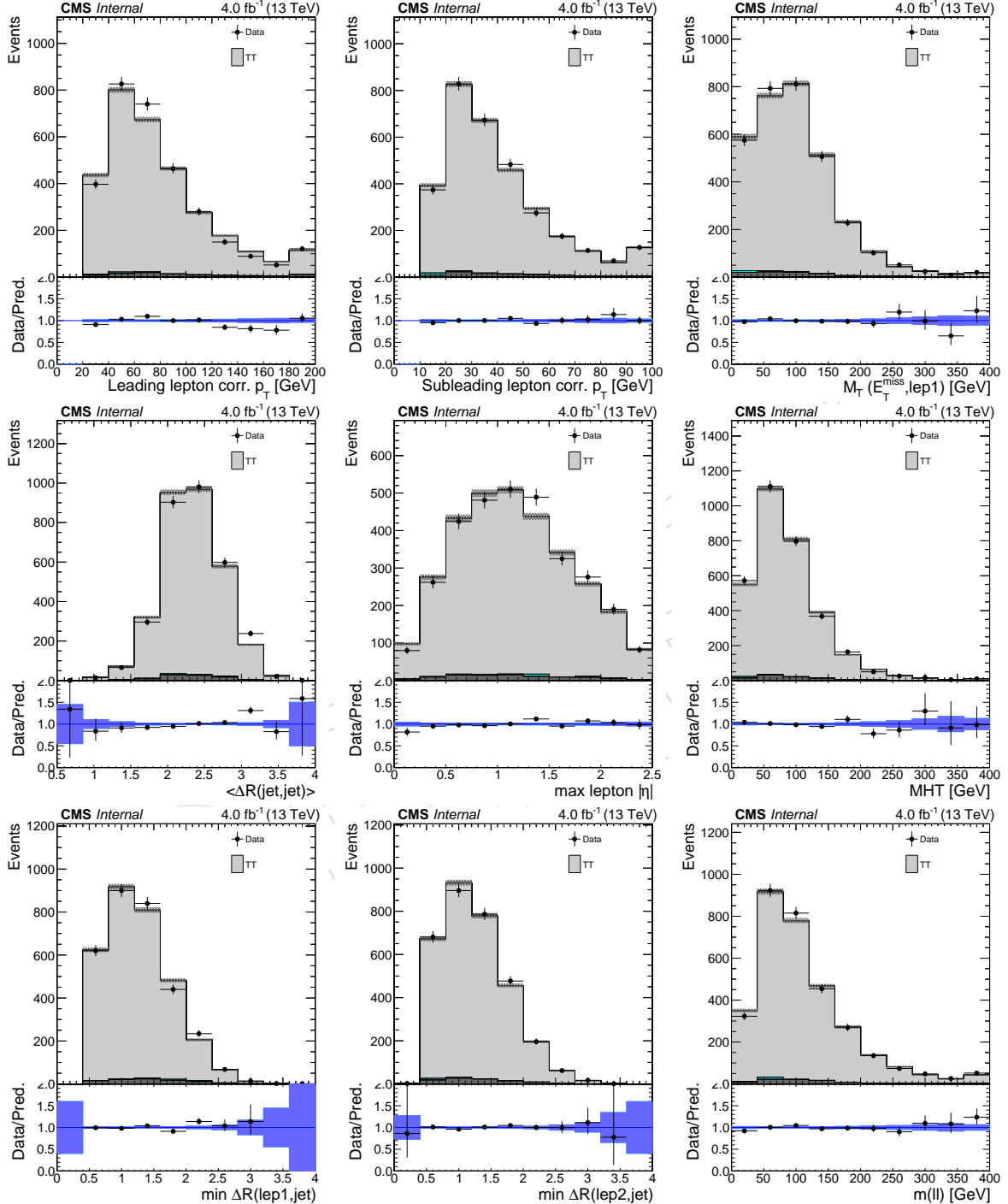


Figure 79: Data and simulation distributions in the $t\bar{t} \rightarrow e^\pm \mu^\mp b\bar{b} \nu\bar{\nu}$ control region, with exactly 4 jets in the final state. Simulation is normalized to data. Uncertainties are statistical only. B-tag scale factors are not applied.

875 **A.4 $WZ \rightarrow 3\ell$**

876 With this control region we want to validate our objects (signal leptons, $E_T^{miss} LD$, jets) in the
 877 three lepton final state. A sample enriched in $WZ \rightarrow 3\ell$ events is selected modifying the 31
 878 selection in the following way:

- 879

 880 - the Z veto is inverted, i.e. we require the presence of a pair of loose opposite-sign
 881 same-flavor leptons whose invariant mass is within 10 GeV from the nominal Z bo-
 882 son mass;
 883 - we require that no selected jets satisfy the medium working point of the CSV b-
 884 tagging discriminator

Some distributions are shown in Fig. 80.

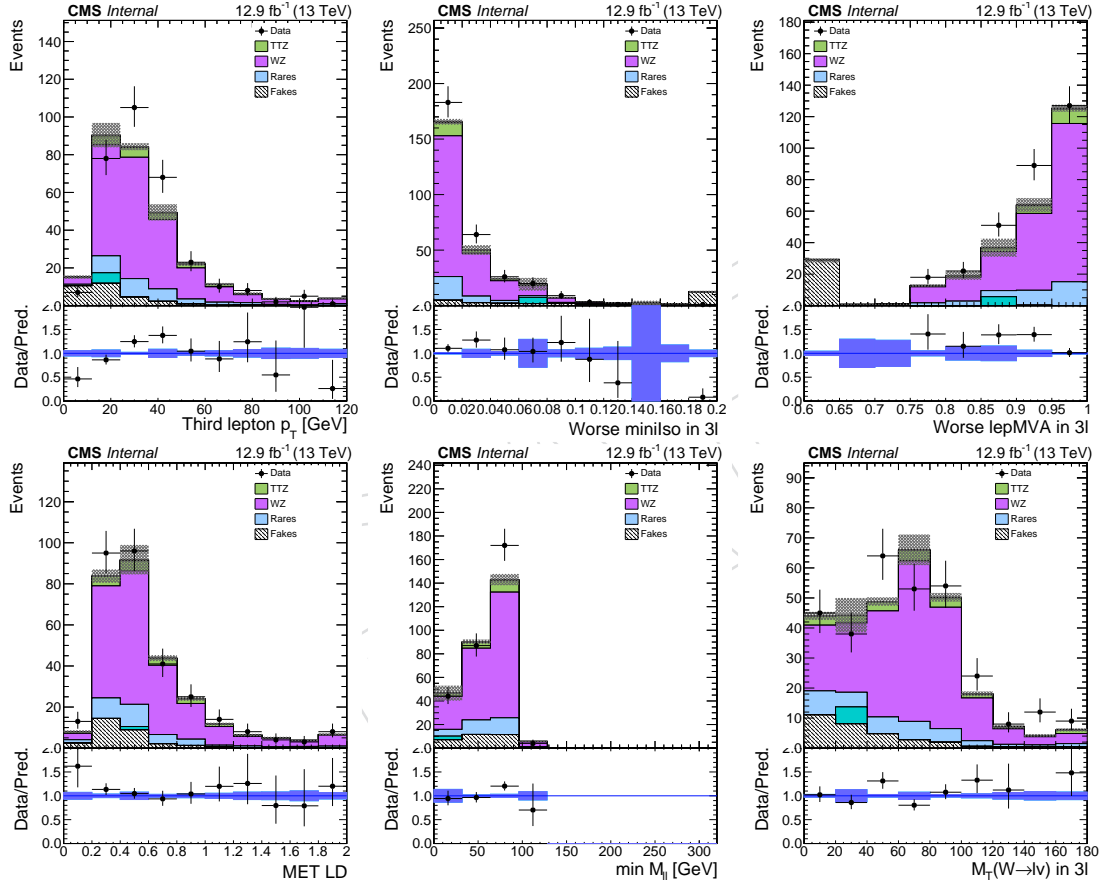


Figure 80: Data and simulation distributions in the $WZ \rightarrow 3\ell$ control region. From top left to bottom right: the p_T of the trailing lepton, mini isolation for the worse isolated lepton, worse lepton MVA value, the $E_T^{miss} LD$, the minimum invariant mass of any $\ell\ell$ couples, M_T of the W boson candidate.

885 A.5 $t\bar{t}Z \rightarrow 3\ell$

886 The prediction for the $t\bar{t}Z$ process is tested directly in a trilepton control region requiring two
 887 of the leptons to have the same flavour, opposite electrical charge and the invariant mass pair
 888 of the pair to be within 10 GeV of the nominal Z boson mass.

889 The definition of the control region differs from the one used for the 3l category of the analysis
 890 in the following points:

- 891 • the Z veto requirement is inverted, as described above;
- 892 • the cut on the multiplicity b-tagged jets is tightened, requiring at least two loose and
 893 one medium b-tagged jets

894 The background from non-prompt leptons is estimated from data. Some distributions are
 895 shown in Fig. 81.

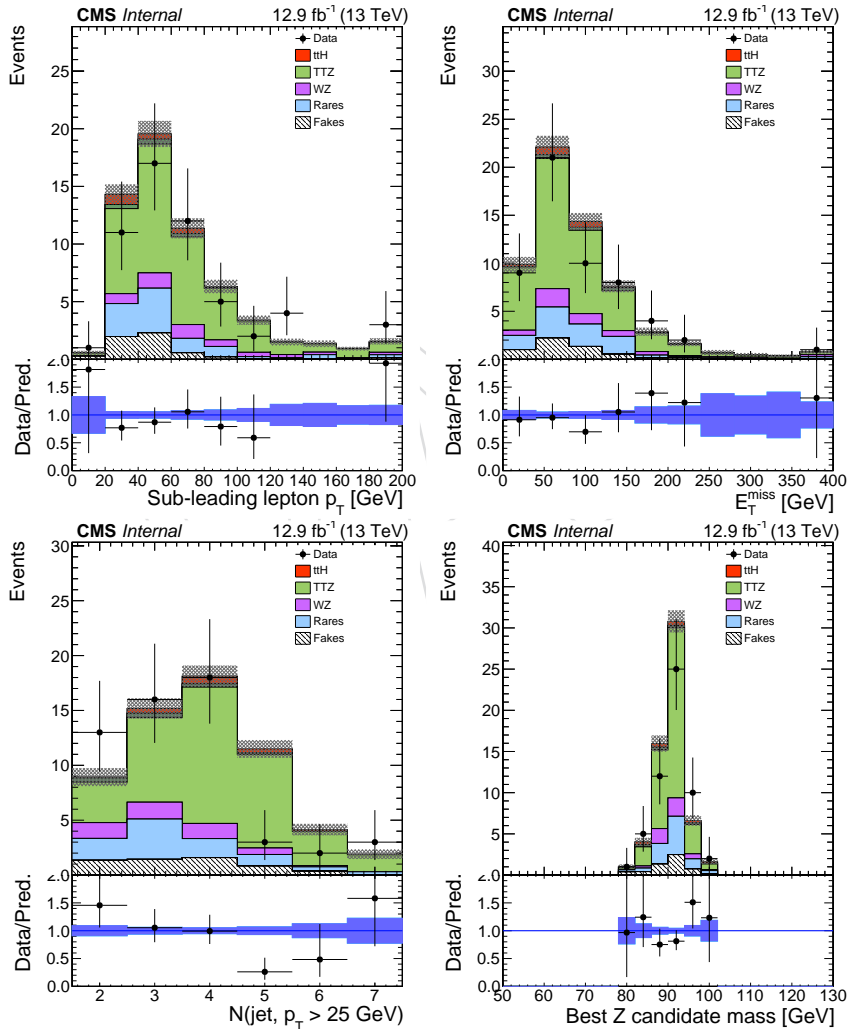


Figure 81: Data and simulation distributions in the $t\bar{t}Z \rightarrow 3\ell$ control region. From left to right: the p_T distribution of the second lepton ordered in p_T , the E_T^{miss} , the number of central jets with $p_T > 25$ GeV, the invariant mass of the best Z candidate.

896 When requiring also the presence of at least four selected jets, as expected for a fully recon-
 897 structed $t\bar{t}Z$ event, the control region becomes more pure in selecting $t\bar{t}Z$ events. This can
 898 be seen in the distributions in Fig. 82.

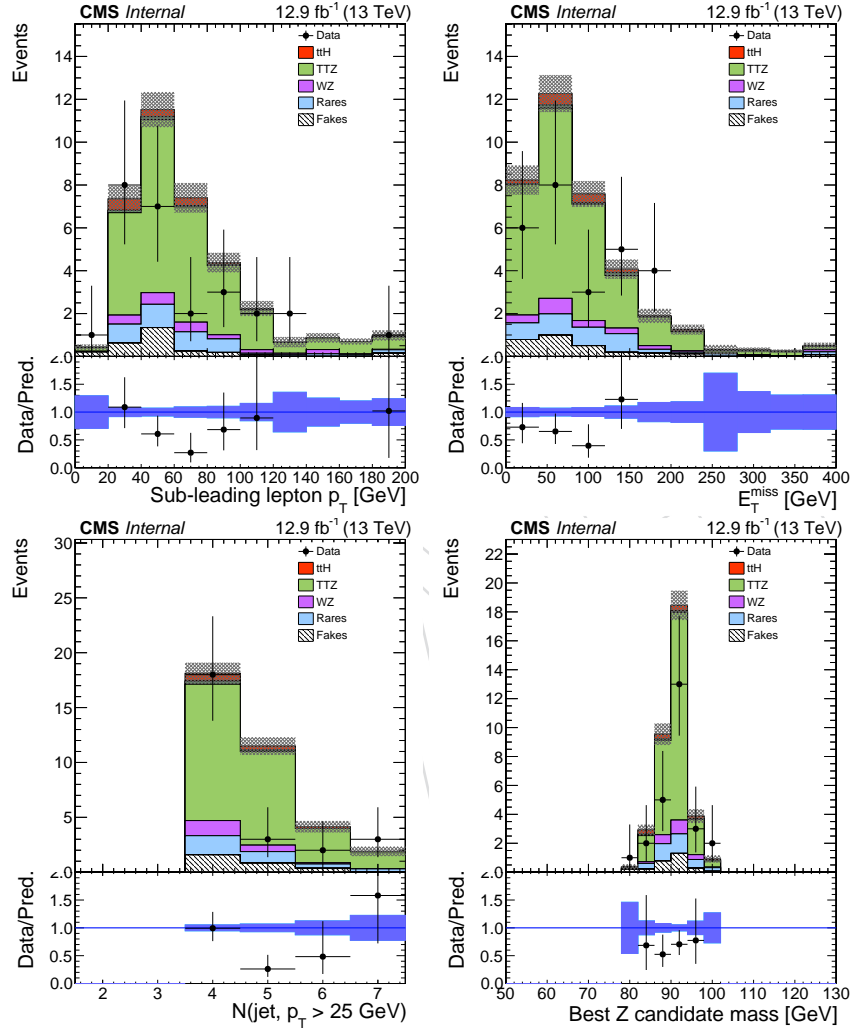


Figure 82: Data and simulation distributions in the $t\bar{t}Z \rightarrow 3\ell$ control region, with the additional requirement of at least four reconstructed jets. From left to right: the p_T distribution of the second lepton ordered in p_T , the E_T^{miss} , the number of central jets with $p_T > 25 \text{ GeV}$, the invariant mass of the best Z candidate.

899 B Matrix Element Method

900 In this section we describe the Matrix Element Method (MEM) for the $t\bar{t}H$ multilepton analysis.

901 B.1 The algorithm

902 The matrix element method consists in estimating the probability of an event to be compatible
 903 with the signal or background hypothesis, by computing the cross section of signal or back-
 904 ground processes on a given phase-space point, corresponding to the reconstructed kinematic
 905 configuration of the event.

For each hypothesis α , a weight $w_{i,\alpha}$ is computed for the event i using the following formula:

$$w_{i,\alpha}(\Phi') = \frac{1}{\sigma_\alpha} \int d\Phi_\alpha \cdot \delta^4(p_1^\mu + p_2^\mu - \sum_{k \geq 2} p_k^\mu) \cdot \frac{f(x_1, \mu_F) f(x_2, \mu_F)}{x_1 x_2 s} \cdot \left| \mathcal{M}_\alpha(p_k^\mu) \right|^2 \cdot W(\Phi' | \Phi_\alpha)$$

906 where σ_α is the cross section of the process α , Φ' is the 4-momenta of the reconstructed par-
 907 ticles in the event, $d\Phi_\alpha$ are the process-dependent integration variables, corresponding to the
 908 4-momenta of all the particles at the vertex in the hypothesis α , the δ symbol represents the
 909 momentum conservation between incoming and final state particles, $f(x, \mu_F)$ are the parton
 910 density function in the proton, x_1, x_2 are the fraction of proton energy carried by the incoming
 911 particles, $\left| \mathcal{M}_\alpha(p_k^\mu) \right|^2$ is the matrix element squared, and W are the transfer functions relating
 912 the energy of particles at the vertex with their energy reconstructed with the detector.

913 The MEM for $t\bar{t}H$ multilepton analysis is implemented in C++, thus can be easily interfaced with
 914 analysis code. The integration is performed using VEGAS [33] stratified/importance sampling
 915 implementation in ROOT. The matrix element squared is taken from Madgraph standalone
 916 C++ code at LO. The parton distribution functions are taken from LHAPDF6 [34]. Transfer
 917 functions are evaluated in CMS Run II Monte Carlo simulation. The phase space is analytic
 918 and implemented as in Madweight [35].

919 $t\bar{t}H$ and $t\bar{t}V$ hypotheses

920 In this analysis, the MEM for two lepton same-sign, three leptons and four leptons categories
 921 are considered. Three hypotheses corresponding to $t\bar{t}H$ signal, and $t\bar{t}W$, $t\bar{t}\gamma^*/Z$ irreducible
 922 backgrounds are included.

923 For all of the three processes, the W mass for W arising from top and Higgs decays is not
 924 treated as fixed, and follows a Breit-Wigner as specified by the matrix element squared. The
 925 W and γ^*/Z bosons produced in association with $t\bar{t}$ in $t\bar{t}V$ processes are also following a Breit
 926 Wigner. Interference between γ^* and Z is included in the $t\bar{t}\gamma^*/Z$ matrix element.

927 On the other hand, to decrease the number of integration variables, the masses of the top quark
 928 and Higgs bosons are set to 173 GeV and 125 GeV respectively. In this narrow-width approx-
 929 imation, matrix element and phase-space of top, anti-top and Higgs/ W/Z can be computed
 930 independently:

$$\left| \mathcal{M}_\odot \right|^2 = \left| \mathcal{M}_{TTH} \right|^2 \cdot \left| \mathcal{M}_{Top} \right|^2 \cdot \left| \mathcal{M}_{Antitop} \right|^2 \cdot \left| \mathcal{M}_{Higgs} \right|^2$$

$$d\Phi_{tot} = d\Phi_{gg \rightarrow TTH} \cdot d\Phi_{Top} \cdot d\Phi_{Antitop} \cdot d\Phi_{Higgs}$$

The phase-space $d\Phi_\alpha$ is made of the product of all final state particle $dE d\theta d\phi$. Integration over some of these variables can be cancelled using momentum conservation formula. We implemented the phase-space parametrization proposed in Madweight MEM paper. This was compared with a custom parametrization and found to be faster. Changes of variables are performed to make explicit the W mass, which follows always a Breit Wigner and do not depends on event kinematics, such that VEGAS can treat it as an independent variable. We reproduce here the integration variables which are used:

$$d\Phi_{top,had} \propto dE_b d\theta_b d\phi_b \cdot d\theta_{j1} d\phi_{j1} \cdot d\theta_{j2} d\phi_{j2} \cdot dm_W$$

$$d\Phi_{top,lep} \propto dE_b d\theta_b d\phi_b \cdot dE_l d\theta_l d\phi_l \cdot d\phi_\nu dm_W$$

$$d\Phi_{H \rightarrow 2l2\nu} \propto dE_{l1} d\theta_{l1} d\phi_{l1} \cdot dE_{l2} d\theta_{l2} d\phi_{l2} \cdot dE_{\nu1} d\theta_{\nu1} d\phi_{\nu1} \cdot d\phi_{\nu2} dm_W$$

$$d\Phi_{H \rightarrow l\nu jj} \propto dE_{j1} d\theta_{j1} d\phi_{j1} \cdot dE_{j2} d\theta_{j2} d\phi_{j2} \cdot dE_{l1} d\theta_{l1} d\phi_{l1} \cdot d\phi_{\nu1} dm_W$$

$$d\Phi_Z \propto dE_{l1} d\theta_{l1} d\phi_{l1} \cdot dE_{l2} d\theta_{l2} d\phi_{l2}$$

$$d\Phi_W \propto dE_l d\theta_l d\phi_l \cdot dE_\nu d\phi_\nu dm_W$$

931 For a given value of the integration variables, the momenta of all particles can be computed by
 932 solving a set of linear and quadratic equations. The b -quark mass is set to 4.7 GeV while the
 933 masses of the non- b quarks and leptons is set to 0.

934 The matrix element squared provided by Madgraph is leading order in pQCD, i.e. with no
 935 additional jets recoiling against the $t\bar{t}H/V$ system. However additional jets are present in data.
 936 To evaluate the ME, the $t\bar{t}H/V$ system needs to be boosted back along the Px/Py direction such
 937 that the incoming particles have no Px/Py component.

938 The pdf chosen is NNPDF2.3 LO QED. The factorization scale in the pdf and matrix element are
 939 chosen to be $\mu_F = (m_t + m_H)/2$ for $t\bar{t}H$, $\mu_F = (m_t + m_W)/2$ for $t\bar{t}W$, and $\mu_F = (m_t + m_{\gamma^*/Z})/2$
 940 for $t\bar{t}\gamma^*/Z$.

941 B.2 Treatment of jets and permutations

942 To evaluate the matrix element, leptons, jets and b -jets need to be assigned to the ME leptons
 943 and quarks. The jets assigned to the two b -quarks from tops are the two reconstructed jets with
 944 highest CSV value (disregarding the analysis categories 1b tight / 2b loose).

945 If all the needed jets are reconstructed, one has to choose 4 (2) jets among the remaining jets
 946 in two lepton same-sign (three lepton) category. In the general case, the jets to be assigned
 947 to the ME will arise from W decay from top or Higgs. For this reason, we select the dijet
 948 pair with mass closest to m_W . In the three lepton categories, when attempting to evaluate the
 949 $t\bar{t}H, H \rightarrow l\nu jj$ hypothesis, the dijet pair can also arise from W^* decay. Here we choose the dijet
 950 pair with lowest dijet mass (dijet mass is bounded by the p_T cut on the jets to be mostly greater
 951 than 50 GeV). Similarly in two lepton same-sign categories, once the jet pair with mass closest
 952 to m_W are selected, two more jets with lowest dijet mass are selected. It was shown that this
 953 "mixed" way of selecting jets performs better than selecting only jet pairs by mass closest to W
 954 mass.

955 If the needed jets are not all reconstructed (e.g. not passing jet identification or escaping detec-
 956 tor acceptance), in principle the matrix element can not be evaluated. However, by expanding
 957 the phase-space with additional integration variables for the missing jets, it is possible to cir-
 958 convene this difficulty. This feature is implemented in the 1-missing and 2-missing jets cases.

Category/Hypothesis	$t\bar{t}Z$	$t\bar{t}W$	$t\bar{t}H, H \rightarrow l\nu jj$	$t\bar{t}H, H \rightarrow 2l2\nu$	$t\bar{t}H$
3l_2b_2j	4 or 8	4	8	8	16
3l_2b_1j	4 or 8	4	8	8	16
3l_2b_0j	2 or 4	4	4	4	8
4l_2b	4 or 8	0	0	8	8
2lss_2b_4j	0	8	96	0	96
2lss_2b_3j	0	8	8	0	8
2lss_2b_2j	0	8	4	0	4

Table 14: Number of permutations of all hypotheses and categories

959 Thus the MEM can be computed for all events selected with the baseline analysis, requiring
 960 $\geq 4(2)$ jets including b-jets, in 2lss (3l) category.

961 Since we cannot know a priori what is the correct lepton and jet assignment to the ME partons,
 962 the ME is evaluated for all possible permutations of leptons and jets. Table 14 summarizes the
 963 number of permutations for all categories and hypotheses.

964 For all hypotheses and categories, there are 2 permutations arising from b-jet permutation (top
 965 or anti-top). The $t\bar{t}Z$ hypothesis can be computed in 3l (with 1 lepton from leptonic decay
 966 and 2 leptons from Z decay) and 4l categories (2 leptons from both leptonic top decay and 2
 967 leptons from Z decay). In 3l/4l categories, there can be 1 or 2 same flavour opposite sign pair
 968 to make a Z, thus 1 or 2 lepton permutations are allowed, the other lepton(s) being assigned
 969 to the top/anti-top according to the sign of their charge. In 3l categories, 2 jet permutations
 970 are arising from the hadronic top decay. The $t\bar{t}W$ ME does not have quarks in 3l categories
 971 (2 leptons from leptonic top decay and 1 lepton from associated W production), thus no jet
 972 permutations are allowed. In 2lss categories, 2 jets among 4 can be assigned to the ME (from a
 973 hadronic top decay), leading to 2 jet permutations in any case. The $t\bar{t}H, H \rightarrow 2l2\nu$ hypothesis
 974 can be computed for 3l (with one leptonic top decay) and 4l categories (two leptonic top decays)
 975 only. The $t\bar{t}H, H \rightarrow l\nu jj$ hypothesis can be computed for 2lss (with one hadronic top decay) and
 976 3l (both leptonic top decays). The biggest number of permutations is found in the 2lss_2b_4j
 977 category, where permutations have to be done within the 4 jets. To reduce the number of
 978 permutations in the special case of 2lss_2b_3j category (time consuming since there are more
 979 integration variables) the missing jet can only be assigned to the W from Higgs decay, assuming
 980 that the jet is lost because of not passing the p_T requirement.

Once the MEM is computed for each of the permutations, an average weight is computed for each hypothesis. The weights with null value are excluded from the average (found to be slightly more discriminating than including them):

$$\begin{cases} w_\alpha = 10^{-300} & \text{if } \sum w_i = 0 \\ w_\alpha = \frac{1}{N_{w_i \neq 0}} \sum_{w_i \neq 0} w_i & \text{else} \end{cases}$$

981 Transfer functions

982 The transfer functions $W(\Phi' | \Phi_\alpha)$ give the probability density of measuring a set of observables
 983 Φ' with the detector, given a phase space point Φ_α at ME level. For this analysis, the following
 984 approximations are made. The lepton energy and its direction is assumed to be perfectly
 985 measured. The direction of quarks is assumed to be perfectly measured by the direction of
 986 the reconstructed jet. Thus no transfer functions are used for leptons, while jet energy transfer
 987 functions are included in the MEM.

988 Jets and b-jets energy transfer functions are evaluated in MC simulation with *CMSSW_7_6_X*.
 989 The pdfs are histograms parameterized as a function of E_{rec}/E_{gen} , where E_{rec} is the jet re-
 990 constructed energy after jet energy scale/resolution correction and E_{gen} is the energy of the
 991 matched parton. Transfer functions are defined in 3 bins of jet pseudorapidity ($|\eta| < 0.8$,
 992 $0.8 < |\eta| < 1.6$, $1.6 < |\eta| < 2.4$) and 6 bins of jet energy ($25 < E < 50$, $50 < E < 80$,
 993 $80 < E < 120$, $120 < E < 200$, $200 < E < 300$, $E > 300$ GeV). B-jet response is found to
 994 be slightly lower than jet response, as expected (due to missing momentum of neutrinos from
 995 B-hadron decays escaping detection). Transfer functions measured in $t\bar{t}H$ samples are used.
 996 Distributions were cross-checked in $t\bar{t}V$ and $t\bar{t}$ samples and found to behave similarly. Exam-
 997 ples of jets and b-jets transfer functions are shown fig. 83.

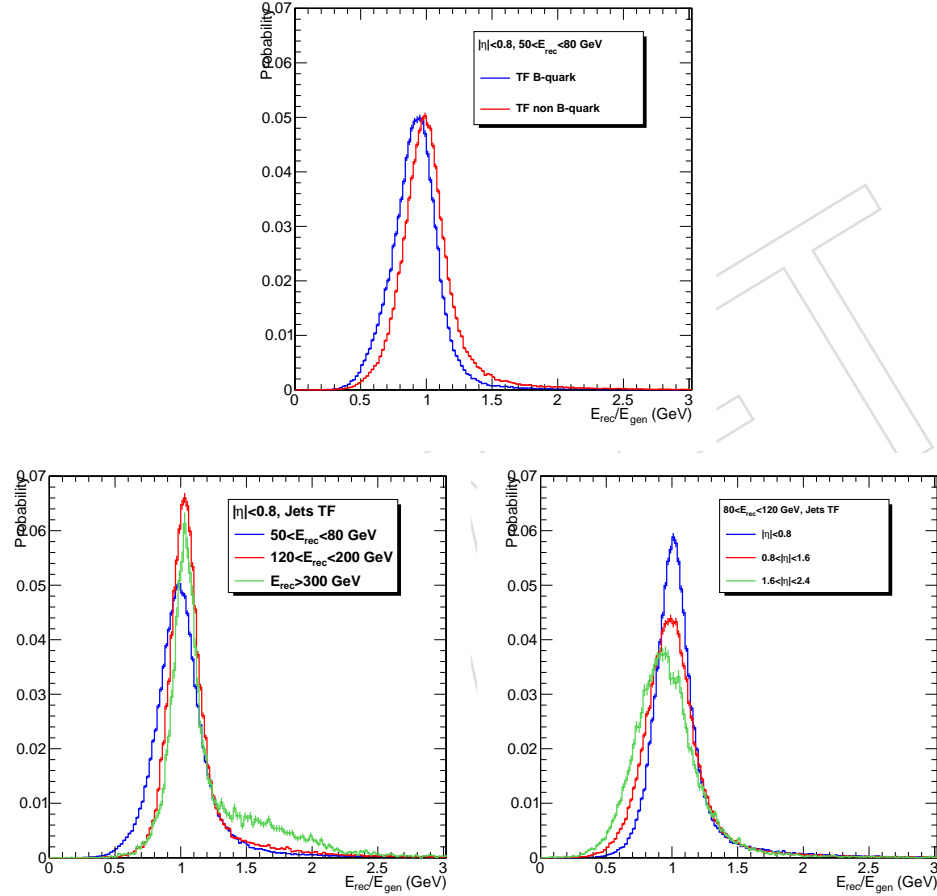


Figure 83: Example of jets transfer functions for (a) b-jets and non-b jets, (b) variation of jets TF with energy (c) variation of jets TF with η .

998 If a jet is missing at reconstructed level, its transfer function is set to 0 if the associated MEM
 999 quark has $|\eta| > 2.4$, and to 1 if $|\eta| < 2.4$.

Another set of transfer functions is used to constrain the total momentum of the $t\bar{t}H/V$ system. According to momentum conservation between initial state and final state particles, integration over the phase space of initial particles is cancelled. Despite the cancellation, one can constrain the total momentum computed with the MEM at parton level with the total momentum reconstructed, by using a transfer function. For practical reason, this transfer function is approximated with a missing transverse energy transfer function. The parameterization is using the mET covariance matrix $|V_{x,y}|$ computed event by event to build a 2D pdf, as a function of mET

P_x and P_y :

$$TF(E_x^{miss}, E_y^{miss}) = \frac{1}{2\pi\sqrt{|V_{x,y}|}} \exp\left(-\frac{1}{2}(\vec{E}_T^{miss} - \sum \vec{\nu}_T)^T V_{x,y}^{-1} (\vec{E}_T^{miss} - \sum \vec{\nu}_T)\right)$$

1000 B.3 MEM discriminant

1001 According to the Neyman-Person lemma, the likelihood of signal and background is the most
 1002 powerful test statistic for hypothesis testing. In the 2lss categories, a likelihood is built with the
 1003 $t\bar{t}H$ and $t\bar{t}W$ hypotheses, while in the 3l categories, a likelihood is built with $t\bar{t}H$ and $t\bar{t}W+t\bar{t}Z$
 1004 hypotheses as follows:

$$\begin{aligned} L_{2lss} &= -\log\left(\frac{\sigma_{TTW}w_{TTW}}{\sigma_{TTH}w_{TTH} + k \cdot \sigma_{TTW}w_{TTW}}\right) \\ \left\{ \begin{array}{ll} L_{3l} = -\log\left(\frac{\sigma_{TTZ}w_{TTZ}+k \cdot \sigma_{TTW}w_{TTW}}{\sigma_{TTH}w_{TTH}+\sigma_{TTZ}w_{TTZ}+k \cdot \sigma_{TTW}w_{TTW}}\right) & \text{SFOS} \\ L_{3l} = -\log\left(\frac{k \cdot \sigma_{TTW}w_{TTW}}{\sigma_{TTH}w_{TTH}+k \cdot \sigma_{TTW}w_{TTW}}\right) & \text{no SFOS} \end{array} \right. \\ L_{4l} &= -\log\left(\frac{\sigma_{TTZ}w_{TTZ}}{\sigma_{TTH}w_{TTH} + \sigma_{TTZ}w_{TTZ}}\right) \end{aligned}$$

1005 MEM weights are weighted by relevant process cross section in the likelihood. Note that the
 1006 $t\bar{t}Z$ hypothesis can be included only if there is at least one same flavour opposite sign pair to
 1007 build a Z.

1008 A multiplicative factor k is included to counterbalance the missing phase space in the $t\bar{t}W$ hy-
 1009 pothesis with respect to the other processes (the $t\bar{t}W$ ME has 2 jets less in the matrix element
 1010 relative to $t\bar{t}H$ and $t\bar{t}Z$). In the case of 3l categories, k was tuned for each category (0/1/2 miss-
 1011 ing jets) to maximize the signal to background discrimination. In the 2lss categories, changing
 1012 k does not improve discrimination but allows easier fit of the final distributions.

1013 Final yields after event selection in CMSSW_7_6_X MC with 2015 luminosity assumed, are
 1014 shown fig. 84 for 2lss categories fig. 85 for 3l categories.

1015 Comparison with TTV BDT

1016 The performance of MEM discriminants is compared on fig. 86 for 2lss categories and fig. 87
 1017 for 3l categories. Performance is in any case comparable, slightly lower in 2lss categories, and
 1018 equivalent or slightly better in 3l categories. The performance is better for categories where all
 1019 the jets are reconstructed. There is almost no discrimination when 2 jets are missing, which is
 1020 also the case for the TTV BDT.

1021 MEM as input variable to the TTV BDT

1022 Given that the performances of TTV BDT and MEM discriminants are similar, it makes sense to
 1023 train BDT including the MEM. We train new BDT's using Madgraph $t\bar{t}W$ and $t\bar{t}Z$ large samples
 1024 with same setup used for training BDT TTV, but including MEM weights. Three trainings are
 1025 performed:

- 1026 • 2lss category: TTV BDT inputs + $\log(w_{TTH}) + \log(w_{TTW}) + \text{catJets}$, where catJets is
 1027 the jet category (0/1/2-missing jets)

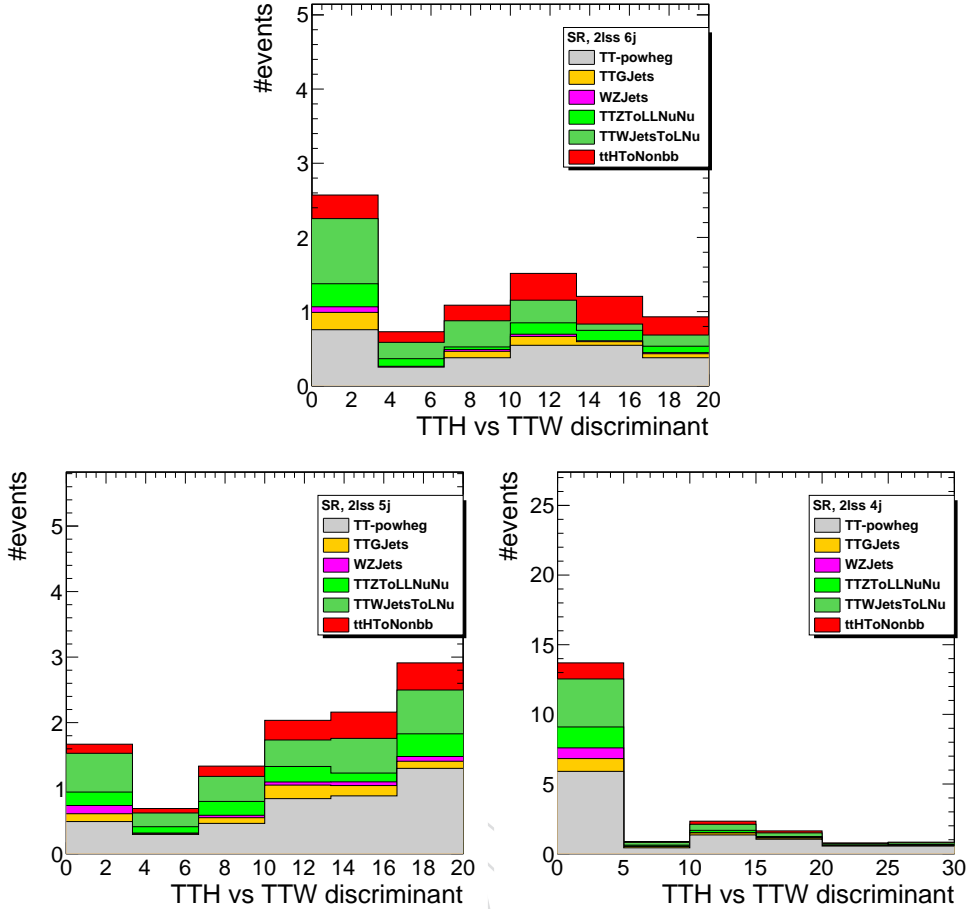


Figure 84: Final yields of MEM discriminants in 2lss signal region for (a) 0 missing jets, (b) 1 missing jets, (c) 2 missing jets.

- 3l/4l categories with a SFOS lepton pair: TTV BDT inputs + $\log(w_{TTH}) + \log(w_{TTW}) + \log(w_{TTZ}) + \text{catJets}$
- 3l categories without SFOS lepton pair: TTV BDT inputs + $\log(w_{TTH}) + \log(w_{TTW}) + \text{catJets}$

The $\log(w)$ are the \log of average MEM weight excluding null weights. catJets variable is included to make the BDT aware of the missing jet category.

Results are shown on fig.88 for 2lss category, fig.89 for 3l without SFOS lepton pair, fig. 90 for 3l with a SFOS lepton pair, and fig. 91 for 4l. Performance of BDT including MEM is greater than the previous training of TTV BDT for all categories, by a few % in signal efficiency for a given background rejection in 2lss categories and up to 10-15% in 3l and 4l categories.

B.4 MEM distributions after event selection

Figures 92 and 93 show the distribution of log of MEM amplitudes after the full 3l event selection, in the signal and in the lepton MVA sideband region.

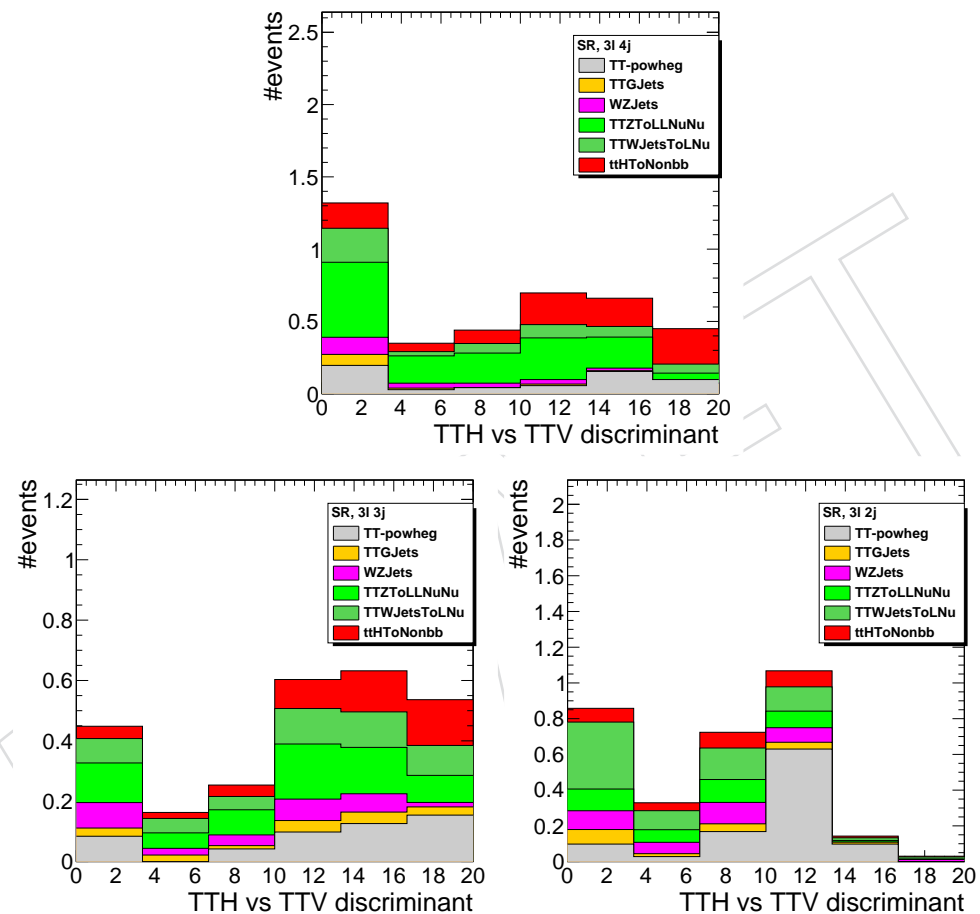


Figure 85: Final yields of MEM discriminants in 3l signal region for (a) 0 missing jets, (b) 1 missing jets, (c) 2 missing jets.

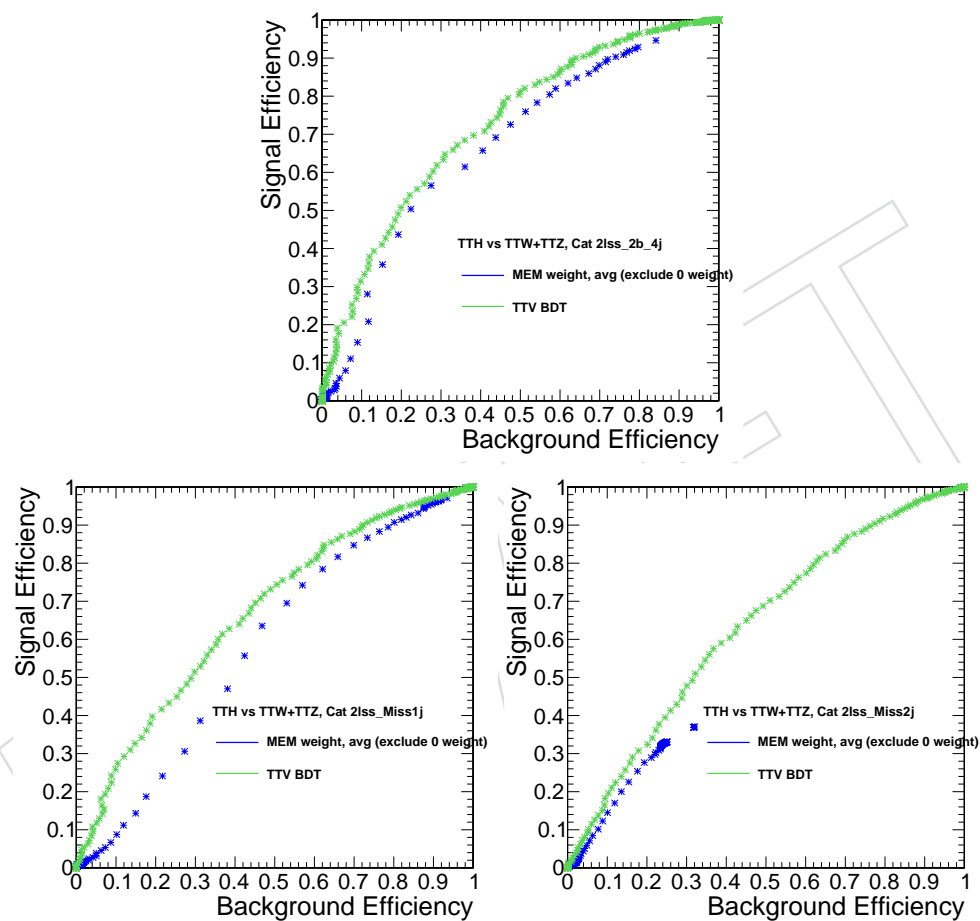


Figure 86: Comparison of MEM discriminants in 2lss signal region for (a) 0 missing jets, (b) 1 missing jets, (c) 2 missing jets.

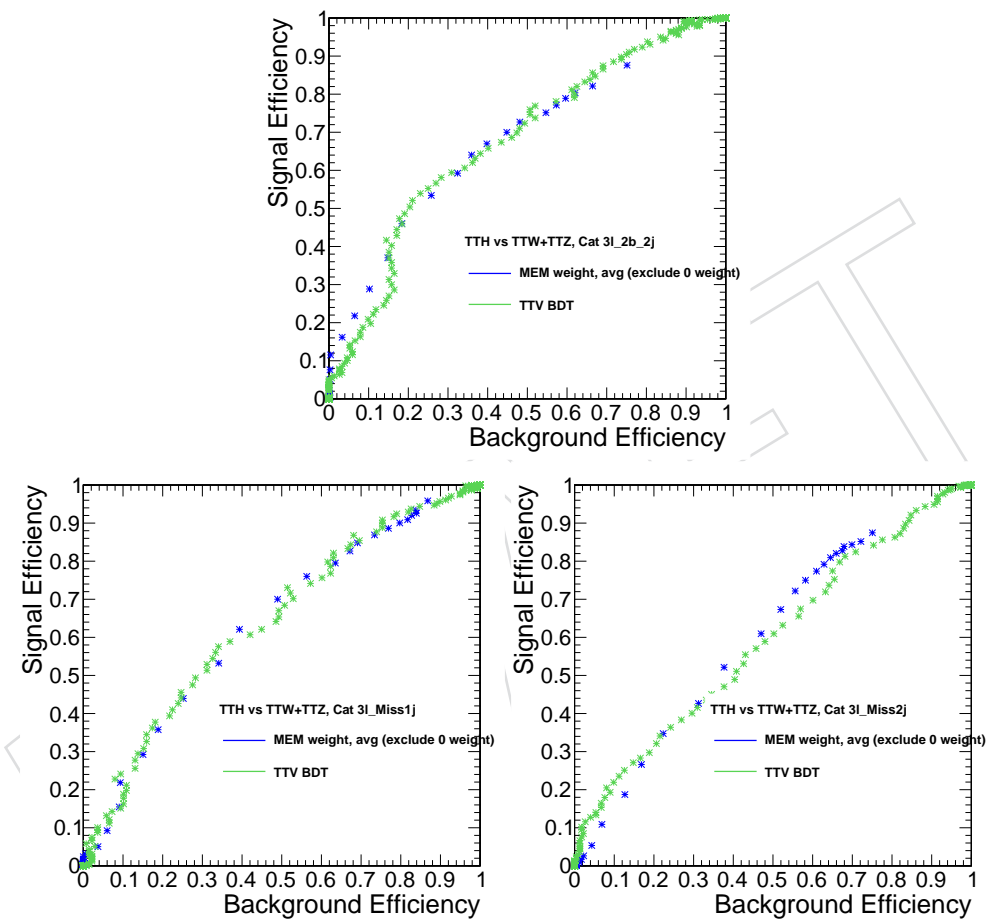


Figure 87: Comparison of MEM discriminants in 3l signal region for (a) 0 missing jets, (b) 1 missing jets, (c) 2 missing jets.

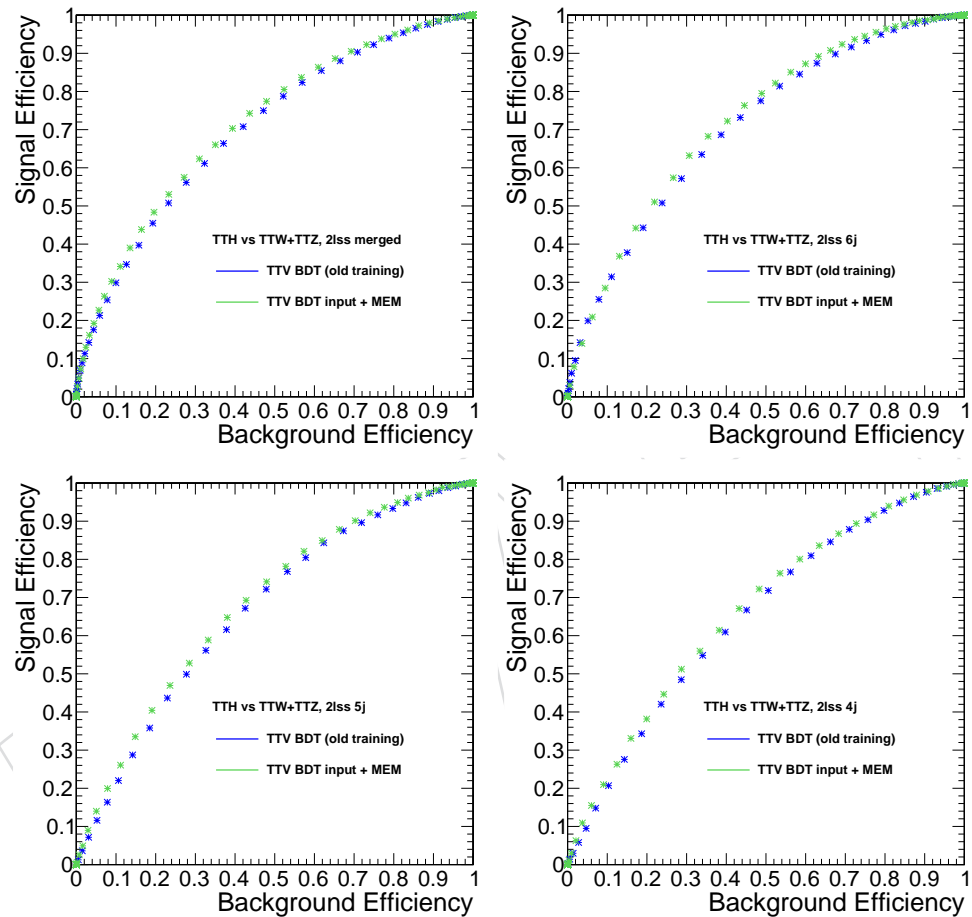


Figure 88: Comparison of TTV BDT and new BDT including MEM in 2lss signal region for (a) all events (b) 0 missing jets, (c) 1 missing jets, (d) 2 missing jets.

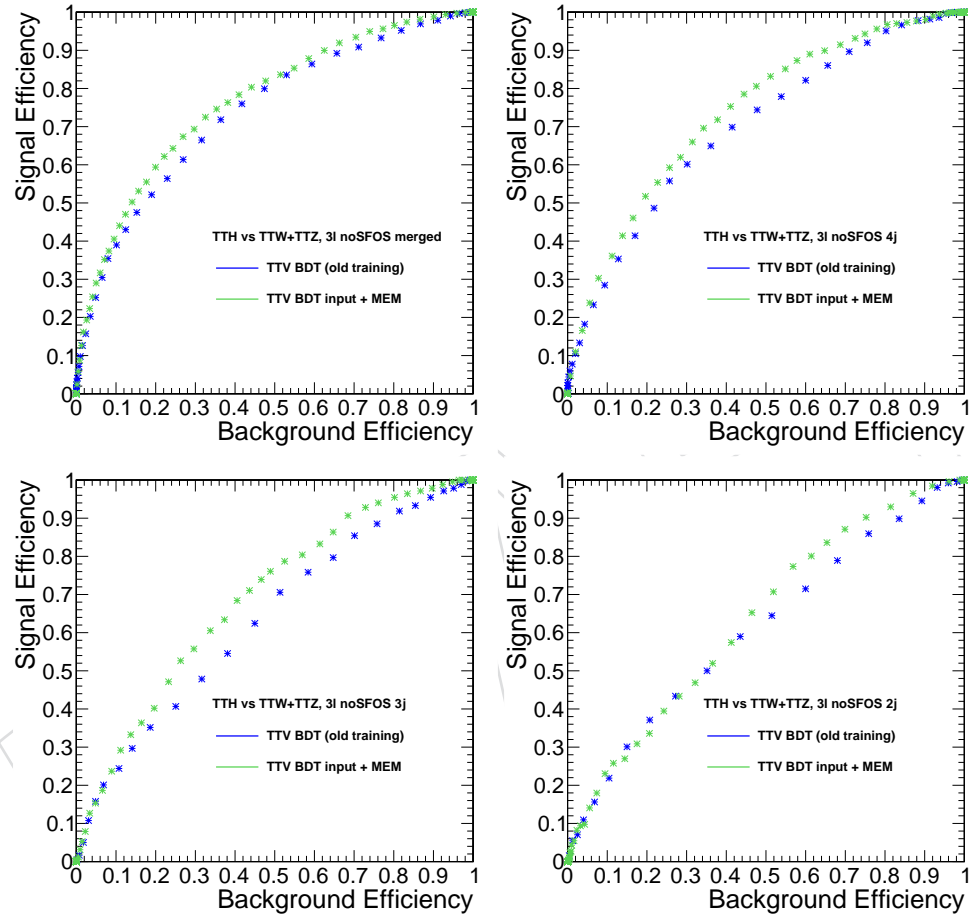


Figure 89: Comparison of TTV BDT and new BDT including MEM in 3l signal region, without SFOS lepton pair, for (a) all events (b) 0 missing jets, (c) 1 missing jets, (d) 2 missing jets.

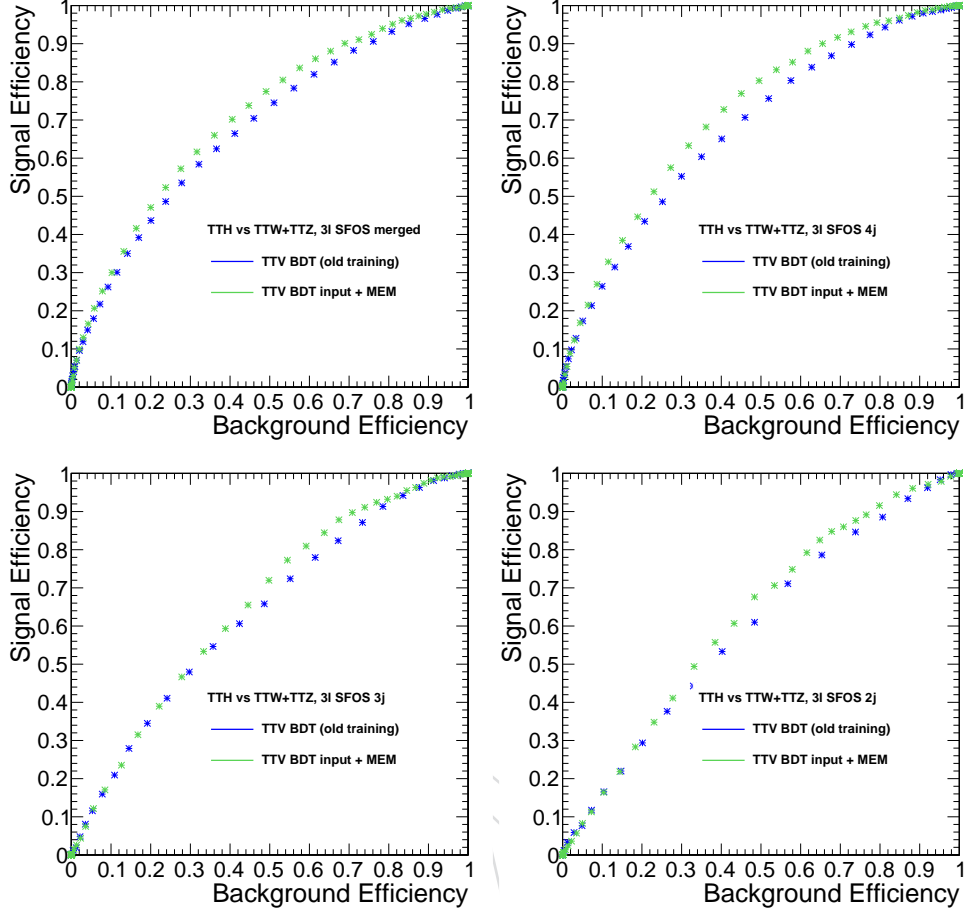


Figure 90: Comparison of TTV BDT and new BDT including MEM in 3l signal region, with a SFOS lepton pair, for (a) all events (b) 0 missing jets, (c) 1 missing jets, (d) 2 missing jets.

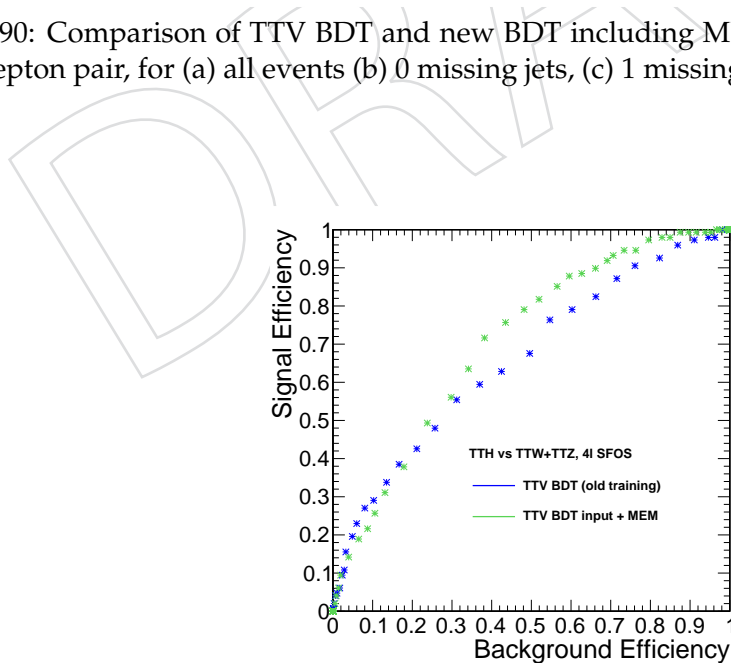


Figure 91: Comparison of TTV BDT and new BDT including MEM in 4l signal region for all events

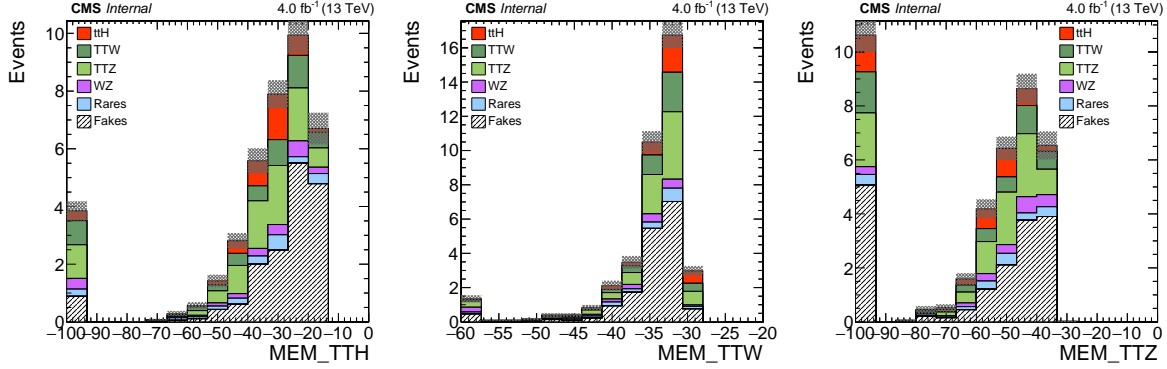


Figure 92: Log of MEM weights in the 3l signal region.

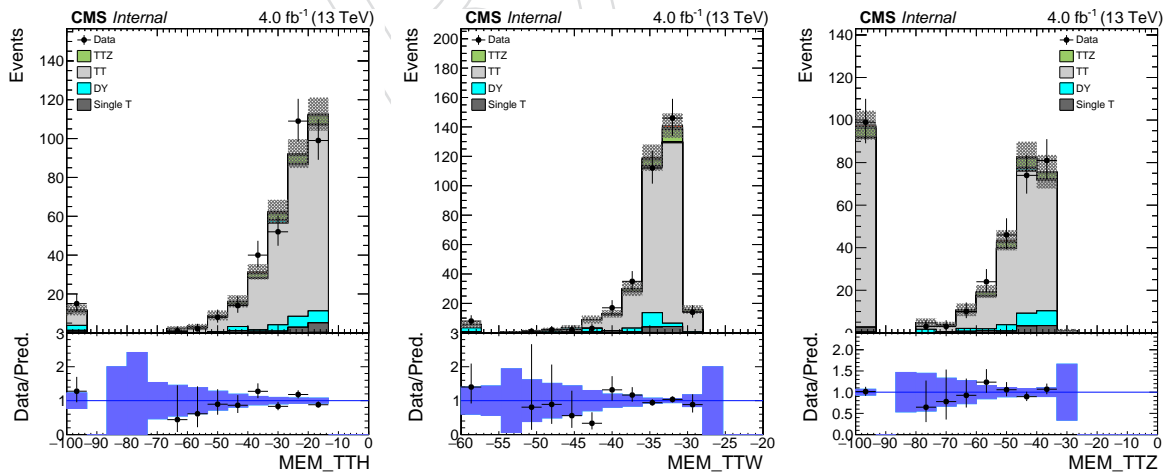


Figure 93: Log of MEM weights in the 3l application region.

1041 C Event Reconstruction

1042 Event reconstruction is performed with a BDT. The objective is to correctly match each selected
 1043 jet and lepton to a final state particle in a $t\bar{t}H$ event, then use the BDT response and other
 1044 variables from the reconstruction to discriminate against the non-prompt $t\bar{t}$ background.

1045 Event reconstruction targets the 2lss category, specifically where the Higgs decays to W bosons.
 1046 In the 2lss category, this means that one lepton originates from the top system, and the other
 1047 from the Higgs. For the jets, one of the W bosons from the Higgs decays hadronically, one of
 1048 the top quarks decays hadronically, producing a total of two b-jets, and four light-flavor jets
 1049 from the hadronic W decays.

1050 C.1 Training

1051 The event reconstruction BDT is trained using the $t\bar{t}H$ monte-carlo powheg signal sample de-
 1052 scribed previously.

1053 The signal is correctly matched $t\bar{t}H$ events, which pass the 2lss selection. Because the 2lss event
 1054 selection requires at least four jets, the vast majority of signal events used for training are only
 1055 partially reconstructed, since a full reconstruction necessitates six matched jets. Because so few
 1056 events can be fully reconstructed, we must consider partial reconstructions for events that have
 1057 fewer than six matched jets. The strategy for this is to use ‘empty’ jets whose four-vectors are
 1058 set to zero to substitute missing jets in the event. Finally we require the signal events to have
 1059 two correctly matched selected leptons, and at least four correctly matched selected jets.

1060 The background consists of all jet and lepton permutations of incorrectly matched $t\bar{t}H$ events.
 1061 For the background, the empty jets are added according to the jet multiplicity. For events with
 1062 seven or fewer selected jets, three empty jets are added, for events with eight selected jets, two
 1063 empty jets are added, and one empty jet is added for events with greater than eight selected
 1064 jets. To reduce the computation time and improve performance, several cuts are applied at
 1065 each permutation to remove unlikely reconstructions. These cuts include applying the b-tag
 1066 requirement on the two jets being considered as b-jets (1 b-tight, 2 b-loose) described earlier,
 1067 requiring that no reconstructed W have a mass greater than 120 GeV, requiring the Higgs mass
 1068 be less than 130 GeV, requiring the leptonic top mass be less than 180 GeV, and requiring the
 1069 hadronic top mass be less than 220 GeV. Additionally, we ignore permutations arising from
 1070 swapping two light flavor jets from the same W boson, as the reconstruction is identical.

1071 The BDT uses eight input variables, consisting of the CSV of the b-jets from the top system,
 1072 the highest CSV of light flavor jets from the hadronic top decay, the transverse momentum of
 1073 the reconstructed hadronic top, the mass of the reconstructed hadronic top, the mass of the
 1074 W originating from the hadronic top, the mass of the hadronic W originating from the Higgs,
 1075 and the solid angle between the reconstructed tops. This approach focuses on the hadronic
 1076 top decay, as the other aspects of the event are more difficult to reconstruct due to the missing
 1077 energy from the neutrinos.

1078 C.2 Evaluation

1079 The event reconstruction BDT is evaluated by iterating over all possible lepton and jet permu-
 1080 tations, and selecting the highest scoring permutation as the reconstruction for each event. For
 1081 the evaluation and usage, the empty jet prescription and permutation cuts used are identical to
 1082 the background training. The results of the reconstruction have been shown to offer significant
 1083 improvement in discriminating against the non-prompt $t\bar{t}$ background, since it is more diffi-
 1084 cult to reconstruct a non-prompt $t\bar{t}$ event under a $t\bar{t}H$ hypothesis. The variables with highest

discrimination power against $t\bar{t}$ include the BDT output itself, the reconstructed hadronic top mass, the reconstructed hadronic top transverse momentum, and the CSV of the light flavor jet from the top, which are shown in Figures 94 through 98.

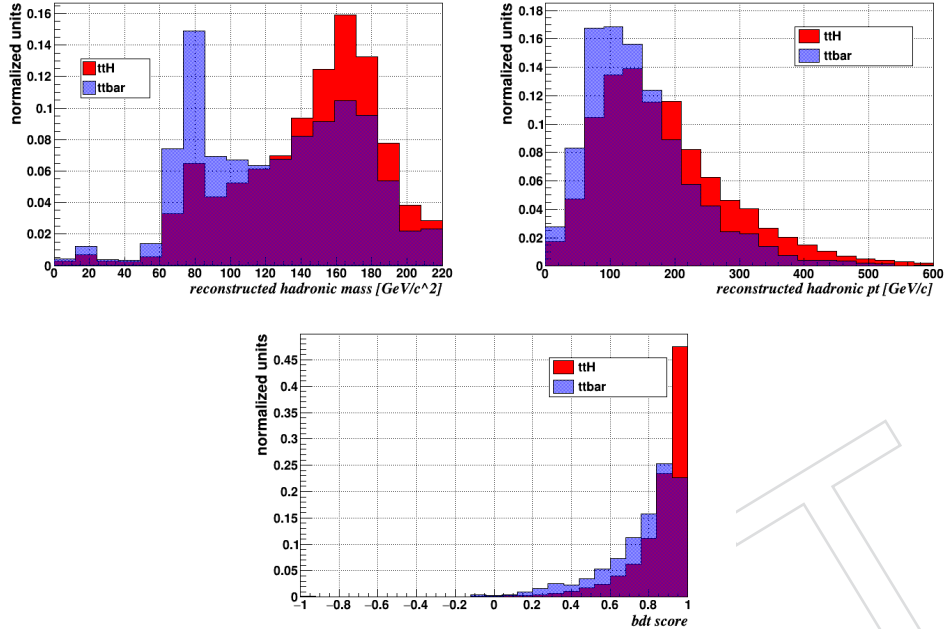


Figure 94: Output variables used for discrimination against semi-leptonic $t\bar{t}$.

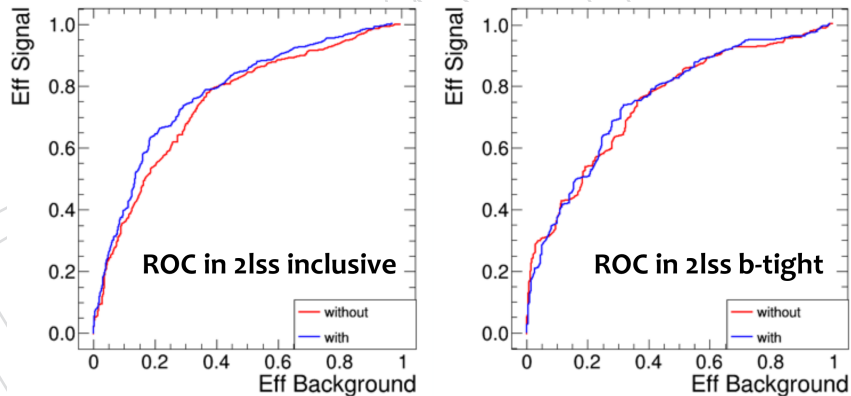


Figure 95: ROC curve of signal extraction BDT with and without reconstruction variables evaluated against $t\bar{t}$.

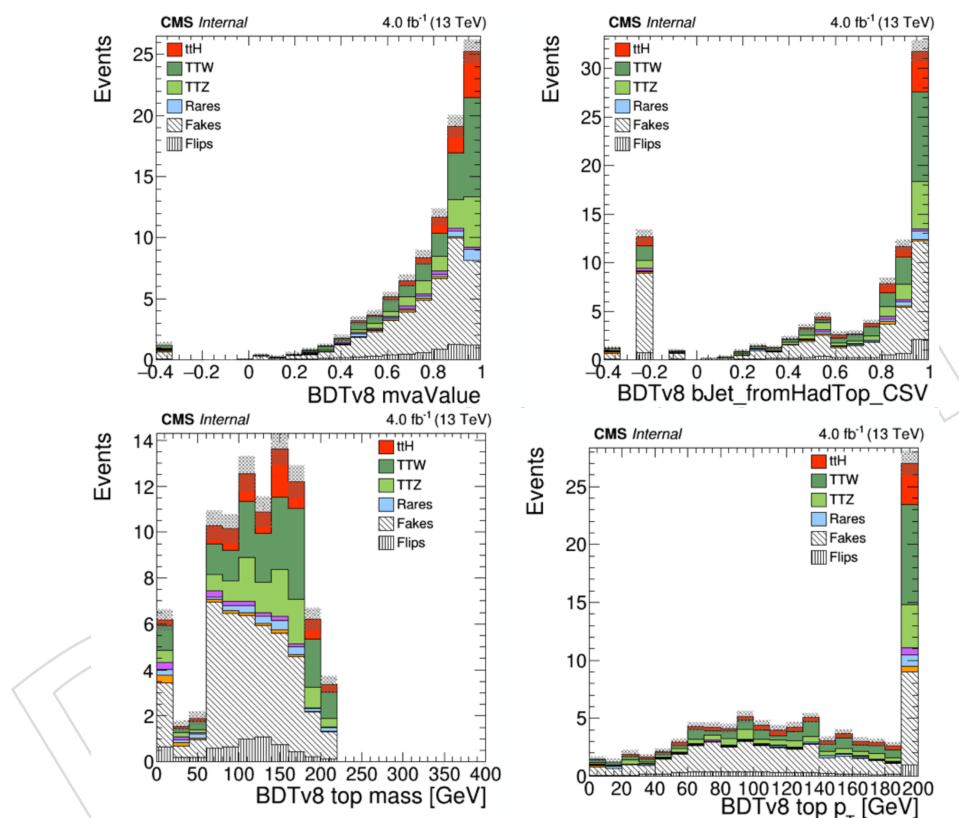


Figure 96: Event reconstruction variables in the 2lss signal region.

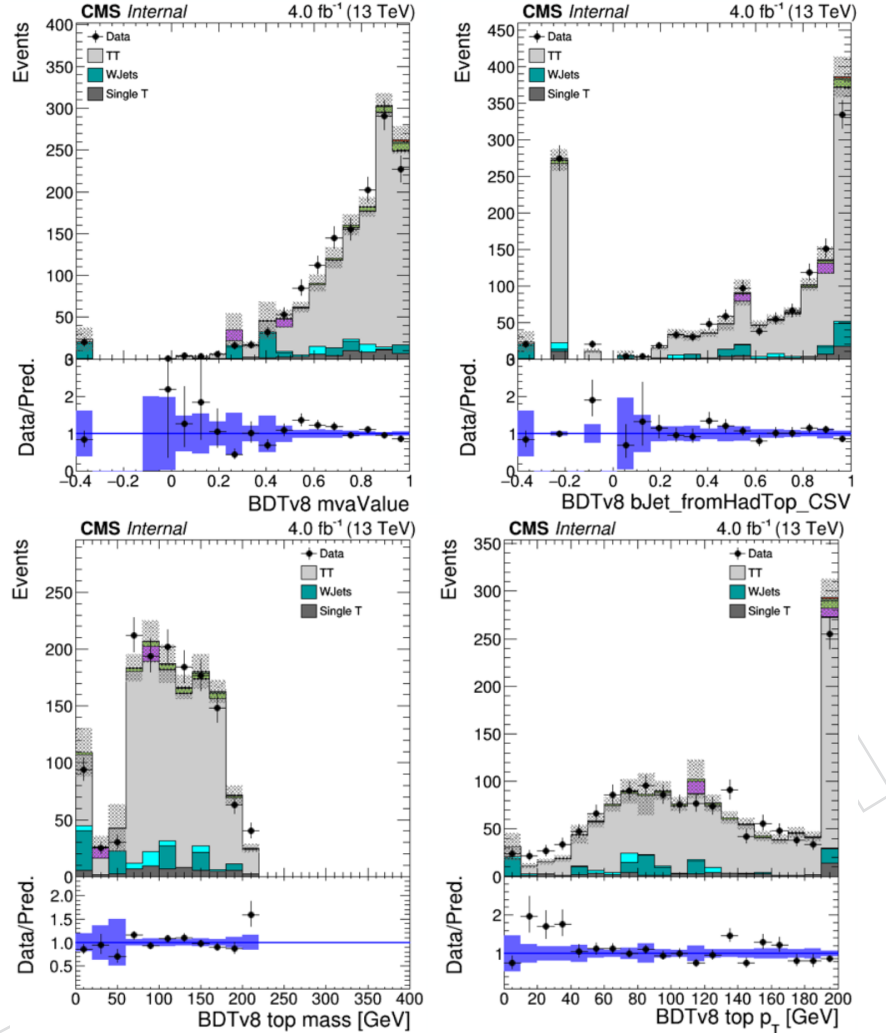


Figure 97: Event reconstruction variables in the 2lss application region.

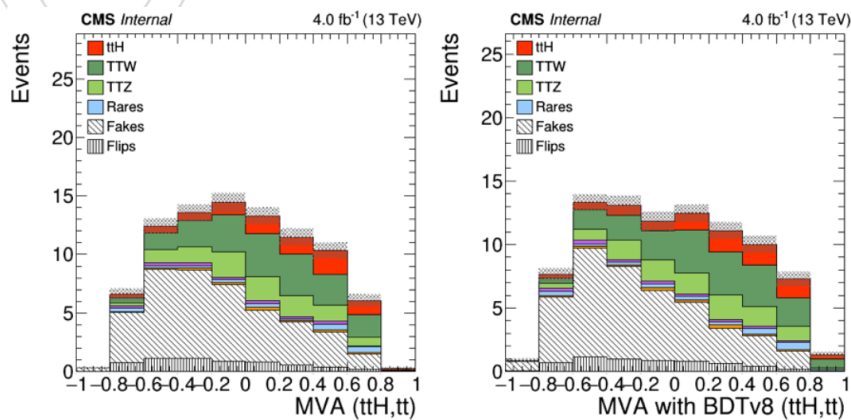


Figure 98: Signal extraction MVA output with and without signal extraction.

References

- [1] CMS Collaboration, "Observation of a new boson at a mass of 125 GeV with the CMS experiment at the LHC", *Phys. Lett. B* **716** (2012) 30, doi:10.1016/j.physletb.2012.08.021.
- [2] ATLAS Collaboration, "Observation of a new particle in the search for the Standard Model Higgs boson with the ATLAS detector at the LHC", *Phys. Lett. B* **716** (2012) 1, doi:10.1016/j.physletb.2012.08.020.
- [3] ATLAS and CMS Collaboration, "Combined measurement of the Higgs boson mass in pp collisions at $\sqrt{7}$ and 8 TeV with the ATLAS and CMS experiments", *Phys. Rev. Letter* **114** (2015) 45, doi:<http://dx.doi.org/10.1103/PhysRevLett.114.191803>.
- [4] ATLAS and CMS Collaboration, "Combined measurement of the Higgs boson mass in pp collisions at $\sqrt{7}$ and 8 TeV with the ATLAS and CMS experiments", *Eur. Phys. J. C* **76** (2015) 64, doi:10.1140/epjc/s10052-015-3769-y.
- [5] CMS Collaboration, "Precise determination of the mass of the Higgs boson and tests of compatibility of its couplings with the standard model predictions using proton collisions at 7 and 8 TeV", *Eur. Phys. J. C* **75** (2015) 212, doi:10.1140/epjc/s10052-015-3351-7.
- [6] LHC Higgs Cross Section Working Group et al., "Handbook of LHC Higgs Cross Sections: 1. Inclusive Observables", CERN-2011-002 (CERN, Geneva, 2011) arXiv:1101.0593.
- [7] CMS Collaboration, "Search for the associated production of the Higgs boson with a top-quark pair", *JHEP* **09** (2015) doi:10.1007/JHEP09(2014)087.
- [8] CMS Collaboration, "Search for the SM Higgs boson produced in association with top quarks in multilepton final states", CMS Physics Analysis Summary CMS-PAS-HIG-13-020, 2013.
- [9] CMS Collaboration, "Search for ttH production in multilepton final states at $\sqrt{s} = 13$ TeV", CMS Physics Analysis Summary CMS-PAS-HIG-15-008, 2015.
- [10] C. Collaboration, "JSON files for 25ns data (CMS Hypernews)", 2016. <https://hypernews.cern.ch/HyperNews/CMS/get/physics-validation/2669.html>.
- [11] J. Alwall et al., "The automated computation of tree-level and next-to-leading order differential cross sections, and their matching to parton shower simulations", 2014. arXiv:1405.0301.
- [12] T. Sjöstrand, S. Mrenna, and P. Skands, "A brief introduction to PYTHIA 8.1", *Comp. Phys. Comm.* **178** (2008) 852, doi:10.1016/j.cpc.2008.01.036, arXiv:0710.3820.
- [13] S. Alioli, P. Nason, C. Oleari, and E. Re, "A general framework for implementing NLO calculations in shower Monte Carlo programs: the POWHEG BOX", *JHEP* **06** (2010) 043, doi:10.1007/JHEP06(2010)043, arXiv:1002.2581.
- [14] CMS Collaboration, "Dilepton trigger and lepton identification efficiencies for the top quark pair production cross section measurement at 8 TeV in the dilepton decay channel.", CMS AN AN-12-389, 2012.

- 1129 [15] CMS Collaboration, “Particle-Flow Event Reconstruction in CMS and Performance for
1130 Jets, Taus, and MET”, CMS Physics Analysis Summary CMS-PAS-PFT-09-001, 2009.
- 1131 [16] CMS Collaboration, “Commissioning of the Particle-Flow reconstruction in
1132 Minimum-Bias and Jet Events from pp Collisions at 7 TeV”, CMS Physics Analysis
1133 Summary CMS-PAS-PFT-10-002, 2010.
- 1134 [17] M. Cacciari, G. P. Salam, G. Soyez, “FastJet user manual”, (2011).
1135 arXiv:hep-ph/1111.6097v1.
- 1136 [18] M. Cacciari, G. P. Salam, “Dispelling the N^3 myth for the k_t jet-finder”, *Phys. Lett. B* **641**
1137 (2006) 57, doi:10.1016/j.physletb.2006.08.037, arXiv:hep-ph/0512210.
- 1138 [19] CMS Collaboration, “Determination of Jet Energy Calibration and Transverse Momentum
1139 Resolution in CMS”, *JINST* **6** (2011) 11002, doi:10.1088/1748-0221/6/11/P11002.
- 1140 [20] CMS Collaboration Collaboration, “Identification of b-quark jets with the CMS
1141 experiment”, *JINST* **8** (2013) P04013, doi:10.1088/1748-0221/8/04/P04013,
1142 arXiv:1211.4462.
- 1143 [21] CMS Collaboration, “Performance of CMS muon reconstruction in pp collision events at
1144 $\sqrt{s} = 7$ TeV”, *JINST* **7** (2012) P10002, doi:10.1088/1748-0221/7/10/P10002,
1145 arXiv:1206.4071.
- 1146 [22] G. Abbiendi et al., “Baseline muon selections”, October, 2014. https://twiki.cern.ch/twiki/bin/view/CMSPublic/SWGuideMuonId#Tight_Muon.
- 1148 [23] G. Petrucciani and C. Botta, “Two step prompt muon identification”, January, 2015.
1149 [https://indico.cern.ch/event/368007/contribution/2/material/
1150 slides/0.pdf](https://indico.cern.ch/event/368007/contribution/2/material/slides/0.pdf).
- 1151 [24] H. Brun and C. Ochando, “Updated Results on MVA eID with 13 TeV samples”, October,
1152 2014. [https://indico.cern.ch/event/367861/contribution/1/material/
1153 slides/0.pdf](https://indico.cern.ch/event/367861/contribution/1/material/slides/0.pdf).
- 1154 [25] A. Le Bihan et al., “Search for ttH in multilepton final states at 13 TeV”, CMS Analysis
1155 Note CMS AN-15-321, 2015.
- 1156 [26] CMS Collaboration, “Studies of Tracker Material”, *CDS Record* **1279138** (2010).
- 1157 [27] S. L. S. F. W. Group, “Lepton SF”, December, 2015.
1158 <https://twiki.cern.ch/twiki/bin/view/CMS/SUSLeptonSF>.
- 1159 [28] CMS Collaboration, “Reconstruction and identification of τ lepton decays to hadrons and
1160 ν_τ at CMS”, arXiv:1510.07488.
- 1161 [29] A. Nayak et al., “Multivariate τ -identification algorithms for 13 TeV data”, CMS Analysis
1162 Note CMS AN-15-310, 2015.
- 1163 [30] Y. R. . in preparation. [http://indico.cern.ch/event/407347/session/3/
1164 contribution/10/attachments/1211342/1766869/hxswg16.pdf](http://indico.cern.ch/event/407347/session/3/contribution/10/attachments/1211342/1766869/hxswg16.pdf).
- 1165 [31] P. production of low m_{ll} ttZ sample.
1166 <https://www.dropbox.com/s/fni1334aaa9cbfn/ttzlowmll.pdf?dl=0>.

- ¹¹⁶⁷ [32] C. Botta et al., "Search for the standard model Higgs boson produced in association with
¹¹⁶⁸ top quarks and decaying to leptons", CMS Analysis Note CMS AN-13-159, 2013.
- ¹¹⁶⁹ [33] G. Lepage, "A new algorithm for adaptive multidimensional integration", *Journal of*
¹¹⁷⁰ *Computational Physics* **27** (1978) 192–203.
- ¹¹⁷¹ [34] A. Buckley et al., "LHAPDF6: parton density access in the LHC precision era", *Eur. Phys.*
¹¹⁷² *J.* **C75** (2015) 132, doi:10.1140/epjc/s10052-015-3318-8, arXiv:1412.7420.
- ¹¹⁷³ [35] P. Artoisenet, V. Lemaitre, F. Maltoni, and O. Mattelaer, "Automation of the matrix
¹¹⁷⁴ element reweighting method", *JHEP* **12** (2010) 068,
¹¹⁷⁵ doi:10.1007/JHEP12(2010)068, arXiv:1007.3300.

DRAFT